Exploring the nature of radio relics and halos in galaxy clusters through GHz radio observations

Dissertation
zur
Erlangung des Doktorgrades (Dr. rer. nat.)
der
Mathematisch-Naturwissenschaftlichen Fakultät
der
Rheinischen Friedrich-Wilhelms-Universität Bonn

vorgelegt von
Monica Trasatti
aus
Popoli, Italien

Bonn, 2014

Angefertigt mit Genehmigung der Mathematisch-Naturwissenschaftlichen Fakultät der
Rheinischen Friedrich-Wilhelms-Universität Bonn

1. Gutachter	Prof. Dr. Ulrich Klein
2. Gutachter	Prof. Dr. Marcus Brüggen

Tag der Promotion: 27.11.2014
Erscheinungsjahr: 2015

Ad Emiliano
ed ai miei genitori

Contents

List of Figures

List of Tables

Abstract

This project has been developed in the framework of the DFG Research Unit 1254 titled *Magnetization of Interstellar and Intergalactic Media*. The Research Unit involves eight different institutions spread over Germany and has the aim of studying magnetic field properties on different scales and environments making use of both observations and numerical simulations. In particular in this thesis we study these properties on the largest scales, that of clusters of galaxies. Galaxy clusters are, indeed, the largest gravitationally bound systems in the Universe. We focused on the study of diffuse Mpc-scale synchrotron emission (referred to as radio halos and radio relics) in galaxy clusters not related to any particular discrete source but rather with the diffuse medium. The emission from these sources helped in unambiguously prove the presence of weak magnetic fields ($\sim \mu$G) and relativistic electrons in the intra-cluster medium (ICM) in galaxy clusters, together with the hot thermal plasma emitting X-rays.
Radio halos permeate the central Mpc^3 of galaxy clusters and the radio emission usually follows the roundish X-ray emission from the thermal gas. *Radio relics* are more irregularly shaped and are located at the cluster's periphery. Both kinds of sources have steep radio spectra ($\alpha > 1$, $S_\nu \propto \nu^{-\alpha}$), but relics exhibit a higher surface brightness than halos, and a high degree of polarization (up to 40%). Even though the existence of radio relics and halos has been known for three decades, their origin is as yet debated. The main difficulty in explaining such extended emissions arises from the combination of their Mpc size and the relatively short radiative lifetime of the emitting electrons that require some form of *in-situ* production or (re-)acceleration. Both phenomena are mostly present in un-relaxed clusters, suggesting that cluster mergers, manifesting the formation of cosmic structure in the bottom-up scenario, play a key role in producing them. However the underlying physical mechanisms are thought to be different for the different classes of sources.
All these ingredients make the study of these sources not only relevant in terms of their physics, but also crucial for a comprehensive description of the composition and dynamics of the ICM, for the study of particle-acceleration mechanisms as well as for a global understanding of the mechanisms at play during the processes of cluster assembly in the Universe.
The proposed formation mechanisms, for both relics and halos, differ in the predictions of the morphological and spectral characteristics of the different classes of sources and can be tested through multi-wavelengths observations. In general, according to these models, the statistic of such sources is expected to increase with the advent of the new generation low-frequencies radio telescopes. The currently known radio relics and halos are, therefore, the most energetic cases, for which high frequency observations (e.g. L, S, C bands) are necessary to constrain the shape of the spectra in order to test the models expectations. To date, the integrated spectra are only in few cases obtained with more than three flux density measurements at different frequencies and for most sources the highest available frequency is 1.4 GHz. These extended sources are usually contaminated by numerous discrete sources, which need to be carefully subtracted from the total diffuse emission. This task requires high-resolution imaging at many frequencies proper of radio interferometers. However, at high frequencies, interferometers en-

counter the technical problem of the *missing short spacings*, that makes them "blind" to very extended structures. It is therefore necessary to complement high-resolution interferometric observation with single-dish data, which are optimal to catch all the emission from a field, although they lack in angular resolution.

In this Thesis we focus on the spectral and polarization properties of these diffuse sources at GHz frequencies, and their connection with the properties of the thermal gas in clusters of galaxies in order to test the current models. With this aim, we present the results from high-frequencies observations of extended emissions from galaxy clusters, performed with both an interferometer (WSRT) and a single dish (Effelsberg). The Thesis is structured as follows:

- In Chap. 1 we review the general properties of clusters of galaxies at different wavelengths. The thermal and non-thermal phenomena taking place in the ICM and their inter-connection are described, as well as the theory of structure formation.
- In Chap. 2 we review the current knowledge on radio relics and halos from both an observational and theoretical point of view.
- In Chap. 3 we present new results from high-frequency observations of the radio relic in the Coma galaxy cluster performed in the L and S bands with the WSRT and the Effelsberg-100m telescope. We describe theory and application of a method for the combination of single-dish and interferometric data that allows to study with high resolution the properties of these extended sources at GHz frequencies. We moreover present the results from a collaboration on the analysis of SZ Planck data used to investigate whether a pressure discontinuity is directly visible at the position of the Coma radio relic.
- In Chap. 4 we present new high-frequency total intensity observations of the galaxy cluster Abell 2256 performed at 2.3 GHz (S band) with the WSRT and at 2.64 (S band) and 4.85 (C band) GHz with the Effelsberg-100m telescope. Combining our new observations with images available at other frequencies, we constrain the radio integrated spectrum of the diffuse emission in Abell 2256 over the widest frequency range collected so far for this kind of objects (63 -10450 MHz). We moreover use Suzaku and XMM-Newton X-ray observations to investigate the ICM properties in the regions across the radio relic emission. Different possibilities on the origin of the radio relic are discussed in the light of the new radio and X-ray properties presented.
- In Chap. 5 we present a detailed analysis of the spectral properties at high frequencies across the diffuse radio relic emission in the galaxy cluster Abell 2256. We moreover present new polarization observations of Abell 2256 performed at 2.3 GHz, 2.64 GHz and 4.85 GHz. Complementing the radio analysis with a X-ray analysis of the ICM properties, we discuss a possible geometry of the complex relic source.
- In Chap. 6 we present the preliminary results from the analysis of new high-frequencies observations (in the L and S bands) of the radio halo in the Coma cluster.

Chapter 1

Clusters of galaxies

For a review of the current observational and theoretical knowledge on galaxy clusters see series of reviews collected in the book titled " Clusters of Galaxies: Beyond the Thermal View " (Kaastra, 2008).

Clusters of galaxies are the most massive gravitationally bound systems in the Universe. In the hierarchical clustering scenario for the formation of cosmic structures, they arise from the gravitational amplification and collapse of perturbations of the otherwise homogeneous primordial density field (Peebles, 1993) (Sect. 1.1). In a Universe dominated by Dark Matter (DM), the gravitational instability process follows the evolution of the dominant component, leading to the formation, in primis, of *dark matter halos*. Galaxy clusters and other luminous objects form inside the potential wells created by such halos. DM halos are fully characterized by their redshift and mean matter density, which in turn are related to the power spectrum of the initial density fluctuations (Peebles, 1980). The scale-free dark-matter collapse drives the evolution of halo concentration across cosmic time (see, e.g., recent work by Gao et al. (2012)), and the ensuing similarity yields both a universal dark matter distribution and simple global scaling relations that should describe the entire halo-cluster population (Bertschinger (1985), Kaiser et al. (1995), Navarro et al. (1995), Evrard et al. (1996)).

However, the observable properties of clusters are determined by the visible baryonic component, which is subject to complex physical processes related to structure formation and feedback. The easiest way to identify a cluster of galaxies is through an over-density in the projected distribution of galaxies visible in the optical band. The first catalogs were, in fact, purely based on visual inspection of photographic plates (Abell (1958), Abell et al. (1989)). Smaller *Groups* count ~ 50 member galaxies, while richer *Clusters* can count up to 1000s of galaxies. Figures 1.1a and 1.2a show the optical view of two massive clusters, Abell 1656 (best known as the Coma cluster) and Abell 1689. The bright galaxies are the massive elliptical galaxies that usually populate the inner region of a cluster. However, stars and galaxies are the minor components of a cluster in terms of mass. Smith (1936) first noticed in his study of the Virgo cluster that the mass implied by the motion of the galaxies inside the cluster is largely exceeding that associated with the optical light component. This was confirmed by Zwicky (1937), and was the first evidence of the presence of dark matter. In this same 1937 paper, Zwicky also realized that one way to estimate the total cluster mass is to use the deflection of light of background sources determined by the cluster gravitational potential well (*gravitational lensing effect*). The first evidence of this effect in a galaxy cluster appeared fifty years later (Lynds & Petrosian, 1986). To date, both strong gravitational lensing, which creates multiple images of background sources, and weak gravitational lensing, which produces

small ellipticities in the shapes of background galaxies, are used to reconstruct the total mass content of galaxy clusters. One example is given in (Broadhurst et al., 2005) for Abell 1689 (Fig. 1.2d). Clusters are indeed constituted by 80 % of dark matter, 17 % of hot diffuse baryonic matter (the Intra-Cluster Medium, ICM) and only 3% of the colder baryons that compose the stars and the Interstellar Medium (ISM) in galaxies. As the main baryonic reservoir in massive clusters, the hot gas in the ICM is the natural target for studying the physical processes at play and their link to the underlying cluster DM content. It is mainly composed by thermal plasma that emits in the X-ray band via bremsstrahlung (Figs.1.1b 1.2b; Sect. 1.2.1) and via ionic emission lines. Moreover, the Inverse Compton (IC) interaction of these thermal electrons with the cosmic microwave background (CMB) photons is known as the *Sunyaev-Zeldovitch effect* (SZ) and allows to nicely complement X-ray studies of the properties of the thermal gas in galaxy clusters (Fig. 1.1c; Sect. 1.2.2). Detection of diffuse radio emission from many galaxy clusters (Figs. 1.1d and 1.2c; Sect. 1.2.3 and Chap. 2) furthermore provided strong evidence of the presence of relativistic electrons with very high energies, emitting through the synchrotron mechanism in magnetic fields of the ICM (Sect. 1.3). The interaction of such relativistic electrons with the CMB photons may result in hard X-ray emission via the IC process (Sect. 1.2.4), while the IC emission owing to the interaction of even more energetic electrons with CMB photons, may lead to gamma-ray emission (Sect. 1.2.5) (e.g., Petrosian et al. (2008)).

Scaling relations between cluster properties (like mass, galaxy velocity dispersion, X-ray luminosity and temperature) observed in most clusters, testify that the cluster components are in approximate dynamical equilibrium within the cluster gravitational potential. However, spatially inhomogeneous thermal and non-thermal emissions of the ICM observed in some clusters are signatures of ongoing cluster merging and interactions. Cluster mergers, naturally expected in a hierarchical scenario of structure formation, are among the most energetic phenomena in the universe ($E \approx 10^{64}$ erg). They are expected to produce shocks and turbulence in the ICM that might be responsible for the compression and heating of the thermal gas (inhomogeneity observed in the X-rays) and for the acceleration of particles (that can produce non-thermal emission in the radio/hard X-ray). Figure 1.3 shows a schematic overview of the relevant non-thermal radiative processes in galaxy clusters (from Pinzke (2010)) that will be reviewed in this and in the next Chapters.

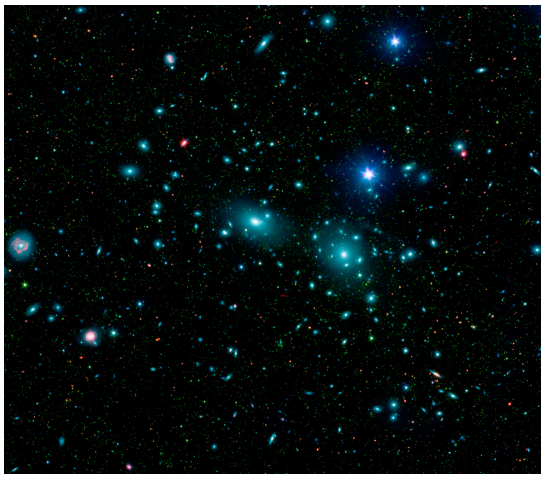

(a) Central part of the Coma Cluster as seen at visible wavelengths. Credit: NASA/SDSS.

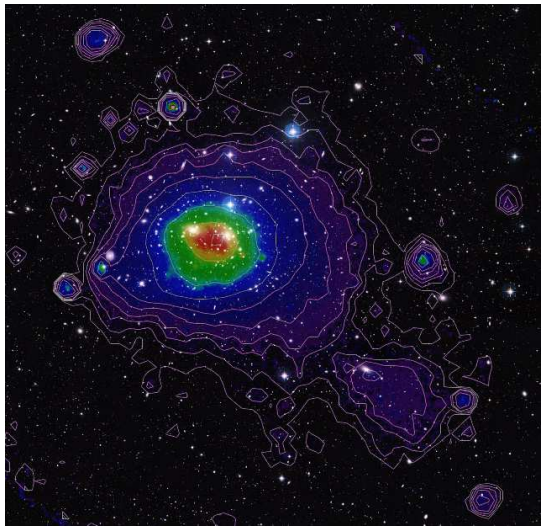

(b) X-ray image taken with the ROSAT satellite in colors and white contours (Credit:ESA/ROSAT) overlaid on the optical image.

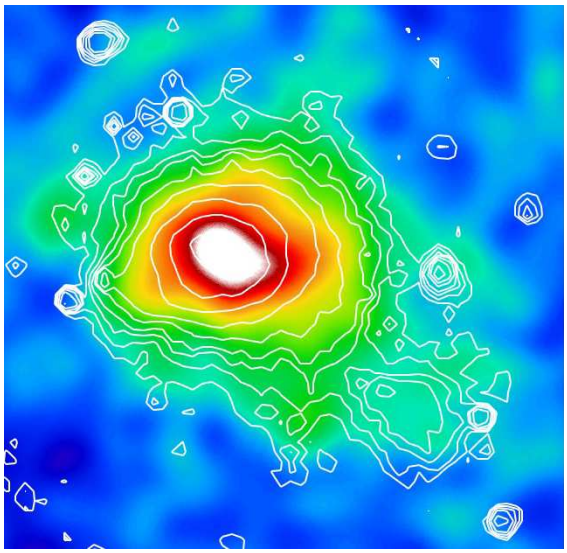

(c) The Coma cluster as seen by Planck through the SZ effect (in color scale; Planck Collaboration et al. (2013b)) with ROSAT X-ray contours overlapped (Credit: ESA / LFI and HFI Consortia).

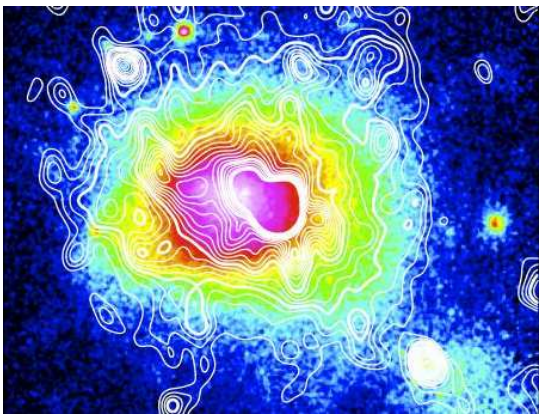

(d) WSRT radio emission (white contours) overlaid on the color-scale ROSAT X-ray image (Adapted from Brown & Rudnick (2011).

Fig. 1.1: Multi-wavelength properties of the Coma galaxy cluster.

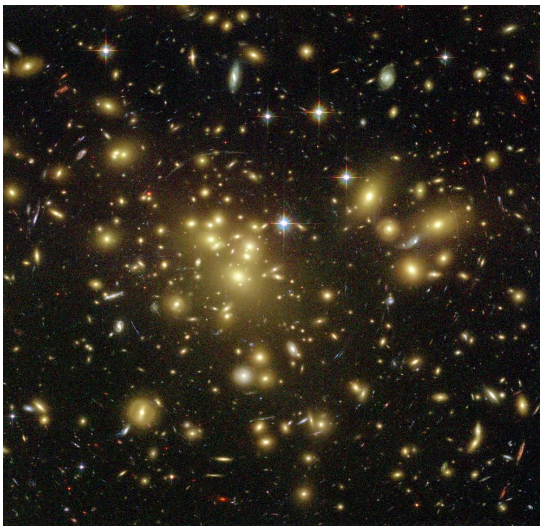

(a) Optical image taken with the Hubble Space Telescope (HST). Credit: NASA/STScI.

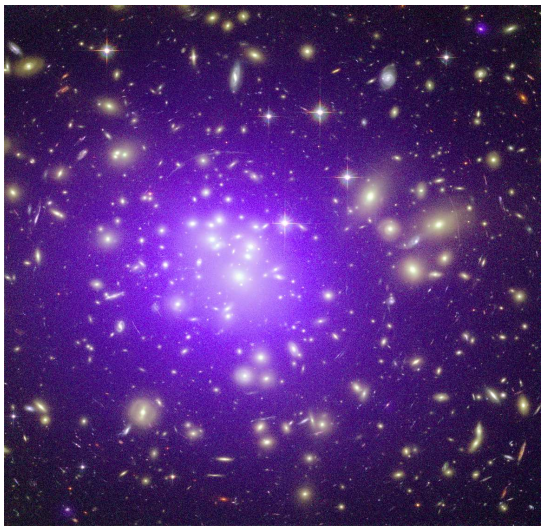

(b) X-ray image taken with the Chandra satellite in purple (Credit: NASA/CXC/MIT/E.-H Peng et al) overlaid on the HST optical image.

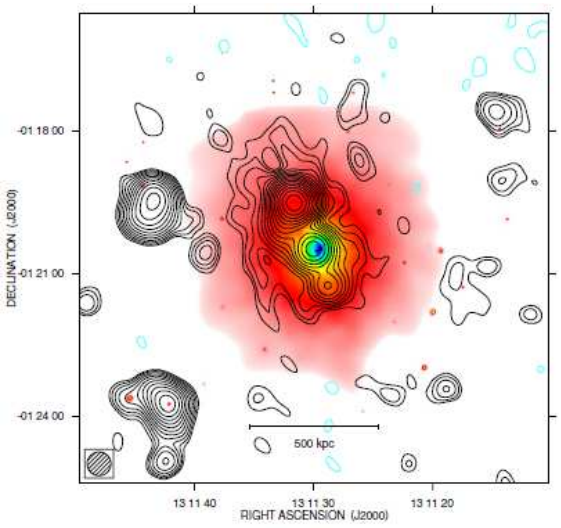

(c) Radio contours obtained with the Very Large Array (VLA) (from Vacca et al. (2011)) overlaid on the Chandra X-ray image (in colour scale).

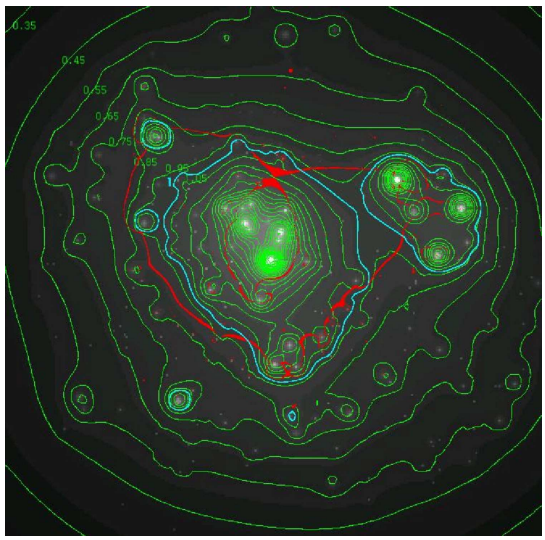

(d) Dark matter map reconstructed from lensing analysis (from Broadhurst et al. (2005)).

Fig. 1.2: Multi-wavelength properties of the galaxy cluster Abell 1689 (z=0.18).

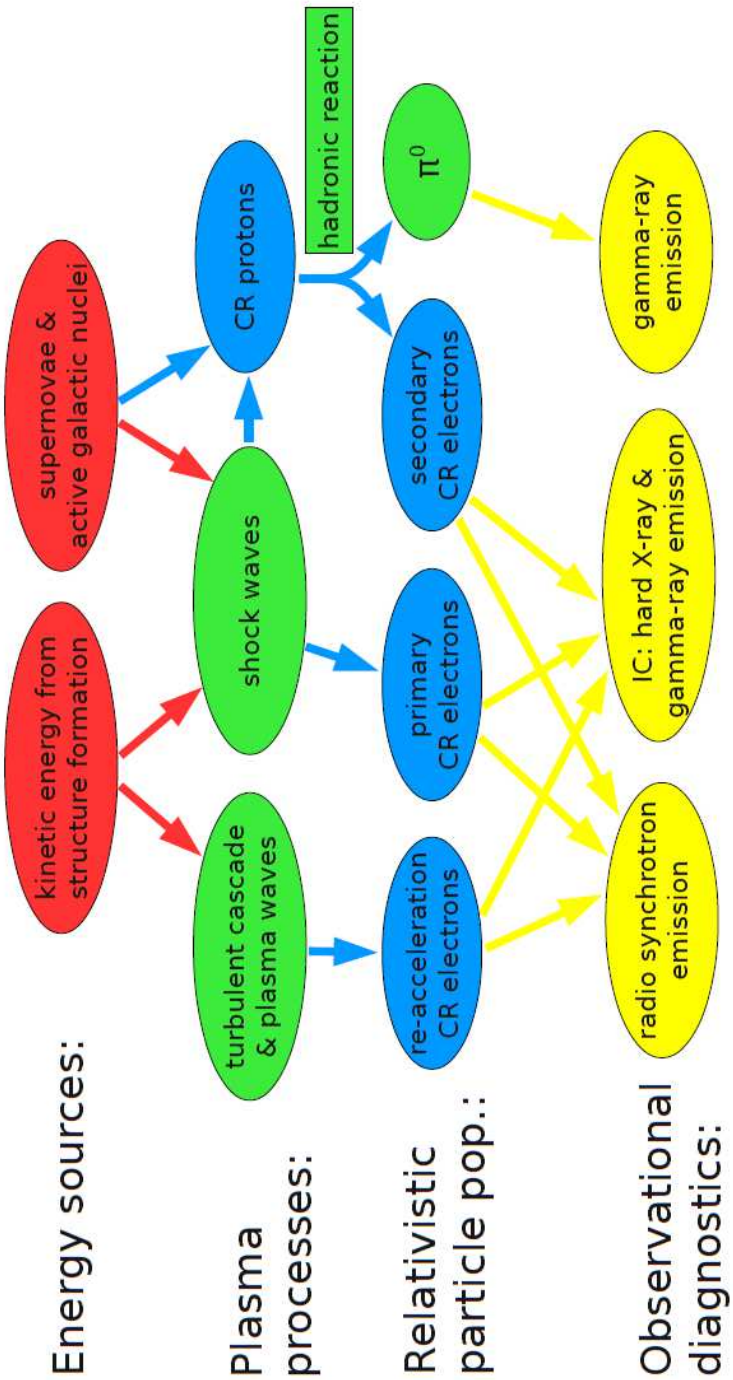

Fig. 1.3: Schematic overview of the relevant non-thermal radiative processes in galaxy clusters. Both gravitational and non-gravitational energy sources (red) are able to accelerate particle populations to relativistic energies (blue) through different plasma processes (green). Cosmic-ray populations are probed through non-thermal emission (yellow), where electron populations can induce radio synchrotron emission as well as inverse-Compton emission in both the X-ray and γ-ray energy regime. Adopted from Pinzke (2010).

1.1 Formation scenario

Reviews of the cosmological formation and evolution of galaxy clusters in the context of theoretical foundations, observational data and numerical simulations include, e.g., Voit (2005), Borgani & Kravtsov (2011) and Lukash et al. (2011).

The different theories about structure formation start similarly from the idea that the structures observed today originated from the growth of gravitational instabilities in density fluctuations in the primordial universe. Jeans was the first to develop a simple formulation for such a mechanism, demonstrating that small density perturbations in a homogeneous, isotropic and stationary fluid can evolve with time, becoming instable and collapsing.
The existence and evolution of such primordial perturbation is testified by observations of small anisotropies in the cosmic microwave background (CMB) (Bennett et al., 1996). The CMB is thermal radiation that pervades every direction in the sky with almost the same brightness, and it is considered to be an echo of the *Big Bang*. Over time, this primeval light has cooled and weakened considerably; nowadays we detect it in the microwave domain. It has a thermal black-body spectrum at a temperature of 2.72548±0.00057 K that peaks at 160.2 GHz, in the mm wavelength range. Accurate measurements of its apparent temperature have revealed that tiny differences do exist as tiny as one part in a million. Recently the Planck satellite (Planck Collaboration et al., 2011a) [1] allowed to image the temperature and polarization anisotropies of the Cosmic Background Radiation Field over the whole sky, with unprecedented sensitivity and angular resolution, as shown in Fig. 1.4. It shows indeed tiny temperature fluctuations that correspond to regions of slightly different densities, representing the seeds of the present cosmic web of galaxy clusters and dark matter.

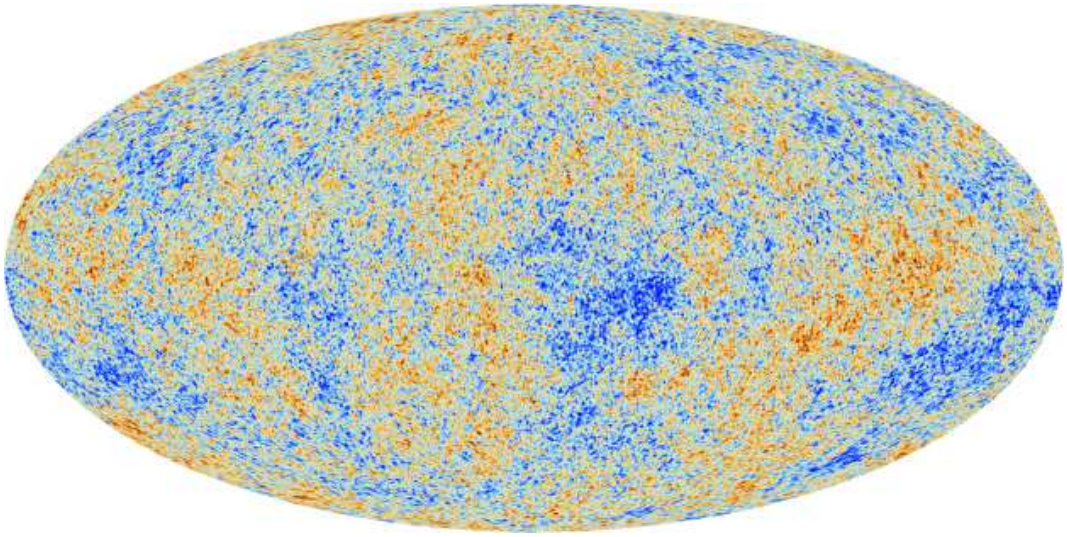

Fig. 1.4: The cosmic microwave background seen by Planck. Credits: ESA, Planck Collaboration.

Astronomical observations over the last century have revealed the existence of a continuous hierarchy of cosmic structures involving a wide range of scales. Clusters of galaxies are the

[1] See the Planck mission web-page for an overview of the mission's results and the list of publications: `http://www.rssd.esa.int/index.php?project=planck`.

largest objects that have had time to undergo gravitational collapse. They form through matter accretion and mergers between smaller groups and sub-clusters in the intersections of filaments of the so-called *cosmic web*.The gravitational instability process is dominated by the DM and first produces the dark matter halos, inside which stars, galaxies and clusters of galaxies will form.

Nowadays numerical simulations (N-body, hydro-dynamical and magneto-hydro-dynamical) constitute the new frontier for the study of cosmic structure formation. They provide the only instrument to follow the evolution of perturbations. They give us an invaluable instrument at hand for studying the growth of cosmological structure. Increased computational power and improved algorithms have led to a steady and rapid increase in the ability of N-body simulations to resolve the detailed internal structure of dark matter halos over substantial cosmological volumes. Figure 1.5 shows, for example, a very large N-body simulation of the dark-matter cosmic evolution in the concordance cold-dark-matter (ΛCDM) cosmology, the Millennium-II Simulation (MS-II)[2] (Boylan-Kolchin et al., 2009). The panels show the time evolution history (from top to bottom: at redshifts z = 6.2, 2.07, 0.99 and 0.0) of the dark matter distribution in the MS-II centered on a DM halo with mass similar to that of the Coma cluster (the largest DM halo in the simulation). The different columns show a zoom through three comoving scales (from left to right: 100, 40 and 15 h^{-1} Mpc). The well-known network of filaments, interconnecting individual halos and sub-halos and voids (the cosmic web) can be clearly seen on the largest scales. Figure 1.6 offers a successive zoom closer into the halo at the present epoch (z=0), up to a scale of 0.5 h^{-1} Mpc. The bottom-right panel is 5 h^{-1} Mpc on a side, approximately the diameter of the Coma-like DM halo. Such simulations provide precise predictions of the statistical formation of DM halos over an unprecedented range of scales, from halos similar to those hosting Local- Group dwarf spheroidal galaxies to halos corresponding to the richest galaxy clusters. Very recently the challenge of simultaneously following the evolution of dark matter and the baryonic component of the Universe on a large volume and with high resolution has been accomplished. The *Illustris simulation* (Vogelsberger et al., 2014), shown in Fig. 1.7, complements N-body DM halo simulation with hydrodynamic simulations, which are required to model gas, stars, super-massive black holes (SMBHs) and their related energetic feedback. It employs a complete model for galaxy formation physics, which includes the for-mation of both stars and SMBHs, and their effects on their environments in the forms of galactic super-winds driven by star formation, as well as radio bubbles and radiation proximity effects caused by active galactic nuclei (AGNs). Starting approximately 12 million years (Myr) after the Big Bang, the Illustris simulation tracks the evolution of more than 12 billion resolution elements in a volume of (106.5 Mpc)^3 up to the current epoch (redshift z=0) with a dark-matter mass resolution of 6.26×10^6 $M_\odot$, and a baryonic mass resolution of 1.26×10^6 $M_\odot$. The smallest scale over which the hydrodynamics is resolved is 48 pc, whereas gravitational forces are resolved down to 710 pc at z=0 and to even smaller scales at high redshifts (for example, 473 pc at z=2). In this way the Illustris simulation overcame the problems of previous hydrodynamic simulations which either did not cover a large enough portion of the Universe to be representative or lacked adequate resolution.
The simulation allows to self-consistently and simultaneously predict statistics on large scales, such as the distribution of neutral hydrogen or the galaxy population of massive galaxy clus-

[2]Update of the previous *Millenium Simulation* (Springel, 2005).

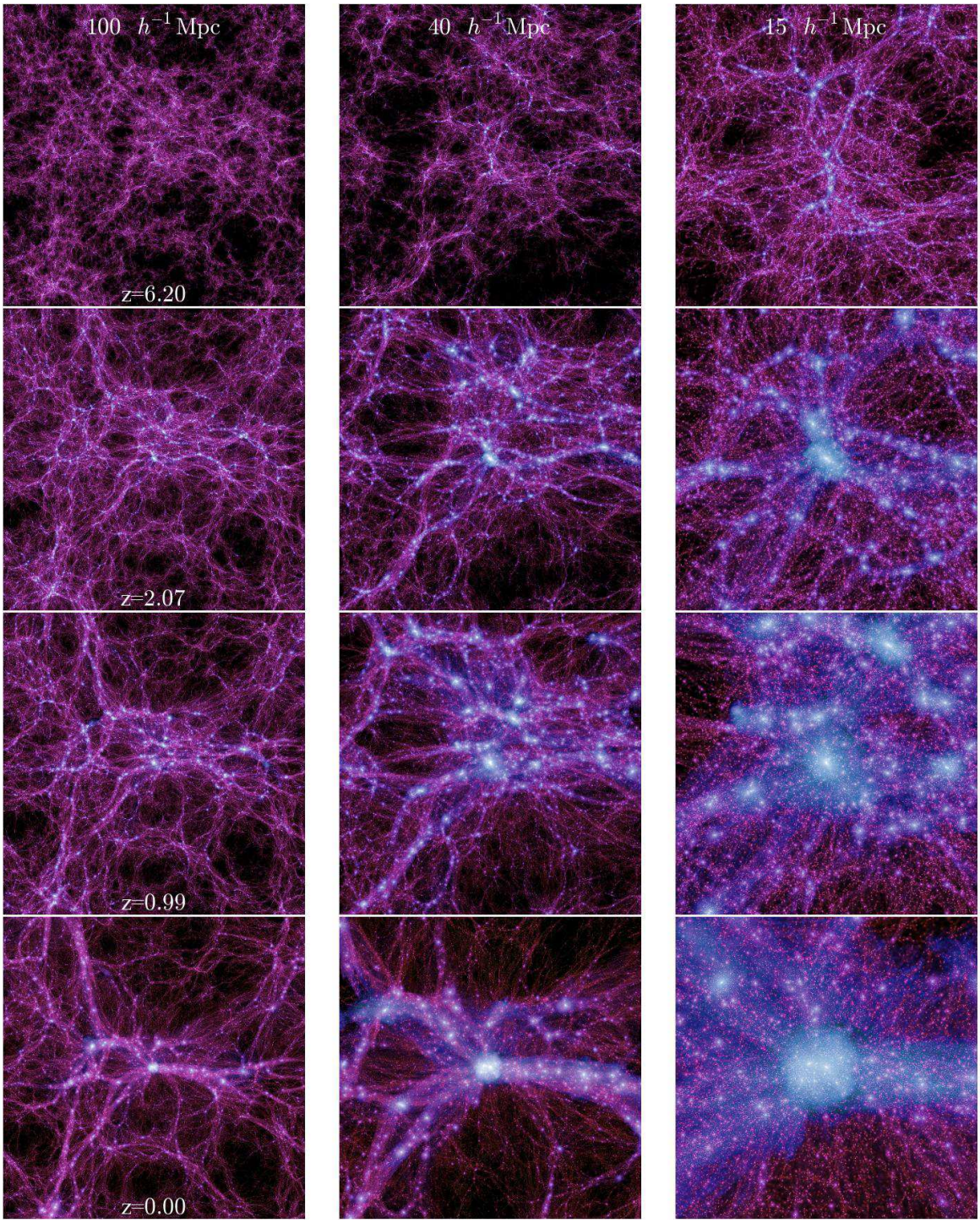

Fig. 1.5: Time evolution of the largest DM halo at z = 0 in the MS-II. The halo is shown at three comoving scales (from left to right: 100, 40 and 15 h^{-1} Mpc, with thickness 15, 10 and 6 h^{-1} Mpc) and at four different cosmological epochs (from top to bottom: z = 6.2, 2.07, 0.99 and 0). Adopted from Boylan-Kolchin et al. (2009).

ters, together with galaxy properties on small scales, such as the morphology and detailed gas and stellar content of galaxies in good agreement with observational data.

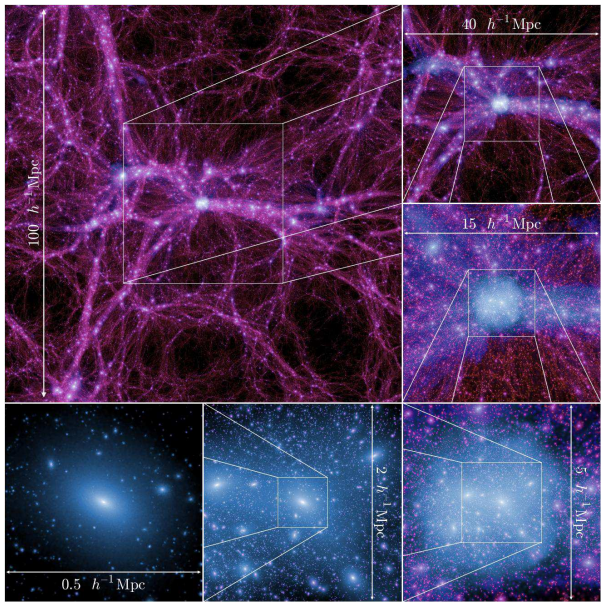

Fig. 1.6: A sequential zoom at z=0 through the MS-II centered on the most massive DM halo in the simulation. Starting from the upper-left and moving clockwise, subsequent panels zoom into the cluster/halo region and show slices that are 100, 40, 15, 5, 2 and 0.5 h^{-1} Mpc on a side (with thicknesses of 10, 6, 5, 2 and 0.5 h^{-1} Mpc). Adopted from Boylan-Kolchin et al. (2009).

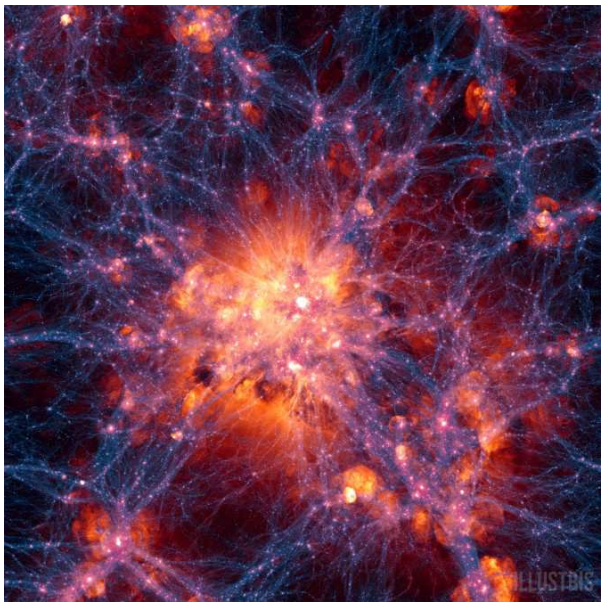

Fig. 1.7: Frame from the Illustris simulation of structure formation. The frame is centered on the most massive simulated galaxy cluster at z=0.The blue-purple filaments show the location of dark matter. Bubbles of red, orange and white show where gas is being blasted outward by supernovae or jets from super-massive black holes. Illustris Collaboration, (Vogelsberger et al., 2014).

The next challenging steps will be to include magnetic fields and cosmic rays in such big simulations.

1.2 Multi-wavelength properties

1.2.1 X-ray properties

Useful reviews about the X-ray properties of galaxy clusters include, e.g., Sarazin (1986), Rosati et al. (2002), Voit (2005), Allen et al. (2011), Reiprich et al. (2013).

With the advent of astrophysics from space in the 1960s, the *Uhuru* satellite revealed that galaxy clusters are the most luminous extended X-ray sources in the sky (Gursky et al., 1972). The X-ray emission observed was very early interpreted as thermal bremsstrahlung from a hot intracluster plasma (Felten et al., 1966). If this plasma is subject to the same gravitational potential as the cluster member galaxies, and if it is in thermal equilibrium, then it is expected to have a typical temperature of (from Rosati et al. (2002)):

$$k_B T \simeq \mu m_p {\sigma_v}^2 \simeq 6 \left(\frac{\sigma_v}{10^3 \mathrm{km\ s^{-1}}} \right)^2 \mathrm{keV}, \tag{1.1}$$

where μ is the mean molecular weight[3], m_p is the proton mass and σ_v is the galaxies' velocity dispersion. Observations show a general correlation between the gas temperature and the galaxies' velocity dispersion, although the big dispersion suggests that the idealized picture of clusters as relaxed structures in which both gas and galaxies share the same dynamics is rather simplified. But it is good to a first approximation. Equation 1.1 implies temperatures for the ICM of the order of T $\sim 10^7$-10^8 K = 1-10 keV. The thermal bremsstrahlung emissivity of such a plasma at frequency ν scales as:

$$\epsilon_\nu \propto n_e n_i g(\nu, T) T^{-1/2} \exp(-h\nu / k_B T), \tag{1.2}$$

where n_e and n_i are the number density of electrons and ions, respectively, and $g(\nu, T)$ is the Gaunt factor. Spectra for typical ICM temperatures are shown in Fig. 1.8. The exponential bremsstrahlung cutoff shifts to higher energies for higher temperatures, as expected from eq. 1.2. In addition to bremsstrahlung, recombination and line emission can be important. At low T, line emission can be the dominant process (Fig. 1.8).
Typical central gas densities are in the range $10^{-3} - 10^{-1}$ cm^{-3}, decreasing rapidly with increasing radius. A popular description the radial profile of the gas density of galaxy clusters is the so-called *β-model*, introduced by Cavaliere & Fusco-Femiano (1976):

$$\rho_g(r) = \rho_{g,0} \left[1 + \left(\frac{r}{r_c} \right)^2 \right]^{-3\beta/2}, \tag{1.3}$$

where β is the ratio of the specific kinetic energies of galaxies and gas.
The assumptions leding to it are those of an ideal, isothermal gas in hydrostatic equilibrium within the potential well associated with a King dark-matter density profile (which includes

[3] μ=0.6 for a primordial composition with a 76 % fraction contributed by hydrogen.

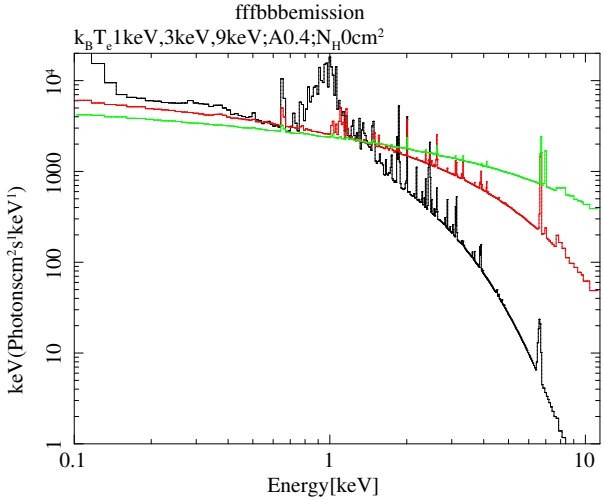

Fig. 1.8: Hot-gas model X-ray spectra as a function of k_BT (black: 1 keV, red: 3 keV, green: 9 keV). Fe L and K shell emission line complexes are visible at ∼1 and ∼6 keV, respectively. The line strength depends on the metallicity (here assumed to be 0.4 solar) and the temperature. Adapted from Reiprich et al. (2013).

the assumption of spherical symmetry), and an isotropic velocity dispersion. Similarly, the X-ray surface brightness (SB) as a function of projected radius R varies as (from Sarazin (1986)):

$$S_X(R) = S_X(0)\left[1 + \left(\frac{R}{r_c}\right)^2\right]^{-3\beta+\frac{1}{2}} . \tag{1.4}$$

The increased angular resolution of present-day's satellites (*Chandra*, *XMM-Newton* and *Suzaku*) allows us to map the X-ray emissivity in detail over larger scales, and showed that a single β-model cannot always describe the density and surface brightness profiles of clusters. It is indeed an adequate description for about 1/3 of the known clusters. Inspection of the SB profiles of some clusters shows the presence of excess emission compared to a single β-model profile in the central regions of the cluster, which indicates the presence of a *cool core*, a clear signature of the dynamically relaxed state of the cluster. An example of a cool-core cluster is XMM2235, shown in Fig. 1.9 (Rosati et al. (2009); see Santos et al. (2008) for a discussion of cool cores in high redshift clusters). In other cases, anomalous discontinuities in the SB, density and temperature profiles may be symptomatic of a disturbed dynamical state. Substructures and irregular morphologies in the X-ray emission may reveal that these clusters are subject to interactions and may be merging with other structures. In the hierarchical structure formation scenario, mergers between (sub-)clusters are common events. A significant fraction of the kinetic energy released in such events goes into shock heating and compression of the ICM and possibly into particle (re-)acceleration. The latter phenomenon is supported by the detection of non-thermal radio emission associated with the diffuse medium (*radio relics and halos*, see Chap. 2). The former can be investigated with deep X-ray observations. The "bullet" cluster 1E 0657-56 provides a textbook example of a disturbed cluster. The second jump in the SB profile (Fig. 1.10, right panel), at around $r \sim 50''$, corresponding to a jump also in the temperature and pressure profiles, reveals the presence of a shock front at that location. The first discontinuity in the SB profile corresponds instead to a *cold front*, since no pressure

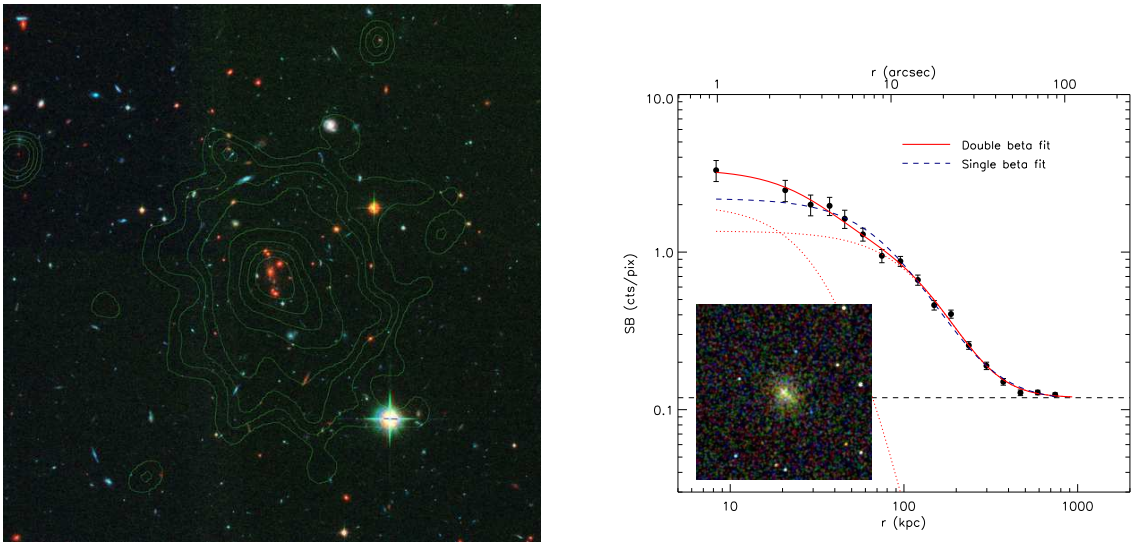

Fig. 1.9: Contours overlaid on an optical image (left panel) and surface brightness profile (right panel) of the Chandra soft X-ray emission from the galaxy cluster XMM2235. The dotted curves indicate the two components of the double-β model (solid line). Note the excess of emission in the central ∼40 kpc region with respect to a single-β model. The inset shows an X-ray color image of the central 2 Mpc region over which the fit is performed. Adapted from Rosati et al. (2009).

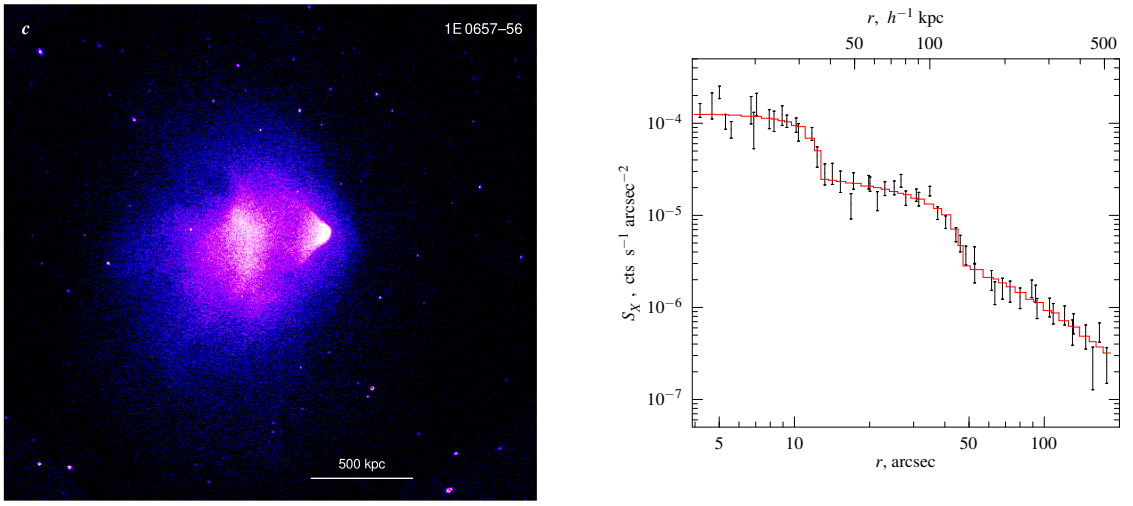

Fig. 1.10: Color image and surface brightness profile of the Chandra X-ray emission of the galaxy cluster 1E 0657-56. Note the two discontinuities in the SB profile: the first at $r \sim 13''$ corresponds to a cold front, while the second at $r \sim 50''$ corresponds to a shock front. Adapted from Markevitch et al. (2002) and Markevitch & Vikhlinin (2007).

jumps and actually a lower entropy behind the front were found. Cold fronts are interpreted as discontinuities because of the motion of cold, dense gas clouds (maybe cool subcluster cores that were not destroyed during previous mergers), through the hotter ICM. Note that cold fronts have also been detected in relaxed clusters, indicating that these are long-living features. A useful review about shocks and cold fronts was given by Markevitch & Vikhlinin (2007). Deep X-ray observations can thus provide a measure of the properties of the shock such as the shock Mach number M and the shock compression ratio C. As we will see in the next chapter, these measures, combined with the properties of the radio emission often observed at the same location, provide important tests to study particle acceleration in galaxy clusters. However, such shocks usually occur in the outskirts of clusters, where the very low density of electrons ($n_e < 10^{-4} cm^{-3}$) make their detection in the X-ray regime very challenging (Reiprich et al., 2013). Indeed, a few clear X-ray shock detections are known in literature (see Brüggen et al. (2012)).

1.2.2 Properties at mm wavelengths (SZ)

Useful reviews about SZ properties of galaxy clusters include, e.g. Carlstrom et al. (2002).

Clusters of galaxies can be seen at mm wavelengths thanks to the effect they have on the CMB spectrum, known as the *thermal Sunyaev-Zeldovich effect* (SZE) (Sunyaev & Zeldovich, 1970). This effect is due to Inverse Compton scattering to higher energies of the photons of the CMB that interact with the hot electrons passing through the ICM of a galaxy cluster. The effect depends on the pressure produced by the cluster plasma along the line of sight, and hence on its density. The SZ effect produces a modification of the CMB blackbody spectrum that, expressed as the specific intensity change ΔI_{SZ} at dimensionless frequency $x = h\nu/k_B T_{CMB}$, is given by (Carlstrom et al., 2002):

$$\Delta I_{SZ} = 2\frac{(k_B T_{CMB})^3}{(hc)^2} \cdot \frac{x^4 e^x}{(e^x - 1)^2} \left(x\frac{e^x + 1}{e^x - 1} - 4 \right) \cdot y, \tag{1.5}$$

where y is the *Comptonisation parameter* that depends on the pressure P produced by the plasma along the line of sight l:

$$y = \frac{\sigma_T}{m_e c^2} \int P(r) dl. \tag{1.6}$$

The SZE appears as a decrease in the blackbody intensity of the CMB at lower frequencies, in the *Rayleight-Jeans regime* ($x \ll 1$), where clusters will appear as "cold spots" on the CMB, and as an increase at higher frequencies, in the *Wien regime* ($x \gg 1$), where clusters will appear as "hot spots" on the CMB.

The SZE is best known for allowing the determination of cosmological parameters, when combined with other observational diagnostics of clusters of galaxies such as X-ray emission from the intracluster gas, weak and strong lensing by the cluster potential, and optical galaxy velocity dispersion measurements. The remarkable property of the SZ effect is that, unlike the CMB emission itself, the modification on it that it induces, does not suffer from cosmological dimming with redshift. This makes the SZ effect a direct, redshift independent measurement of the ICM column density weighted by temperature, i.e. the pressure integrated along the

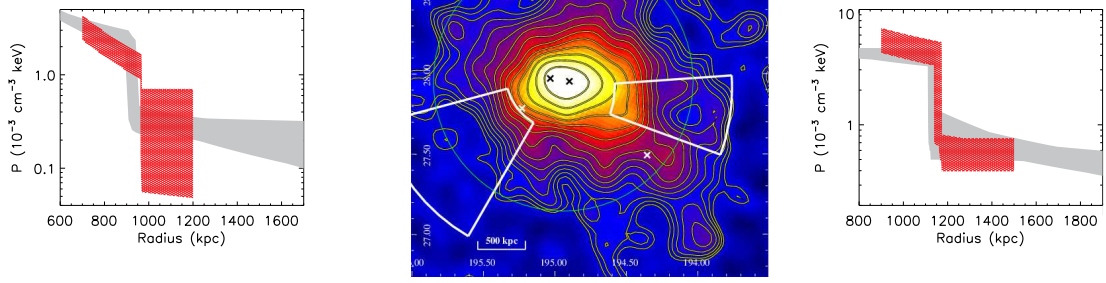

(a) 3D-pressure model for the west sector.

(b) Planck y map of the Coma cluster.

(c) 3D-pressure model for the south-east sector.

Fig. 1.11: The central panel shows the Planck y map of the Coma cluster. The contour levels are logarithmically spaced by $2^{1/4}$. The green circle indicates R_{500} (R_{500} determines the spherical region within which the mean enclosed density is 500 times the critical density of the Universe). White and black crosses indicate the position of the brightest galaxies in the Coma cluster. The white sectors indicate two regions where the y map shows a local steepening of the radial gradient, shown in the side panels. The 68.4% confidence level range of the 3D-pressure model for the west and south-east sectors are shown in the right and left panels respectively. Grey shaded regions are the profiles derived from the Planck data. Red regions are the profiles derived from the XMM-Newton data. Adapted from Planck Collaboration et al. (2013b).

line of sight. SZE surveys will therefore be able to detect all clusters above a mass limit, independent of the redshift of the clusters, offering an ideal tool for determining the cluster density evolution. The Planck satellite provided an invaluable contribution to this field.

Moreover, high-resolution SZ observations of single clusters nicely complement X-ray studies of the properties of the ICM. This is particularly useful in studying the outskirts of clusters, where the X-ray surface brightness is low but the SZ signal remains substantial. Here, SZ observations may reveal pressure/density jumps due to shocks believed to be responsible of the non-thermal radio emission observed in many clusters, and it helps in putting constraints on the shock properties, such as the Mach numbers and compression ratio. For example, the Coma cluster is the most spectacular SZ source in the Planck sky (Figs. 1.1c and 1.11). It is a low-redshift, massive, and hot cluster, and is sufficiently extended that Planck could resolve it well spatially, allowing to study the underlying pressure distribution of the ICM. Planck detected a localised steepening of the y profile about half a degree to the west and also to the south-east of the cluster centre (Fig. 1.11). Features in the X-ray and radio synchrotron profiles at similar locations suggest the presence of shock waves that propagate with Mach number $M_W = 2.03^{+0.09}_{0.04}$ and $M_{SE} = 2.05^{+0.25}_{0.02}$ in the west and south-east directions, respectively (Planck Collaboration et al., 2013b).

1.2.3 Radio properties

For reviews of the radio properties of galaxy clusters, see e.g. Feretti et al. (2012), Brüggen et al. (2012) and Ferrari et al. (2008).

A fraction of clusters of galaxies manifests diffuse Mpc-scale synchrotron emission in the radio band, not related to any particular cluster member galaxy. This diffuse emission comes from three different classes of sources: *radio relics*, *radio halos* and *radio mini-halos*. The first two classes of sources are the object of this thesis and they will be described in a dedicated chapter (Chap 2).
Radio mini-halos are diffuse sources with moderate extent ($\sim 500\ h_{50}^{-1}$ kpc) that surround a powerful radio galaxy at the center of a *cooling core* cluster. Although the more natural explanation would invoke a connection between the central galaxy and the diffuse emission, mini-halos do not show the common morphology of active radio galaxies where extended lobes are maintained by the central Active Galactic Nuclei (AGN). The mini-halo emission is instead believed to originate from relativistic particles and magnetic fields which are deeply mixed with the thermal ICM gas and must be distinguished from other morphologies where the detected radio emission is contained within *cavities* devoid of X-ray emitting gas.
The main difference between radio mini-halos and the bigger radio halos, discussed in the next section, is that the first are observed in relaxed cool core clusters, while the latter are observed in clusters with evidence of major mergers. This suggest a connection between mini-halos and the presence of cool cores, and rules out that they are simply smaller radio halos or radio halos in a different evolutionary stage. Gitti et al. (2002) proposed that mini-halos result from a relic population of relativistic electrons re-accelerated by MHD turbulence via Fermi-like processes, the necessary energetics being supplied by the cool-core region. We will see in Chapter 2 that radio halos are produced by similar acceleration processes powered by major mergers. However, observations of the galaxy cluster RXJ 1347.5-1145 (Fig. 1.12, Gitti et al. (2007)) revealed the presence of a cool core cluster with signatures of merging activity and hosting a radio mini-halo. This suggests that additional energy for electron re-acceleration in mini-halos might be provided by sub-cluster mergers that have not been able to destroy the central cluster cool core. Pfrommer & Enßlin (2004) proposed that emission from mini-halos could arise from electrons produced by proton-proton collisions in the dense cool-core regions. Finally, the possibility has been advanced that the relativistic electrons in mini-halos may get re-accelerated by turbulence in the core, induced by *gas sloshing* (ZuHone et al., 2011).
Combining the difficulties in the detection of radio mini-halos due to their relatively small angular size and the strong radio emission from the central galaxy with the difficulties in the classification, by the time of the last review from Feretti et al. (2012) no more than 11 mini-halos were known. The list is given in Table 5 of Feretti et al. (2012).

1.2.4 EUV-SXR/HXR properties

For reviews see Durret et al. (2008), Petrosian et al. (2008) and Rephaeli et al. (2008).

With the advent of telescopes sensible to low X energies (ROSAT-PSPC, the Extreme Ultra-Violet Explorer (EUVE) Satellite, XMM-Newton) it has been found that ~30 % of the galaxy clusters exhibit an excess emission over the extrapolation of the usual thermal emission from the hot ICM (Sect. 1.2.1) to the extreme ultraviolet and soft X-ray ranges. This value is based on the two largest samples of galaxy clusters with a soft x-ray excess (Bonamente et al. (2002); Kaastra et al. (2003)). However, the detection and interpretation of the soft x-ray excess are still being debated vigorously (e.g. Bowyer et al. (2004), Bregman & Lloyd-Davies (2006)).

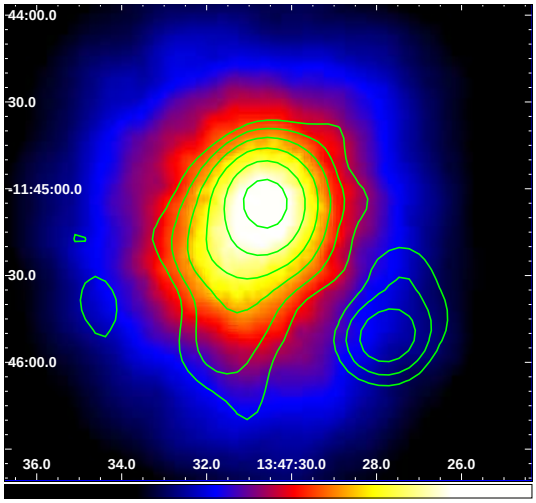

Fig. 1.12: Radio mini-halo in the galaxy cluster RXJ 1347.5-1145. Contours represent the 1.4 GHz diffuse radio emission overlaid on a color scale of the adaptively smoothed XMM-Newton image of the central region of the cluster. Adopted from Gitti et al. (2007).

The first mention of soft excess emission in the 0.065-0.245 keV band was made by Lieu et al. (1996b) and Lieu et al. (1996a) for the Virgo cluster, based on data obtained with the EUVE satellite and for the Coma cluster, based on EUVE and ROSAT data. The first interpretation by Lieu was that the soft excess emission was of thermal origin. The Coma cluster is a good case for a cluster where the soft excess is dominantly of thermal nature. Bonamente et al. (2003) proposed that the soft component may reside in external filamentary structures of a warm-hot (10^5-10^6 K) intergalactic medium (WHIM), which are predicted by hydrodynamical simulations of the formation and evolution of large-scale structures (Yoshikawa & Sasaki, 2006). A second model, proposed by Sarazin & Lieu (1998), favors a non-thermal origin for the excess emission. In this model the soft excess is due to the IC emission of CMB photons on a population of cosmic rays electrons, which could have been produced by supernovae, radio galaxies or by particle acceleration in intra-cluster shocks. This non-thermal model best explains the observed properties of the soft excess in the cluster Sersic 159-03 (Werner et al., 2007).
Other models that may account for the soft excess may be found in, e.g., Enßlin et al. (1999), Sarazin & Kempner (2000), Petrosian (2001), De Paolis et al. (2003).

Some of the non-thermal mechanisms suggested to account for the soft excess emission can also explain the hard X-ray emission detected in some clusters. Indications for emission at energies $\geq$ 20 keV (where thermal bremsstrahlung falls off exponentially with energy) came after deep dedicated observations of a few clusters with the RXTE and BeppoSAX satellites (Rephaeli et al. (1999); Fusco-Femiano et al. (1999). As for the soft excess, the detections are still controversial (Rossetti & Molendi (2004), Renaud et al. (2006), Rephaeli et al. (2006)). The extent and strength of these emissions has been disputed (e.g. analyses of Swift/BAT observations by Ajello et al. (2009) and Suzaku observations by Wik et al. (2009)). The most natural non-thermal process for this excess is the IC scattering of the CMB photons by the same population of relativistic electrons responsible for the radio-synchrotron emission. Non-thermal HXR emission from galaxy clusters due to Compton scattering of CMB photons in clusters with diffuse radio emission was indeed predicted more than 30 years ago (Rephaeli, 1977).

Some authors (see e.g. Enßlin et al. (1999), Blasi (2000)) suggested instead that the HXR radiation is due to non-thermal bremsstrahlung by a second population of non-thermal electrons with a power-law distribution in the 10 to 100 keV range. However, these hypotheses seem to be ruled out by energetic considerations, because of the well known inefficiency of the proposed non-thermal bremsstrahlung mechanism.

1.2.5 γ-ray properties

For reviews on gamma ray properties of galaxy clusters see, e.g., Blasi et al. (2007).

Galaxy clusters are unique reservoirs of cosmic-ray (CR) hadrons. It is expected that relativistic protons are the dominant non-thermal component of cluster, due to their long life-time and consequent confinement on Hubble time scale (Blasi et al., 2007). This provides the possibility of proton-proton collisions that produce gamma emission through the decay of π^0 ed inject secondary particles. On the other hand, it has been suggested (Bykov et al. (2000), Miniati (2003)) that the detection of gamma-ray emission from clusters may not necessarily reflect the hadronic origin of cosmic rays, since it could be related to the Compton scattering of CMB photon from shock-accelerated, intracluster electrons. We have seen in the previous sections that the presence of thermal particles in the ICM results in a distortion of the Cosmic Microwave Background (CMB) spectrum known as Sunyaev-Zeldovich effect, and similarly non-thermal hard X-ray (HXR) photons may be produced via Compton scattering by the same cosmic rays that are responsible for the synchrotron emission observed at radio wavelengths. Compton scattering increases the frequency of the incoming photon. For typical energies of relativistic electrons in clusters ($\gamma_L \sim$ 1000-5000), the scattered photons can fall also in the gamma-ray domain. The most promising insight into gamma ray emission from galaxy clusters was expected to come from *Fermi-LAT* observations, however, only upper limits and no detection have been derived (Fig. 1.13; Ackermann et al. (2010)).

An additional source of GeV gamma rays could be the decay or annihilation of dark matter particles.

1.3 Magnetic fields in galaxy clusters

For reviews see, e.g., Widrow (2002), Carilli & Taylor (2002), Govoni & Feretti (2004).

The existence of magnetic fields associated with the intracluster medium in clusters of galaxies is now well established through different methods of analysis. Direct evidence of the presence of cluster magnetic fields is provided by the detection of diffuse synchrotron radio emission (radio mini-halos, Sect. 1.2.3, radio relics and radio halos, Chap. 2). The synchrotron emission is produced by the helical motion of relativistic electrons in a magnetic field. It is therefore the easiest and more direct way to detect and study the properties of magnetic fields in astrophysical sources. The total synchrotron emission from a source provides an estimate of the strength of magnetic fields, while the degree of polarization is an important indicator of the field uniformity and structure. Assuming *energy equipartition* between particles and fields, a qualitative indication of the magnetic-field strength can be made using the synchrotron intensity of the radio diffuse emission of the cluster (e.g. Giovannini et al.,

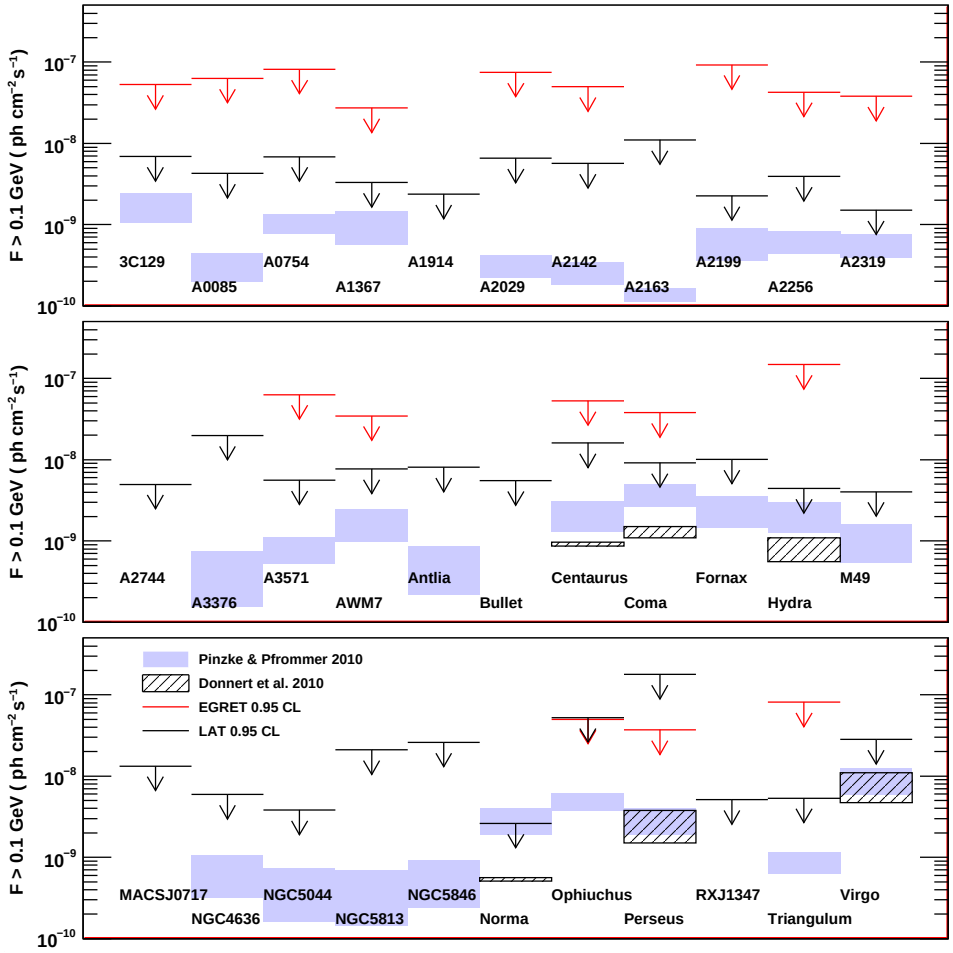

Fig. 1.13: Upper limit of the photon flux derived from Fermi-LAT observations of galaxy clusters (assuming unresolved gamma-ray emission), compared with EGRET results (Reimer et al., 2003) and with predictions based on the numerical simulations of Pinzke & Pfrommer (2010) and Donnert et al. (2010). Adopted from Ackermann et al. (2010).

1993; Thierbach et al., 2003). The synchrotron emission of such sources requires a population of $\sim$ GeV relativistic electrons and cluster magnetic fields on μG levels (Feretti et al., 2012; Brüggen et al., 2012; Ferrari et al., 2008). Observations indeed show that cluster fields are at the μG level, with values of up to tens of μG at the center of cooling-core clusters. The magnetic field is not constant through the cluster and shows a complex structure, fluctuating over a wide range of spatial scales with values from a few kpc up to hundreds kpc. Theoretical studies have shown that an integral part of particle acceleration in strong shocks is the magnetic field compression, amplification and alignment with the shock front (Lucek & Bell, 2000; Bell, 2004). Recent simulations by Iapichino & Brüggen (2012) predict strong magnetic fields aligned with the shock surface of the order of 6 μG at 0.5 R_{vir}, which are in agreement with observations of the polarization properties of cluster radio relics.
An indirect evidence of the existence of magnetic fields in clusters is also derived from studies of the Rotation Measure of radio galaxies located within or behind clusters of galaxies (e.g. Bonafede, 2010).

The detection of non-thermal HXR and radio emission produced by the same population of relativistic electrons allows to estimate unambiguously the volume-averaged intracluster magnetic field. Moreover, as discussed, both primary and secondary electrons produce radio waves via synchrotron radiation and possibly gamma rays by IC scattering of soft ICM photons. For clusters with measured radio flux and knowledge of particle and soft-photon densities, upper limits on gamma-ray fluxes can constrain the volume-averaged value of the magnetic field (Ackermann et al., 2010).

The origin of magnetic fields in galaxy clusters is still debated. They might originate in the early Universe, either before or after recombination, or they could have been deposited in the intracluster medium by starburst galaxies or AGN. In either case, magnetic fields undergo significant amplification during the cluster merger processes (Dolag et al., 2008).

Chapter 2

Radio relics and radio halos in clusters of galaxies

A fraction of galaxy clusters exhibits diffuse Mpc-scale synchrotron emission (referred to as *radio relics* and *radio halos*) not related to any particular cluster galaxy (for reviews see Ferrari et al., 2008; Feretti et al., 2012; Brüggen et al., 2012). This emission manifests itself by the presence of relativistic electrons (∼GeV) and weak magnetic fields (∼ μG) in the intracluster medium (ICM), together with the hot thermal plasma emitting X-rays. Even though the existence of radio relics and halos has been known for three decades, their origin is as yet debated. The main difficulty in explaining such extended emissions arises from the combination of their Mpc size, and the relatively short radiative lifetime of the emitting electrons. Such diffuse sources therefore require some form of in-situ production or (re-)acceleration of the electrons (Jaffe, 1977), even though the underlying physical mechanisms are thought to be different for the different classes of sources. Moreover, these diffuse radio emitting regions are mostly found in unrelaxed clusters, suggesting that cluster mergers play a key role in producing them. Indeed, mergers drive shocks and turbulence in the ICM that may lead to the amplification of the magnetic fields (e.g. Dolag et al., 2002; Subramanian et al., 2006; Ryu et al., 2008) and to the acceleration of high-energy particles.
Some galaxy clusters host both a radio halo and a radio relic, some host a double radio relic system. Figure 2.1 displays a collection of clusters showing several types of diffuse radio emission.

2.1 Radio relics

The term radio relic is used in literature to refer in general to irregularly shaped diffuse synchrotron sources observed in the outskirts of clusters of galaxies. Due to this broad classification criterion, different kinds of sources with significantly different observational properties fall into this class. Besides the irregular shape, other common characteristics are a low surface brightness, a steep integrated radio spectrum ($\alpha \geq 1$, $S_\nu \propto \nu^{-\alpha}$) and a medium-to-high level of polarization (up to 40 %; see Fig. 2.2).

Relics are observed toward the periphery of clusters in both merging and cool-core systems, suggesting that they may be related to minor or off-axis mergers, as well as to major-merger events. They are detected up to redshifts z ∼ 0.4. The low number of high-redshift relics could be due to selection effects, or could also be a real trend due to the evolution of the cluster mergers rate, or to the increasing relevance of inverse Compton losses with z (Feretti et al., 2012).

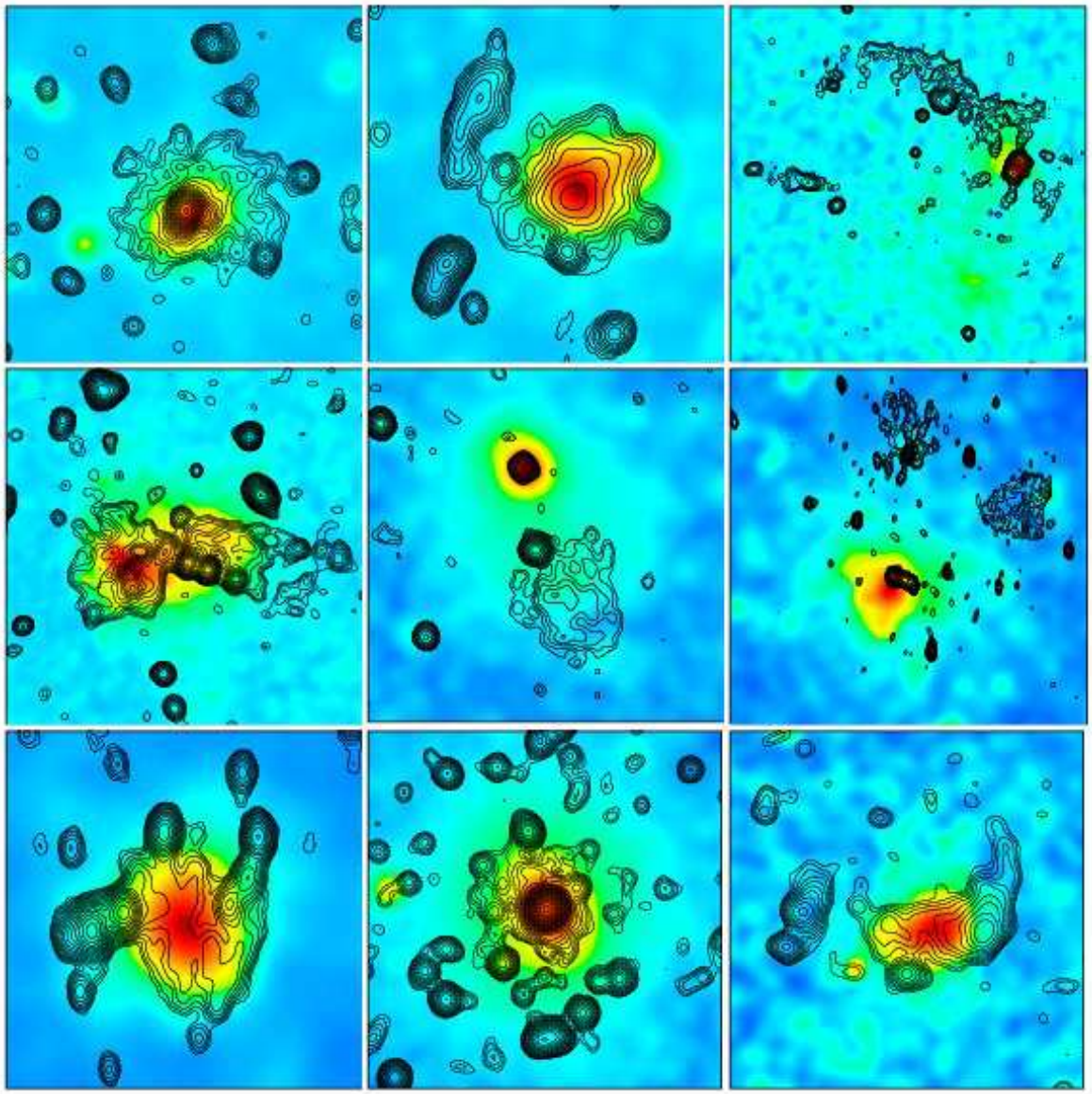

Fig. 2.1: Collection of galaxy clusters showing several types of radio emission, shown in contours, overlaid onto the X-ray emission, shown in colors. Clusters are (from left to right and from top to bottom) A 2219 (halo, Bacchi et al., 2003), A 2744 (halo + relic, Govoni et al., 2001), A 115 (relic, Govoni et al., 2001), A 754(complex, halo plus relic, Bacchi et al., 2003), A 1664 (relic, Govoni et al., 2001), A 548b (relic, Feretti et al., 2006), A 520 (halo, Govoni et al., 2001), A 2029 (mini-halo, Govoni et al., 2009), RXCJ1314.42515 (halo plus double relics, Feretti et al., 2005). Adopted from Feretti et al. (2012).

Giovannini et al. (1999) showed that the occurrence of relics in a sample from the NVSS[1] is higher in clusters showing a high X-ray luminosity.
Relics are further subdivided into three classes: *radio gischt*, *radio phoenices* and *AGN relics* (see Kempner et al., 2004), depending on their characteristics and proposed origin.
Radio gischt or *giant radio relics* are large extended arc-like sources, believed to be syn-

[1]NRAO VLA Sky Survey.

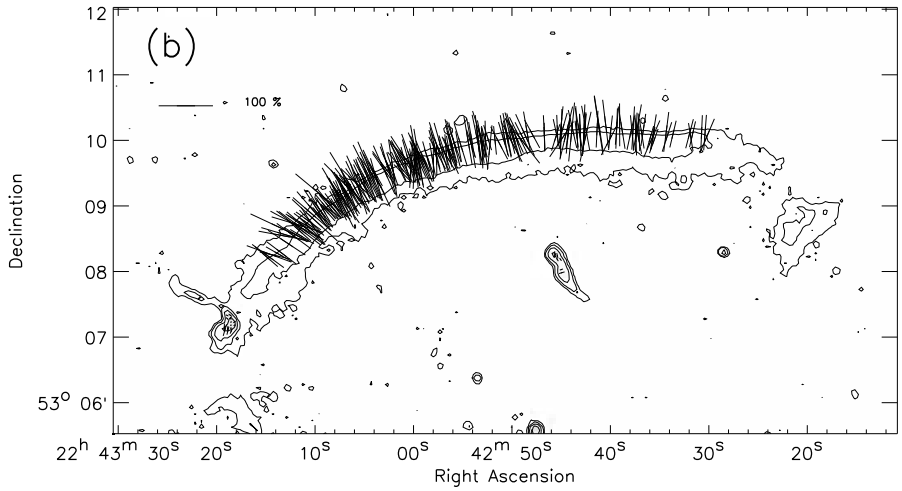

Fig. 2.2: The radio relic in CIZAJ2242.8+5301: contours represent the total intensity emission obtained with thw GMRT at 610 MHz. Superimposed bars represent the polarization electric field vectors obtained with the VLA at 4.9 GHz. Adopted from van Weeren et al. (2010).

chrotron emission from electrons (re-)accelerated in merger or accretion shocks, through diffusive shock acceleration (DSA; Enßlin et al., 1998; Kang & Ryu, 2011, see Sect. 2.3.2). A textbook example of such giant radio relic has been observed in the galaxy cluster CIZA J2242.8+5301 (Figs. 2.2 and 2.7 from van Weeren et al., 2010; Stroe et al., 2013). *Radio phoenices* are smaller structures believed to be the result of the re-energization, via adiabatic compression, of fossil plasma from former radio galaxies where the AGN creating the radio lobes had switched off. The adiabatic compression is believed to be triggered when a merger or accretion shock passes through such a faded relic radio galaxy (Enßlin & Gopal-Krishna, 2001; Enßlin & Brüggen, 2002). An example of a radio phoenix has been found in the galaxy cluster A2443 (Fig. 2.9c from Cohen & Clarke, 2011). *AGN relics* are such fossil radio galaxies where the AGN switched off more recently and no re-energization occurred. The plasma is still emitting at observable radio frequencies and it simply evolves passively until it will become invisible in the radio regime (Komissarov & Gubanov, 1994).
In the last review from Feretti et al. (2012), radio relics have been classified using only morphological criteria, viz. *elongated* vs. *roundish*. In first approximation, elongated relics correspond to the giant radio relics of Kempner's classification, while roundish relics correspond to radio phoenices. We point to Table 3 of the review for a collection of known radio relics updated to September 2011. They show that roundish sources are more concentrated towards the cluster center, while elongated relics are mostly located between 0.5 and 1.5 Mpc from the center, up to a distance of 3 Mpc (see Fig. 2.3 left panel). Moreover, elongated relics show the spectral index α in the range 1.0 - 1.6, with an average value of 1.3, while spectral indices of roundish relics span a larger range of values, 1.1 - 2.9, with an average value of 2.0 (see Fig. 2.3 right panel).

Some of the most extended and powerful giant relics are located in clusters with central radio halos (as in the case of Abell 2256, Clarke & Ensslin, 2006). The cases of double relics in the same cluster are getting more and more common since the first discov-

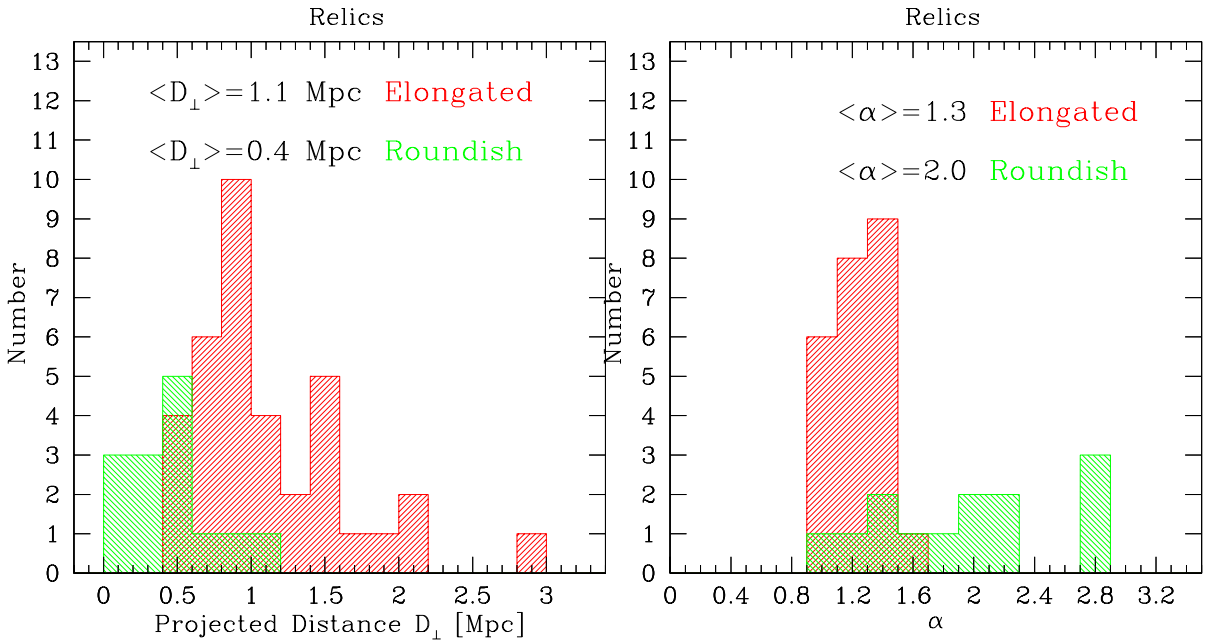

Fig. 2.3: Left panel: Distribution of relics according to their projected distance from the cluster center. Right panel: Spectral index distribution of relics. Adopted from Feretti et al. (2012).

ery of two almost symmetric relics located on opposite sides in A3667 (Rottgering et al., 1997; Johnston-Hollitt et al., 2002). Since then, several other objects have been found (see Feretti et al., 2012). We will see that this is expected in a scenario in which relics are manifesting the presence of shock waves caused by mergers between clusters with approximately equal masses.

Finally, in few cases the presence of a shock front at the location of the radio relic has been proven though X-ray observations via density and/or temperature jumps (e.g. Markevitch et al., 2002; Krivonos et al., 2003; Markevitch et al., 2005; Giacintucci et al., 2008; Russel, 2010; Finoguenov et al., 2010). However, relics are usually observed in the outskirts of clusters where the very low density of electrons ($n_e < 10^{-4}$ cm^{-3}) make the detection of shocks in the X-ray very challenging (Akamatsu & Kawahara, 2011). Indeed, only a few clear X-ray shock detections are known in literature (see review by Brüggen et al., 2012).

2.2 Radio halos

The term *radio halos* is used to indicate low-surface brightness extended radio sources permeating the central Mpc^3 of clusters. Their radio morphology is quite regular and follows the X-ray emitting thermal gas. The main difference to radio relics is that they are unpolarized down to a few percent in the majority of cases. The only successful detections of polarized filamentary emission connected with a radio halo have been found in the galaxy clusters A2255 (Govoni et al., 2005; Pizzo et al., 2011) and MACS J0717.5+3745 (Bonafede et al., 2009).
Their low surface brightness (usually lower than radio relics), steep spectra and large angular sizes makes their detection difficult. As for relics, the occurrence of halos in the NVSS sample increases with increasing X-ray luminosity of the host cluster (Giovannini et al., 1999). The *GMRT Radio Halo Survey*[2] (Venturi et al., 2007, 2008) has provided a significant improvement of the statistics of radio halo occurrence. This survey consists of 610 MHz observations of a complete sample of 50 X-ray-luminous galaxy clusters in the redshift range 0.2 - 0.4 (with $L_X \geq 5 \cdot 10^{44}$ erg/s, taken from the REFLEX and the extended BCS catalogues, Böhringer et al., 2004; Ebeling et al., 1998, 2000). Large-scale synchrotron emission at the level of presently known radio halos was found only in $\sim$ 30% of the selected clusters (Venturi et al., 2008), confirming that this fraction depends on the cluster X-ray luminosity (Cassano et al., 2008). Figure 2.4 (from Brunetti et al., 2009) shows the distribution of the GMRT galaxy clusters (blue) and other clusters hosting giant radio halos from the literature, in the plane of X-ray thermal luminosity in the energy range 0.1 - 2.4 keV ($L_{[0.1-2.4]keV}$) vs the non-thermal radio power at 1.4 GHz ($P_{1.4GHz}$). The distribution follows a *bimodal behavior*, with radio-halo clusters tracing a $P_{1.4}$ - L_X correlation and radio-quiet clusters (without radio halo; upper limits indicated by arrows in Fig. 2.4) clearly separated. Since the X-ray luminosity is directly related to the cluster mass, the $P_{1.4}$ - L_X correlation suggests that gravity provides the reservoir of energy to generate the non-thermal components in the ICM. However, clusters with similar thermal properties (X-ray luminosity and hence mass) are expected to have a similar probability to possess radio halos. The observed differences in terms of non-thermal cluster properties should therefore be understood by assuming different evolutionary stages of these clusters and a *transient* radio halo nature. Radio-halo clusters, always dynamically disturbed systems, must be the "youngest" systems, where an ongoing merger is still supplying energy to maintain the synchrotron emission. On the other hand, radio-quiet clusters, typically more relaxed than radio halo clusters (Venturi et al., 2008), must have experienced the last merger at earlier epochs and had sufficient time for the decline of the synchrotron emission. Consequently they should be the "oldest" systems in the GMRT sample. Clusters in the "empty" region may be either intermediate systems at late merging phases, where synchrotron emission is being suppressed, or the very young systems in the very early phases of a merging activity, where synchrotron emission is still increasing. Brunetti et al. (2009) estimated that the life-time of radio halos is $\sim$ 1.3 Gyr, the time interval that clusters may spend in the empty region is $\sim$ 180 Myr and the corresponding time-scale for suppression of the cluster-scale synchrotron emission from the level of radio halos to that of radio quiet clusters is roughly 90 Myr. Buote (2001) provided the first quantitative comparison of the dynamical states of clusters possessing radio halos. He used power ratios that relate the gravitational potential fluctuations to the X-ray substructure

[2]Performed with the Giant Metrewave Radio Telescope (GMRT) run by the National Centre for Radio Astrophysics of the Tata Institute of Fundamental Research.

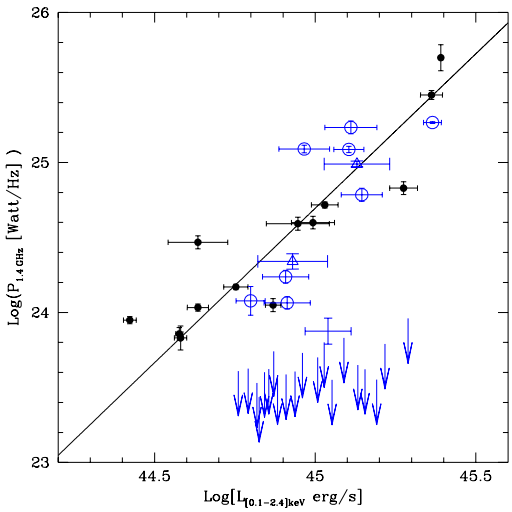

Fig. 2.4: Distribution of GMRT galaxy clusters (blue) and of other radio-halo clusters from the literature (filled black symbols) in the $P_1.4$ L_X(0.1-2.4 keV) luminosity plane. Empty circles mark giant radio halos from the GMRT sample, empty triangles mark the two mini-halos in cool-core clusters from the GMRT sample. The cross marks the position of RXJ1314, and arrows mark upper limits of GMRT clusters with no evidence of Mpc-scale radio emission. The solid line gives the best fit to the distribution of giant radio halos. Adopted from Brunetti et al. (2009).

to describe the dynamical state of a cluster, and found that they correlate with the radio power at 1.4 GHz ($P_{1.4GHz}$), i.e. the strongest radio halos appear only in those clusters currently experiencing the largest departures from a virialized state. The association of radio halos with massive, disturbed core-disrupted clusters can account for both the vital role of mergers in accelerating the relativistic particles responsible for the radio emission as well as for the rare occurrence of radio halos in cluster samples.
However, radio halos in under luminous X-ray clusters, i.e. outside the correlation between radio power and X-ray luminosity, have been found in few cases (Giovannini et al., 2009, 2011; Brown et al., 2011).
We point to Table 1 of Feretti et al. (2012) for a collection of known radio halos updated to September 2011.

2.3 Models and spectral behavior

The observed radiation from radio relics and halos is synchrotron emission from cosmic ray (CR) electrons with Lorentz factors[3] $\gamma \geq 10^4$ moving in $\sim \mu$G magnetic fields diffuse in the ICM. The cooling timescale of such CR electrons due to synchrotron and IC emission is of the order of $\sim 10^8$ yr. Advection or diffusion over this time scale would typically be limited to ≤100 kpc. So, the electrons have very likely been injected, accelerated, or re-accelerated close to where they are seen in emission. This is true for both relics and halos, although the proposed mechanisms at play in the different classes of sources are thought to be different.

2.3.1 Synchrotron spectra

Instantaneous synchrotron spectra

Synchrotron radiation is generated from charged particles that undergo acceleration in a magnetic field. A particle with charge q and mass m moving with velocity $\vec{v}$ in a magnetic field $\vec{B}$ assumed to be uniform[4] undergo the Lorentz force :

$$\frac{d\vec{p}}{dt} = \frac{q}{c}\vec{v} \times \vec{B} \tag{2.1}$$

where $\vec{p} = m\vec{v}$ is the particle's momentum.
If we call χ the angle between the directions of $\vec{p}$ and $\vec{B}$ (*pitch angle*), and with $v_{\parallel} = v \cdot cos\chi$ and $v_{\perp} = v \cdot sin\chi$ the components of $\vec{v}$ in the directions respectively parallel and perpendicular to the direction of the field $\vec{B}$, from eq. 2.1 we have:

$$\frac{d(mv_{\parallel})}{dt} = 0 \Rightarrow v_{\parallel} = const \tag{2.2}$$

and

$$\frac{d(mv_{\perp})}{dt} = \frac{q}{c}v_{\perp} \times \vec{B}. \tag{2.3}$$

Therefore the motion is uniform translational along the field lines (eq. 2.2), while in the direction perpendicular to the field the motion is uniform circular around the magnetic field lines, with centripetal acceleration (eq. 2.3) and curvature (called *Larmor radius*) $r_L = mcv_{\perp}/qB$. If the particle is relativistic (with $\gamma \gg 1$) then the Larmor radius is $r_{rel} = E/qB$, where $E = m_0c^2\gamma$ is the total particle energy. On the whole, the motion is helical with the axes parallel to the magnetic field lines (see Fig. 2.5). The pitch angle is important: if particles stream along the magnetic field line with no perpendicular component, they will not get centripetally accelerated and will not emit synchrotron radiation (eq. 2.3). In the other limiting case, a particle will emit the maximum synchrotron power when it will pitch the magnetic field line perpendicularly. The whole range of pitch angles (between 0° and 90°) and consequent synchrotron powers are expected.

It is well known that when charged particles are accelerated, they emit radiation according

[3]The Lorentz factor is defined as $\gamma := (1 - v^2/c^2)^{-1/2}$.
[4]It is sufficient that the field is uniform on scales bigger than the Larmor radius.

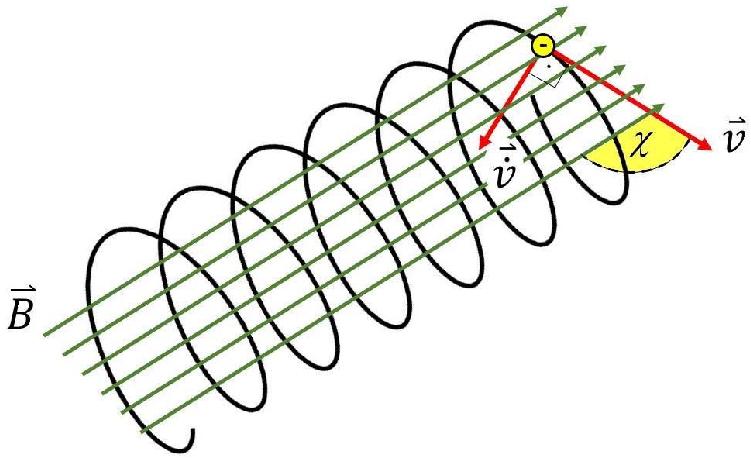

Fig. 2.5: Schematic view of the synchrotron emission process.

to Larmor's law. In case of relativistic particles with energy E moving in a uniform magnetic field B, the synchrotron power emitted is given by:

$$P = \frac{2}{3}\frac{q^4}{m_o^4 c^7} \cdot E^2 B^2. \tag{2.4}$$

Although in the reference system of the particle the emission is isotropic, an observer will see the bulk of the radiation concentrated in a cone with semi-amplitude $\approx 1/\gamma$ (along the instantaneous direction of velocity) for a relativistic beaming effect. Indeed, the angular distribution of the energy emitted by a particle moving with relativistic speed results heavily concentrated in the direction of the velocity. As a consequence, as the particle moves along its orbit, a fixed observer will receive the radiation only when its line of sight intercepts this cone. The synchrotron emission from a single particle is then impulsive. The spectral distribution of the radiation $S_e(\nu)$ is obtained through a Fourier analysis of the impulse. It will contains all frequencies up to a critical value inversely dependent on the duration of the impulse τ given by:

$$\nu_{e,c} \sim \frac{3}{4\pi}\frac{1}{\tau} = \frac{3}{4\pi}\frac{eB_\perp}{m_e c}\gamma^2 = \frac{3}{4\pi}\frac{eB_\perp}{m_e^3 c^5}E^2 \simeq 0.4\left(\frac{\gamma}{10^4}\right)^2\left(\frac{B_\perp}{\mu G}\right)\mathrm{GHz} \tag{2.5}$$

where $B_\perp = Bsin\chi$. At frequencies above the critical one the spectrum will have an exponential cut-off, $S_e(\nu) \propto e^{-(\nu/\nu_{e,c})}$. We can assume with good approximation that the emission from a single particle is almost monochromatic at the frequency $\nu_m \sim \nu_c/3$, where there is the maximum of the emission. So, equations 2.4 and 2.5 show that, for a given magnetic field B, increasing the electron energy also increases the emitted power, and the critical frequency shifts to higher frequencies. Electrons with $\gamma \sim 10^4$ in magnetic fields that are typical for clusters ($B \sim \mu G$), radiate at radio frequencies ($\nu \sim 400$ MHz from eq. 2.5).

In astrophysical situations we always deal with an ensemble of electrons. If we assume that there are no collective processes, and no absorption phenomena, the total emission is given by

summing up the contribution of the single particles, and it will be dominated by their energy distribution and not by the shape of the spectrum of the single electron. In the simplest case we can assume that the energy distribution of the electrons is described by a power law[5] in an energy range $E_{min} - E_{max}$:

$$f(E) \propto E^{-\beta_{inj}}, \tag{2.6}$$

or

$$g(p) \propto p^{-\delta_{inj}} \tag{2.7}$$

between $p_{min} - p_{max}$ in the momentum space.
The synchrotron emission from this ensemble of relativistic electrons is also well described by a power law:

$$S(\nu) \propto \nu^{-\alpha_{inj}}, \tag{2.8}$$

where the exponent α_{inj}, called *spectral index*, depends only on the exponent of the electrons distribution[6]:

$$\alpha_{inj} = \frac{\beta_{inj} - 1}{2} = \frac{\delta_{inj} - 3}{2}. \tag{2.9}$$

If E_{max} ($\Rightarrow \gamma_{max}$) is the maximum energy of the electrons distribution, we can define a critical frequency as in eq. 2.5 for the total spectrum:

$$\nu_c \simeq 0.4 \left(\frac{\gamma_{max}}{10^4}\right)^2 \left(\frac{B_\perp}{\mu G}\right) \text{GHz}. \tag{2.10}$$

Below this frequency the spectrum is a power law with spectral index α_{inj}, while above this frequency it has the exponential cut-off $S(\nu) \propto e^{-\nu/\nu_c}$, which reflects the cutoff in the spectra of the highest-energy electrons in the distribution.

Aging of synchrotron spectra

The situation described above refers to kind of a snapshot of the situation at the beginning of the emission process, right after the particles have been produced or accelerated by some mechanism. There are different processes, the first being the production of the synchrotron radiation itself, that reduce the energy of the emitting particles. Another process relevant in the astrophysical situation we are considering in this thesis is the the Inverse-Compton (IC) scattering off photons such as those of the CMB. These energy loss processes will alter the shape of the synchrotron spectrum (*spectral aging*). The higher the energy of the emitting

[5] A power-law shape of the energy spectrum doesn't have a real justification a priori, but it is the spectrum observed for cosmic rays, and moreover some mechanism presumed for the acceleration of relativistic particles, like the first-order Fermi mechanism, naturally produce an energy spectrum that is a power law.

[6] Some authors define the spectral index as $\alpha' = -\frac{\beta inj - 1}{2} = \frac{1-\beta_{inj}}{2}$ in a way that the radiation spectrum will be $S(\nu) \propto \nu^{\alpha'_{inj}}$.

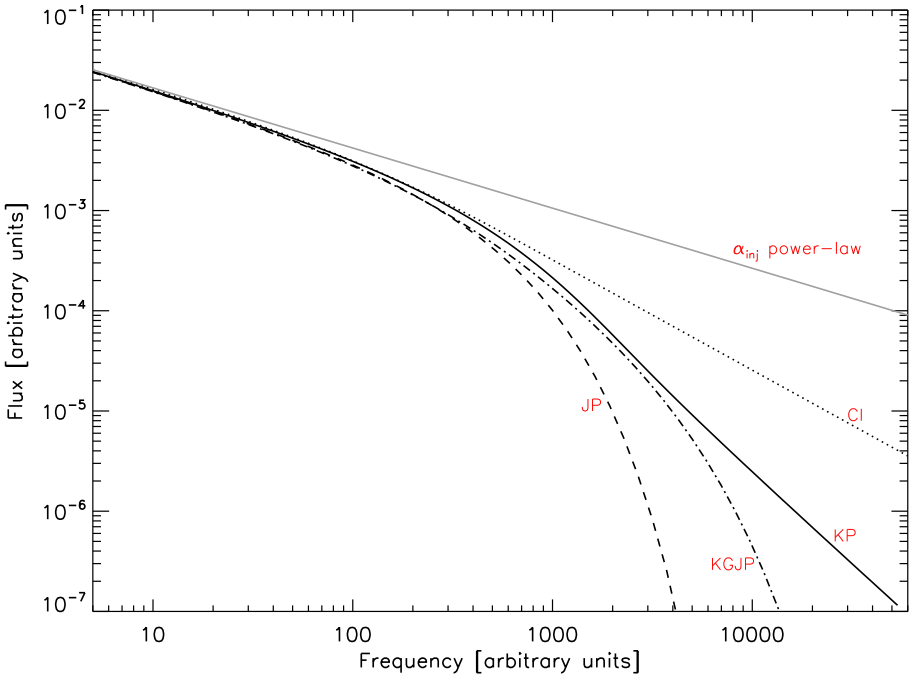

Fig. 2.6: Overview of different spectral aging models. All spectral models have the same injection spectral index. Solid gray line: power-law spectrum without any aging; solid black line: KP model; dotted line: CI model; dash-dotted line: KGJP model; dashed line: JP model. Adopted from van Weeren et al. (2012a).

electrons, the more they will radiate (eq. 2.4), and thus the faster they will lose their energy. This processes will therefore affect first the high frequency end of the spectrum, producing a steepening, departing from the initial injection power-law. At low frequencies the spectrum remains the injected power law (Rybicki & Lightman, 1979). As time pass by, the break frequency ν_{br} at which the departure from the injected power-law happens, shifts to lower frequencies. The quantity ν_{br} can therefore be used to estimate the age of the radio source. The particles energy distribution (and consequently the radiation frequency spectrum) can undergo modification with time also due to leakage of particles or injection of new ones. The shape of the high-frequency fall-off is determined by the micro-physics of the processes at play, such as the energy injections to the electrons and the pitch angle w.r.t. the magnetic field.

Spectral breaks from α_{inj} to $\alpha_{CI} = \alpha_{inj} + 0.5$ are predicted by the theory of synchrotron sources for the case of a continuous supply, according to the same injection power-law, of fresh relativistic electrons in the emitting region and synchrotron losses (the continuous injection (CI) model; see Fig. 2.6; Kardashev, 1962).
The evolution of synchrotron sources due to synchrotron losses strongly depends on the efficiency of pitch-angle isotropization of the relativistic electrons due to interaction with micro-turbulence in the plasma. For the Kardashev-Pacholczyk (KP) model the isotropization is negligible, and the pitch angle of the electrons remains in its original orientation with respect to the magnetic field. In this case, synchrotron losses lead to a power-law fall-off at high frequencies with index $\alpha_{KP} = 4/3\alpha_{inj} + 1$ (the Kardashev-Pacholczyk (KP) model; see Fig. 2.6;

Kardashev, 1962; Pacholczyk, 1970). On the contrary, if the isotropisation is so fast[7] that the electron distribution remains almost absolutely isotropic, the energy losses are more efficient, and an exponential cut-off instead of the power-law region appears. This case was considered by Jaffe & Perola (1973, the Jaffe-Perola (JP) model; see Fig. 2.6). The JP model is more realistic from a physical point of view, as an anisotropic pitch angle distribution will become more isotropic due to changes in the magnetic field strength between different regions and scattering and irregularities of $\vec{B}$ created by Alfvén waves (e.g. Carilli et al., 1991; Tribble, 1993; Slee et al., 2001).
Both the KP and the JP models assume that the particles are injected with a single impulsive injection, and then they simply age. Komissarov & Gubanov (1994) extended the JP model to include a finite period of freshly supplied electrons and electron losses due to synchrotron and IC scattering (KGJP model; see Fig. 2.6).

2.3.2 Models for radio relics

Relics are found in both merging and cool-core clusters, suggesting that they may be related to minor or off-axis mergers, as well as to major mergers. Indeed, the most widely accepted scenario to explain giant radio relics invokes particle acceleration in shocks produced during merger events. This is consistent with their elongated structure, often almost perpendicular to the merger axis. Smaller relic structures may moreover be produced via adiabatic compression of fossil plasma.

Production of emitting electrons by SHOCK ACCELERATION

To date the most widely accepted scenario to explain *giant radio relics* invokes diffusive particle acceleration through shocks that develop during cluster mergers (DSA; Krymskii, 1977; Drury, 1983; Blandford & Eichler, 1987). Indeed, DSA is widely accepted as the primary mechanism through which relativistic particles are produced in a variety of astrophysical environments such as the solar wind colliding with planetary magnetospheres, or shocks surrounding supernova remnants. Moreover, cosmological simulations suggest that such shocks are quite common in the ICM (e.g. Vazza et al., 2009a,b) and that they are indeed collisionless features able to accelerate particles passing through them (e.g. Blasi, 2000; Miniati et al., 2001b; Fujita & Sarazin, 2001). Scattering processes increase the probabilities that a particle that has just been accelerated passing through the shock will diffuse back through the front to where it came from and get accelerated again. With this process, when particles pass back and forth through the shock, high energies can eventually be achieved. Cosmological hydrodynamic simulations show that shocks expected to form in the ICM at cluster outskirts as a consequence of mergers of subclumps or accretion of matter are relatively weak, with Mach numbers $M \sim$ a few (e.g. Ryu et al., 2003; Kang et al., 2007; Hoeft et al., 2008; Vazza et al., 2009a). On the other hand, shocks with Mach numbers of order $\sim$ 3-4 are enough to explain the non-thernal radiation observed in the radio regime (Gabici & Blasi, 2003). It has been shown by Kang & Ryu (2011) that DSA of electrons directly from the thermal pool at such

[7] On time scales much shorter than the time after which the radio emission diminishes significantly (10 - 100 Myr).

weak shocks is rather inefficient. They suggested that the presence in the relic site of pre-accelerated CRs electrons produced during previous shocks and/or by turbulent acceleration would alleviate the problem of inefficient injection in weak cosmological shocks.

DSA is a Fermi-I mechanism for particle acceleration (Fermi, 1949). In this process, both electrons and protons in the ICM get accelerated at the shock surface during mergers, but the dynamics of the two components are extremely different because of the differences in the energy loss processes (see e.g. Gabici & Blasi, 2003; Kang, 2011). Indeed, eq. 2.4 shows that the synchrotron power emitted by a particle is inversely proportional to the fourth power of the particle mass. Therefore, protons lose only a small fraction of their energy during the cluster lifetime, and they are stored in clusters for cosmological times. On the other hand, high energy electrons have a radiative lifetime much shorter than the age of the cluster. During the diffusive acceleration process particles reach increasing energy with time and their distribution drops off exponentially above the maximum energy reached $E_{max}(t)$. Below $E_{max}(t)$, the particles are accelerated according to a power-law energy distribution, whose spectral index is determined by the properties of the shock. At the beginning of the process, i.e. at low energy, electrons and protons are accelerated in the same way and have the same distribution because also for low-energy electrons the radiative losses are negligible with respect the acceleration process. For protons, as far as the acceleration mechanism is at work efficiently, the maximum energy $E_{p,max}(t)$ reached continues to increase with time and it depends on the shock age. For electrons, the maximum energy injected increases with time till when the increasing synchrotron/IC losses equal the energy gains by DSA. When this equilibrium between energy gains and losses is reached, the maximum electron energy $E_{e,max}$ injected approaches an asymptotic value $E_{e,eq}$ that is determined by the properties of the shock and does not depend on the shock age. The time t_{eq} required for the electrons to reach the equilibrium injection spectrum is relatively short. At this point, if the properties of the shock remain unchanged (stationary conditions) the injection spectrum (at the position of the shock) becomes steady and cuts off at E_{eq}. In the *test-particle regime*[8] of DSA theory the integrated injection spectrum of electrons below $E_{e,eq}$ is a power law $f(p) \propto p^{-\delta_{inj}}$, where δ_{inj} is determined by the properties of the shock. When the particle diffusion is specified, the properties of the shock such as the compression ratio C and the Mach number M are the primary parameters that determine the efficiency of DSA and the energy distribution of the particles, and hence of the integrated synchrotron spectrum. According to theory, particles are Fermi accelerated at the shock front to a power-law distribution function in relativistic momentum p of logarithmic slope δ_{inj} (from Blandford & Eichler, 1987):

$$g(p) \propto p^{-\delta_{inj}} \qquad \text{with} \qquad \delta_{inj} = \frac{3C}{C-1}. \tag{2.11}$$

If the plasma is a perfect gas, we can apply the canonical shock jump condition (Rankine-Hugoniot conditions) in the form (from Blandford & Eichler, 1987):

$$\frac{1}{C} = \frac{\gamma_H - 1}{\gamma_H + 1} + \frac{2}{(\gamma_H + 1)M^2}. \tag{2.12}$$

[8] When the dynamical feedback of the Cosmic Rays electrons pressure is ignored.

Combining eqs. 2.11 and 2.12, assuming a heat ratio of $\gamma_H = 5/3$, we obtain the particle index as a function of the shock Mach number:

$$\delta_{inj} = \frac{4M^2}{M^2 - 1}. \tag{2.13}$$

The synchrotron radiation spectrum produced by this underlying population of electrons will have spectral index (from eq. 2.9):

$$\alpha_{inj} = \frac{3}{2(C-1)} = -\frac{1}{2} + \frac{M^2 + 1}{M^2 - 1}. \tag{2.14}$$

After the electrons are injected at the shock location according to the equilibrium distribution, they are naturally subject to energy losses while being advected downstream in the postshock regions. From theory it is well known that the most energetic particles lose their energy faster than the less energetic ones and become rapidly invisible behind the shock front. The lower energy electrons instead advect further from the shock before cooling. Thus, moving across the source away from the shock, the electron radiative age increases and the cut-off energy in the local electron spectrum due to the radiative cooling decreases linearly with distance from the shock location. At the farthest point downstream, the cutoff energy will be at $E_{e,br}$, which depends on the shock age and moves to lower frequencies with time. A gradient in the spectral index across an edge-on relic is then expected (see Fig. 2.7).

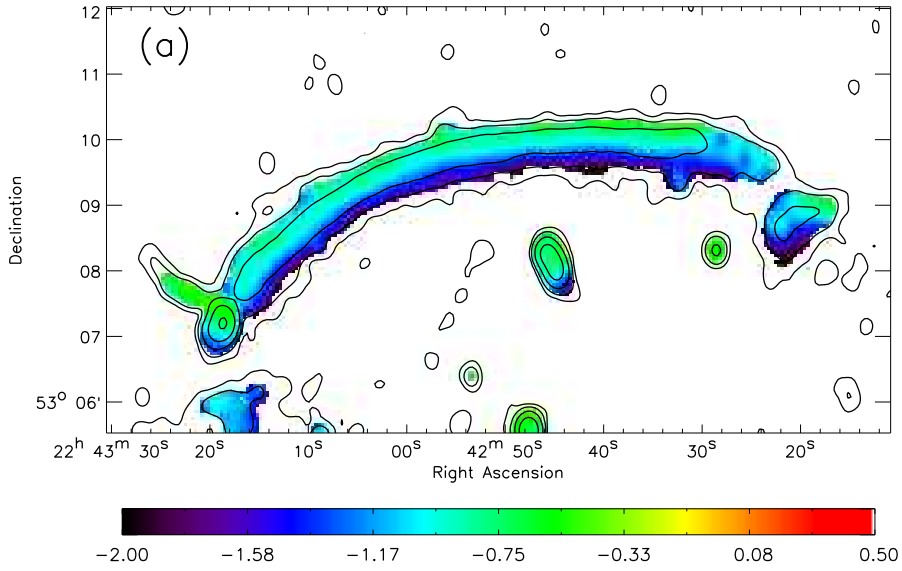

Fig. 2.7: The radio relic in CIZAJ2242.8+5301: contours represent the total intensity emission obtained with the GMRT at 610 MHz. Colors represent spectral index values obtained with a power-law fit to measurements between 0.61 and 2.3 GHz. Adopted from van Weeren et al. (2010).

Therefore, there are two characteristics energies in the distribution of the electrons: $E_{e,eq}$, which reflects the strength of the acceleration mechanism (shock) and does not depend on the shock age, and $E_{e,br}$, which more properly describes the electron aging and can be used to estimate the shock age. These two values translate into as many characteristic frequencies in

the integrated synchrotron spectrum, viz. ν_{eq} and ν_{br}.
Assuming that the shock is continuously accelerating particles according to the same injection power-law for a time exceeding the electrons cooling time (CI model, Sect. 2.3.1; Kardashev, 1962), summing the contribution of the particles freshly injected at the shock location and the contribution from the particles which age as they move away from the shock, we expect a volume integrated spectrum that is a *single power-law* with spectral index $\alpha_{obs} = \alpha_{inj} + 0.5$ (see Fig. 2.9b). However, strictly speaking, the stationarity for the spectrum can be reached only if the time for energy losses is shorter than the age of the shock at all energies. In other words, electrons with injection energy below $E_{e,br}$ didn't have enough time to lose their energy and the injection spectrum is expected. If we assume that the shock started to accelerate recently, we would be able to catch the break frequency still in the observable frequency range, if the spectrum is known over a wide frequency range. Kang (2011) shows that the simulated downstream integrated electron spectrum at a quasi-parallel shock[9] is a broken power-law which steepens from $E^{-\delta_{inj}}$ to $E^{-(\delta_{inj}+1)}$ above $E > E_{br}(t)$, with an exponential cutoff at energies higher than E_{eq}. As a consequence the volume integrated synchrotron spectrum has also three regimes:

$$S(\nu) \propto \begin{cases} \nu^{-\alpha_{inj}} & \text{at } \nu < \nu_{br}(t) \\ \nu^{-(\alpha_{inj}+0.5)} & \text{at } \nu_{br}(t) < \nu < \nu_{eq} \\ exp(-\nu/\nu_{eq}) & \text{at } \nu > \nu_{eq}. \end{cases}$$

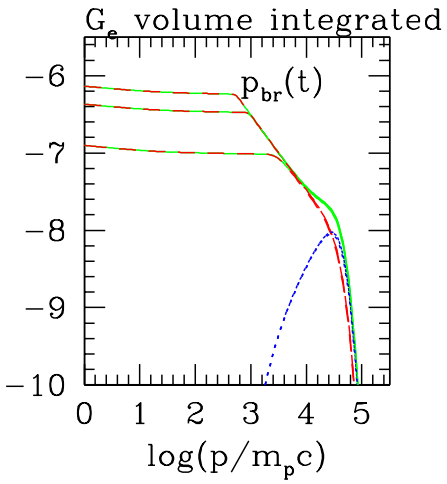

Fig. 2.8: Results from DSA simulations in the test-particle case. Shown is the downstream integrated electron spectrum, $G_{e,2} = \int_{-\infty}^{0} f_e(p)p^4dx$ (red dashed line), the upstream integrated electron spectrum $G_{e,1} = \int_{-\infty}^{0} f_e(p)p^4dx$ (blue dotted line) and the sum of the two curves (green solid line) for different times (t/t_0=1,3,5). Adopted from Kang (2011).

[9]When the angle between the magnetic field upstream of the shock and the shock normal is less than 45 degrees.

Appendix A summarizes the relations existing between the spectral index of the synchrotron spectrum, the spectral shapes of the particle distribution in energy and momentum space and the shock properties.

Production of emitting electrons by ADIABATIC COMPRESSION

As introduced, smaller radio relics can be produced by adiabatic compression triggered by shock and re-energization of relic plasma left behind by radio galaxies (Enßlin & Gopal-Krishna, 2001; Enßlin & Brüggen, 2002). Three-dimensional magneto-hydrodynamical (MHD) simulations of the passage of a radio plasma cocoon filled with turbulent magnetic fields through a shock wave have shown that the properties observed in some relics can be reproduced (Enßlin & Brüggen, 2002; Slee et al., 2001). If the magnetic field inside the cocoon is not too strong, on contact with the shock wave the initially spherical radio cocoon is first compressed and finally torn into a filamentary structure. In these simulations where the magnetic fields are dynamically important a more complicated morphology is produced. The degree of polarization produced is relatively high, and the electric polarization vectors tend to be perpendicular to the radio filaments, indicating aligned magnetic field structures within them.
In this case, we expect steeper and curved integrated spectra, due to the already aged population of electrons that are re-accelerated. In fact, the adiabatic compression would just shift the already aged spectrum at high energies upward without modifying the spectral slope. A steepening is indeed observed in the integrated synchrotron spectrum of some relics (see e.g. Fig. 2.9d and Table 4 in Feretti et al. (2012)).

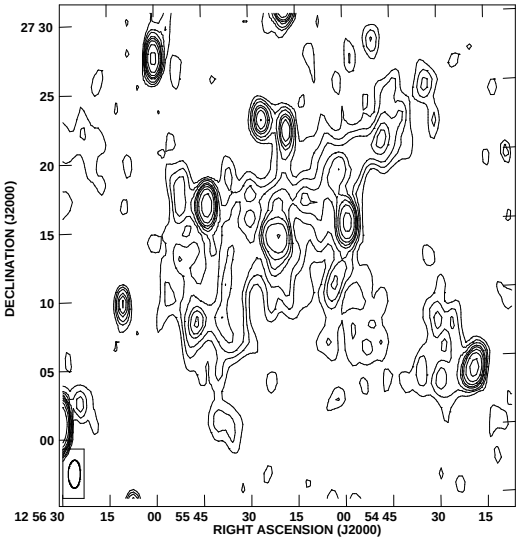

(a) The radio gischt in the Coma cluster at 327 MHz. Adopted from Giovannini et al. (1991).

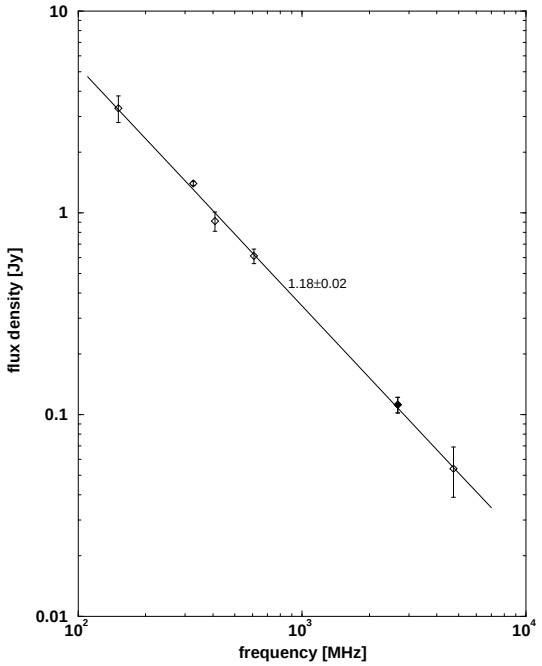

(b) The straight integrated radio spectrum of the Coma relic. Adopted from Thierbach et al. (2003).

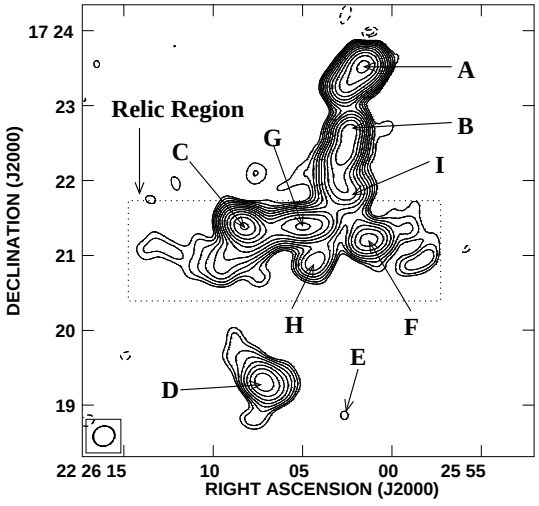

(c) The radio phoenix in the cluster A2443 at 325 MHz. Adopted from Cohen & Clarke (2011).

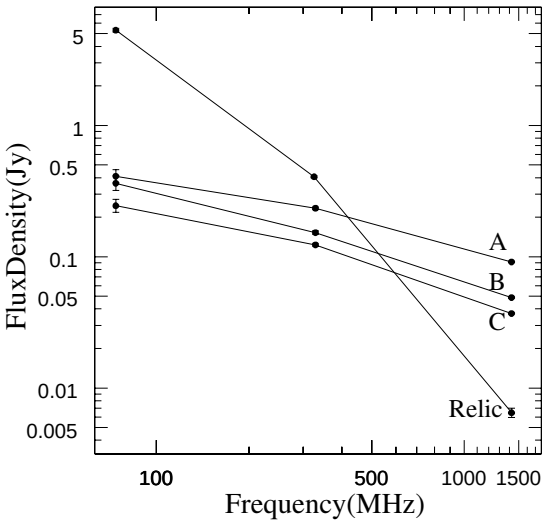

(d) The curved integrated radio spectrum of the A2443 relic. Adopted from Cohen & Clarke (2011).

Fig. 2.9: Radio gischt vs radio phoenices.

2.3.3 Models for radio halos

Production of emitting electrons by TURBULENT ACCELERATION

The observed properties of radio halos support a re-acceleration scenario by *turbulence* induced during clusters mergers. Mergers are among the most energetic events that take place in the universe. The bulk of this energy is dissipated through shocks, which produce radio relics (e.g. Vazza et al., 2009a, 2012). Additionally vortical motions, shear flows and instabilities efficiently drive turbulence in the ICM during these events (Subramanian 2006). This turbulence amplifies magnetic fields to μG values and may efficiently re-accelerate particles in radiohalos (e.g. Jaffe, 1977; Brunetti et al., 2001; Petrosian, 2001; Schlickeiser et al., 1987). In this scenario, as soon as large scale turbulence in the ICM reaches smaller resonant scales (via cascading or induced plasma instabilities, e.g. Brunetti et al., 2004; Lazarian & Beresnyak, 2006; Brunetti & Lazarian, 2007) , particles are accelerated and generate synchrotron emission. The acceleration of particles by turbulence is due to the resonant scattering of these particles by turbulent waves, which lead to a stochastic energization of the former and to the damping of the latter (Melrose D.b. plasma astrophysics). Different coupling between particles and waves may result in energy transfer: magnetosonic (MS) waves (considered e.g. in Cassano & Brunetti, 2005), magnetic Landau damping (e.g. Kulsrud & Ferrari, 1971; Schlickeiser & Miller, 1998), lower hybrid (LH) waves (e.g. Eilek & Weatherall, 1999), fast compressive turbulent modes (an MHD version of sound waves)(e.g. Brunetti & Lazarian, 2007) and Alfvén waves (e.g. Brunetti et al., 2004; Brunetti & Blasi, 2005) are examples that have been investigated in literature. We point to these papers for detailed description of the mechanism.
The acceleration should take place on a time-scale of the order of a cluster-subcluster crossing time ($\sim$ 1 Gyr), during which turbulence is continuously injected on scales of the order of the subcluster size, transported at smaller scales and then dissipated into heating of the intergalactic medium and acceleration of relativistic particles over a fairly large volume. This argument is supported by the observation of a bimodality.
The particle spectrum is determined by the interplay between cooling due to radiative losses (mainly synchrotron and IC), and acceleration due to turbulence. The usual power-law spectrum for the injection of relativistic electrons up to a maximum momentum p_{max} can be reasonably assumed. The maximum energy to which particles can be accelerated pinpoints the energy at which the timescale of the electron radiative losses becomes equal to that of the turbulent acceleration. Indeed, stochastic particle acceleration by MHD turbulence is a second-order Fermi (Fermi-II) process (Fermi 1949), and is a rather inefficient process that can accelerate electrons up to energies of a few GeV. At higher energies radiative losses of the relativistic electrons (synchrotron and Inverse Compton) become more efficient than the acceleration mechanisms, causing a steepening of the integrated radio spectrum .This is consistent with the observed spectra in well studied halos (Thierbach et al., 2003; Dallacasa et al., 2009).
Moreover, the cooling time of the emitting electrons is smaller than, or comparable to, the cascading time-scale of the large-scale turbulence, implying that the evolution of the synchrotron power depends very much on the level of MHD turbulence in the ICM (Cassano & Brunetti, 2005; Brunetti & Lazarian, 2007). Consequently, if we simply assume that the injection of MHD turbulence is suppressed "instantaneously" at a given time (e.g. at late merging-phase), then also the synchrotron emission at higher radio frequencies is suppressed, falling below

the detection limit of radio observations, as soon as the energy density of turbulence starts decreasing.

According to this scenario the formation and evolution of radio halos is, therefore, tightly connected with the dynamics and evolution of the hosting clusters. The occurrence of radio halos at any redshift depends on the rate of cluster-cluster mergers and on the fraction of the merger energy channeled into MHD turbulence and re-acceleration of high-energy particles.

Cassano & Brunetti (2005)developed statistical models based on a self-consistent approach, which at the same time model the evolution of the thermal properties of the intra-cluster medium of the galaxy clusters and the generation and evolution of the non-thermal phenomena. This statistical model represents the ”cosmological“ extension of the turbulence acceleration models developed by Brunetti et al. (e.g. 2001). These allowed them to produce a synthetic population of halos with specific break frequency as function of the mass of clusters hosting them.

They showed that in this scenario, the fraction of clusters with a giant radio halo in a fixed redshift range increase with increasing mass of the hosting cluster. This is mostly due to the fact that mergers in smaller clusters are not able to efficiently generate turbulence in volumes of order of Mpc^3. Moreover, the model predicts that increasing the mass of the hosting cluster increases also the fraction of them hosting a radio halo with smaller values of the spectral index, i.e. with flatter radio spectra (see Fig. 2.11), in agreement with observational evidence for a trend between the radio spectral index of radio halos and the temperature of the clusters (Feretti et al., 2004; Giovannini et al., 2009). Clusters with higher temperature (and hence with higher masses) tend to possess halos with a flatter spectrum. This may be naturally understood in the framework of the re-acceleration model, since the hottest clusters are more massive and may have undergone more recent and violent mergers, able to re-accelerate particles to higher energies, producing halos with flatter radio spectra.

Production of emitting electrons by P-P COLLISIONS

Alternatively, electrons emitting in radio halos can be produced by inelastic proton-proton collisions (*secondary model*). The secondary model was initially proposed by Dennison (1980) and subsequently developed by Blasi & Colafrancesco (1999). Recently, these models have been considered by many authors in the framework of numerical simulations, where they can be easily implemented (Dolag & Enßlin, 2000; Miniati et al., 2001a; Pfrommer et al., 2008; Donnert et al., 2010).
As already discussed, relativistic protons produced in the ICM during the cluster lifetime stay confined and pile up because of the low energy losses. This confinement increases the probabilities to have inelastic p-p collisions between these relativistic protons and the thermal protons in the ICM. This process would provide a continuous production of charged pions $\pi^{\pm}$ and neutral pions π^0, which in turn decay into secondary electrons and positrons and into γ-rays through the decay chain (Dermer, 1986):

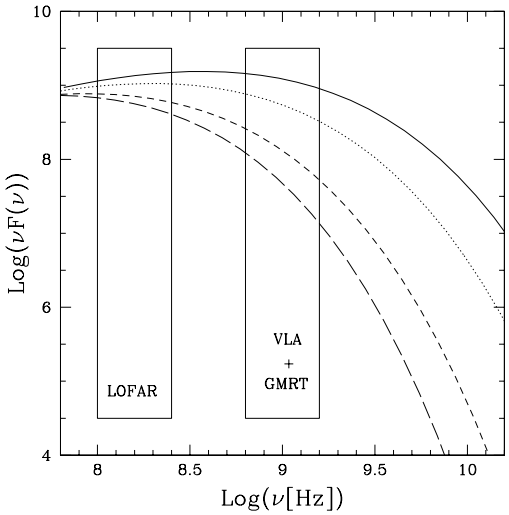

Fig. 2.10: Example of the emitted synchrotron power (arbitrary units) as a function of frequency, for different energy densities of turbulence (magnetosonic waves): 30% (solid line), 20% (dashed line), 15% (long-dashed line) of the thermal energy density. Frequency ranges of interest for GMRT, VLA and LOFAR are also marked. Adopted from Brunetti et al. (2009).

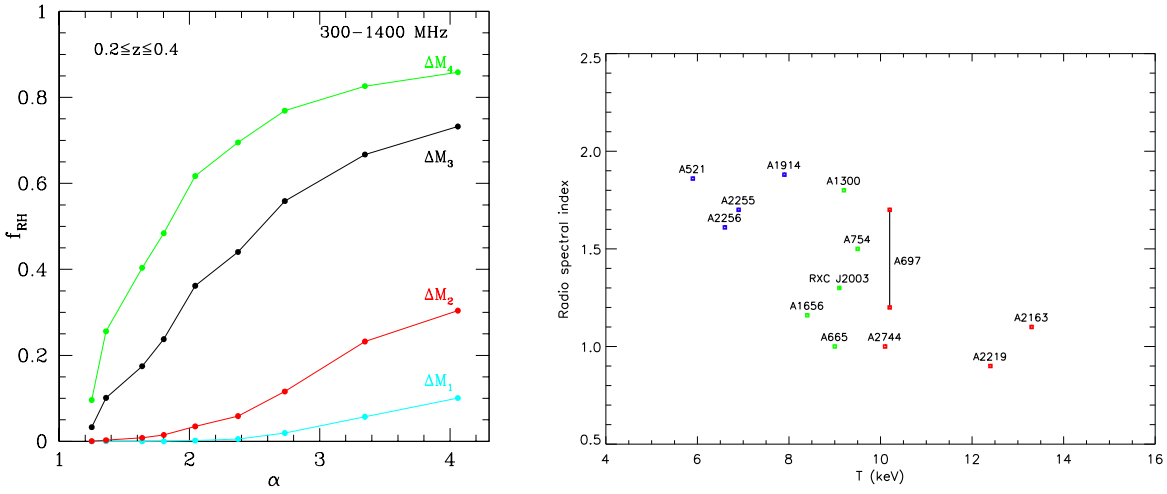

(a) (b)

Fig. 2.11: Left panel: Distribution of spectral index between 300 - 1400 MHz, calculated in the framework of the statistical re-acceleration model. The redshift range $0.2 \leq z \leq 0.4$ and four mass bins ($\Delta M_1 = 5-8\cdot10^{14}\mathrm{M}_\odot$; $\Delta M_2 = 8\cdot10^{14}-1.35\cdot10^{15}\mathrm{M}_\odot$; $\Delta M_3 = 1.35-2.5\cdot10^{15}\mathrm{M}_\odot$; $\Delta M_1 \geq 2.5\cdot10^{15}\mathrm{M}_\odot$) have been considered. Right panel: Radio halo spectral index vs temperature for clusters in literature. Adopted from Trasatti (2010).

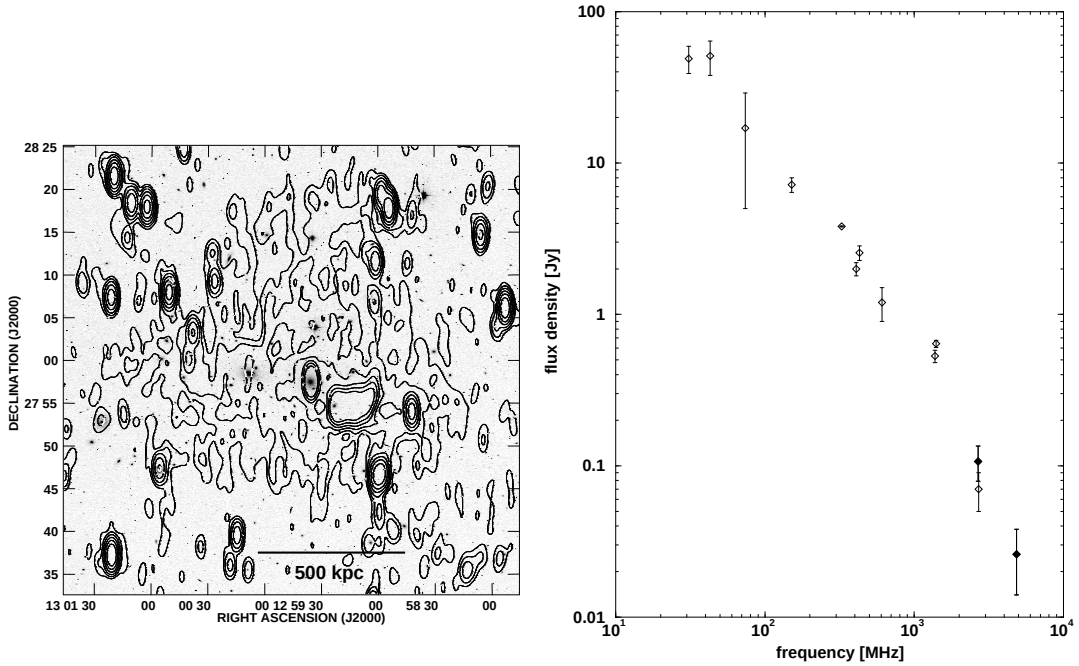

(a) Total intensity radio emission at 300 MHz superimposed onto the optical image from the Digitized Sky Survey. Adopted from Feretti et al. (2012).

(b) Integrated radio spectrum. Adopted from Thierbach et al. (2003).

Fig. 2.12: The Coma radio halo from literature.

$$\begin{cases} p_{CR} + p_{ICM} \rightarrow \pi^0 + \pi^+ + \pi^- + ... \\ \pi^0 \rightarrow 2\gamma \\ \pi^{\pm} \rightarrow \mu + \nu_{\mu} \\ \mu^{\pm} \rightarrow e^{\pm} + \nu_{\mu} + \nu e. \end{cases}$$

As a consequence, the injection of CR electrons is constrained by the distribution function of the CR protons, which should retain the injection power-law, since due to the inefficient energy losses their spectrum should be only slightly modified during the cluster life-time (Blasi & Colafrancesco, 1999). It is expected that the protons in clusters get accelerated to > 1 TeV, and therefore that the spectra of the relativistic electrons have maximum energies ≥ 100 GeV. The spectra should therefore be single power-laws in the accessible range of radio frequencies, without a break, in contrast to the observations that revealed a steepening in the spectra of some well studied radio halos (Thierbach et al., 2003; Dallacasa et al., 2009). Moreover, with this model radio halos would be expected to be more frequently observed in clusters and the observed bimodal behavior is not expected. Finally, one of the predictions of this model is that clusters must be observed in gamma rays (decay). However, so far no cluster has been observed in this regime (see Sec. 1.2.5)

2.4 Importance of high frequency observations

A significant increase of the statistics of non-thermal radio emission from galaxy clusters is expected with the advent of the new generation low-frequency ($\sim$ 10 - 200 MHz) radio telescopes such as LOFAR and SKA, whose high sensitivity and low-frequency capabilities are well suited to probe the diffuse steep-spectrum radio emission in clusters. For example, Cassano et al. (2010) predict that the *Tier 1* LOFAR survey will discover about 350 giant radio halos at redshifts ≤ 0.6, half of these halos are expected to have a synchrotron spectral index $\alpha > 1.9$ between 250-600 MHz, and would brighten only at low frequencies.
This can be related to the fact that major mergers able to produce brighter diffuse sources are rare events, while minor mergers are expected to be more common. According to these predictions, the currently known radio relics and halos are the most extreme and energetic cases, for which high-frequency observations (at GHz frequency) are necessary to constrain the shape of the spectra in order to test the models expectations. To date, the integrated spectra are obtained in few cases only with more than three flux density measurements at different frequencies; for most sources the highest available frequency is 1.4 GHz (Feretti et al., 2012). Therefore, while the new generation of low-frequencies radio telescopes would become fully operational, observations at GHz frequencies of the currently known radio relics and halos are essential to test the model expectations and shed light on the origin of these diffuse sources.

Chapter 3

The Coma radio relic from combination of interferometric and single-dish data*

3.1 Introduction

As introduced in Chap. 2, detailed studies of the spectral characteristics of radio relics, together with studies of their morphological and polarization properties, allow to test the current models, and study the shock properties in case of diffusive shock acceleration (DSA). However, the accurate measurement of the integrated spectra of radio relics is a difficult task because these sources are extended with a low surface brightness and they usually embed a number of discrete sources, whose flux density needs to be carefully subtracted from the total diffuse emission. Moreover, their commonly steep spectra, make more difficult the study at high frequencies, where important constraints on the underlying physical mechanism can be found. Indeed, integrated spectra over a wide range of frequencies are available in literature only for few of this objects (see Feretti et al., 2012). The task requires high-resolution imaging at many frequencies with radio interferometers. However, increasing the observing frequencies, the interferometers' field of view decreases and they encounter the technical problem of the *missing short spacings*, that makes them "blind" to very extended structures. On the other hand, single dishes are optimal to catch all the emission from a field but they lack angular resolution. Combining single dish with interferometric data allows to get final maps with both the high resolution of the interferometer data and the short-spacing information provided by the single-dish observations. This procedure is very powerful to investigate the emission of extended radio sources at cm-wavelengths. The problem of small field of view is easily overcome performing the interferometric observations in mosaic mode.
We applied this technique for the first time to study in detail the properties at cm wavelength of the radio relic emission in the Coma cluster. In this chapter we discuss the theory of interferometric (Sect. 3.1.1) and single-dish (Sect. 3.1.2) observations and their combination (Sect. 3.1.3). In Sect. 3.2 we present the science case of the Coma radio relic. We present new radio observations of the Coma radio relic in the L-band (Sect. 3.3.1) and in the S-band (Sect. 3.3.2). In Sects. 3.4 and 3.5 we present the data combination in the L and S band respectively. In Sect. 3.6 we discuss the relic extent from our observations. The integrated radio spectrum of the radio relic is presented in Sec. 3.7. Sec. 3.8 describes the results from Planck SZ observations at the relic position. Conclusions are presented in Sect. 3.9.
We adopted the cosmological parameters H_0 =71 km s^{-1} Mpc^{-1}, Ω_Λ=0.73 and Ω_m=0.27

*Trasatti, Klein, Bonafede (in prep.)

(Bennett et al., 2003), which provide a linear scale of 0.44 kpc arcsec^{-1} at the redshift of the Coma cluster.

3.1.1 Theory of interferometric observations

Detailed lectures on interferometry and synthesis imaging in radio astronomy include e.g. Thompson et al. (2002), Perley et al. (1990) and Taylor et al. (2000).

Aperture synthesis or *synthesis imaging* techniques, first developed at radio wavelengths in the Fifties, helps to overcome the resolution problem suffered by single-dish observations. A basic inverse relation exists, in fact, between the angular resolution of a single antenna and its diameter. For example, to reach a modest resolution of $\sim 1'$ at the typical radio frequency of 1.4 GHz (=21 cm), an impossibly large single antenna of ~880 m would be required! The two largest fully steerable single-dish radio telescopes are the *Effelsberg-100m Telescope*[1] and the *Green Bank Telescope*[2], with surface areas of 100m×100m and 100m×110m respectively. At 21 cm Effelsberg observations have an angular resolution of $\sim 10'$ (see Sec.3.3.1).

There are two fundamental ideas behind radio interferometry:

- the resolution of a big antenna aperture can be "simulated" with two (or more) smaller dishes placed at a distance equivalent to the aperture one want to simulate (an interferometer). For example, observing at a wavelength of 21 cm, a resolution of $\sim 1'$ can be achieved with an interferometer of small antennas placed at a distance of ~ 880 m from each other.

- A Fourier transform relation exists between the sky radio brightness distribution I and the response of a radio interferometer. The correlation of the source signals received (the voltage outputs) by a pair of antennas constituting the interferometer, is a complex quantity called *visibility*, the magnitude of which has the dimensions of spectral power flux density (W·m^{-2} ·Hz^{-1}). The visibility V is the Fourier (anti-)transform of the sampled true source brightness distribution I.

However, a pair of antennas with given separation d (called *baseline*), observing at a given wavelength λ, measures (samples) instantaneously only one specific Fourier component of the source signal, i.e. the visibility corresponding to a given *spatial frequency u* measured in wavelengths:

$$u(\lambda) = \frac{d_p}{\lambda} \tag{3.1}$$

where d_p is the projected baseline, as seen by the source. This means that a pair of antennas samples instantaneously only one component of the true source brightness distribution, that

[1]The Effelsberg-100m Telescope is operated by the Max-Planck-Institut für Radioastronomie (MPIfR) In Bonn, Germany. `http://www.mpifr-bonn.mpg.de/effelsberg`.

[2]The National Radio Astronomy Observatory is a facility of the National Science Foundation operated under cooperative agreement by Associated Universities, Inc. `https://science.nrao.edu/facilities/gbt`

produced by structures in the source with *physical spatial scale*:

$$x(rad) = \frac{\lambda}{d_p} = \frac{1}{u(\lambda)} \tag{3.2}$$

Note that *a pair of antennas placed at a small distance (i.e. small baseline, i.e. small spatial frequency) is sensitive to large structures in the source, while antennas with big separation (i.e. big baseline, i.e. big spatial frequency) are sensitive to small structures in the source.*
Improving the instantaneous source response of an interferometer requires the sampling of more Fourier components of the source's brightness distribution, that is more baselines, i.e. more antennas. Having N antennas means that N(N-1)/2 baselines are possible, i.e. N(N-1)/2 Fourier components of the source brightness distribution, i.e. N(N-1)/2 simultaneous samples of the source signal. Moreover, the earth's rotation can be used to vary the projected baseline coverage of an interferometer. The projected baseline vector has components (u,v,w). Coordinates u, υ and w are the projections of the terrestrial baseline onto a plane perpendicular to the source direction, in directions towards the East, the North and the phase tracking center, respectively. This can be reduced to a two-dimensional problem in the case of a linear array of antennas in an East-West line on the earth's surface, as it is in the case of the Westerbork Synthesis Radio Telescope (WSRT)[3] used for the observations presented in this Thesis. In this case the baselines are coplanar and we can set $w = 0$. The (u, υ) plane is called the *spatial frequency domain* or *Fourier domain*. The coverage of the (u, υ) plane describes the interferometer sampling function. Positions on the sky are defined in x and y, which are direction cosines measured with respect to the u and υ axes. The (x, y) plane is referred to as the *image domain*. A synthesized image in the (x, y) plane represents a projection of the celestial sphere onto a tangent plane at the source center. The Fourier and image planes are related by Fourier transform relations.
During a 12 hours observation, each projected baseline traces an ellipse in the (u,υ) plane. If the interferometer has more than two elements, and/or if the spacing of two elements is changed daily, the coverage of the (u,υ) plane will become a number of concentric ellipses having the same shape. The maximum value of u equals the maximum antenna separation in units of λ, and the maximum value of υ is smaller by the projection factor $\cos(\delta)$, where δ is the source declination. The *synthesis beam* (the Fourier transform of the interferometer sampling function) obtained by an east-west earth rotation aperture synthesis can therefore approach an elliptical Gaussian. The ellipticity will depends on the source declination, becoming almost circular for a source near the celestial pole. Figure 6.2 shows the different (u,υ) coverages resulting from the observations of two sources at different declinations, performed with identical observational set-up of the WSRT (the observations are presented in Sect. 3.3.2 and in Sect.. 4.3.1). Figure 3.2 shows the corresponding synthesis beams.

By virtue of its finite diameter D_{INT}, each element of the array is sensitive only to the radiation from a cone of width $A_{INT} \sim \lambda/D_{INT}$, which is called the *antenna primary beam*. The primary beam of the single antennas defines the interferometer field of view. Imaging to the edge of the primary beam adds noise to the outer parts of a field, because of the lower sen-

[3]The Westerbork Synthesis Radio Telescope is operated by the Netherlands Institute for Radio Astronomy ASTRON, with support from the Netherlands Foundation for Scientific Research (NWO). `http://www.astron.nl/radio-observatory/astronomers/wsrt-astronomers`

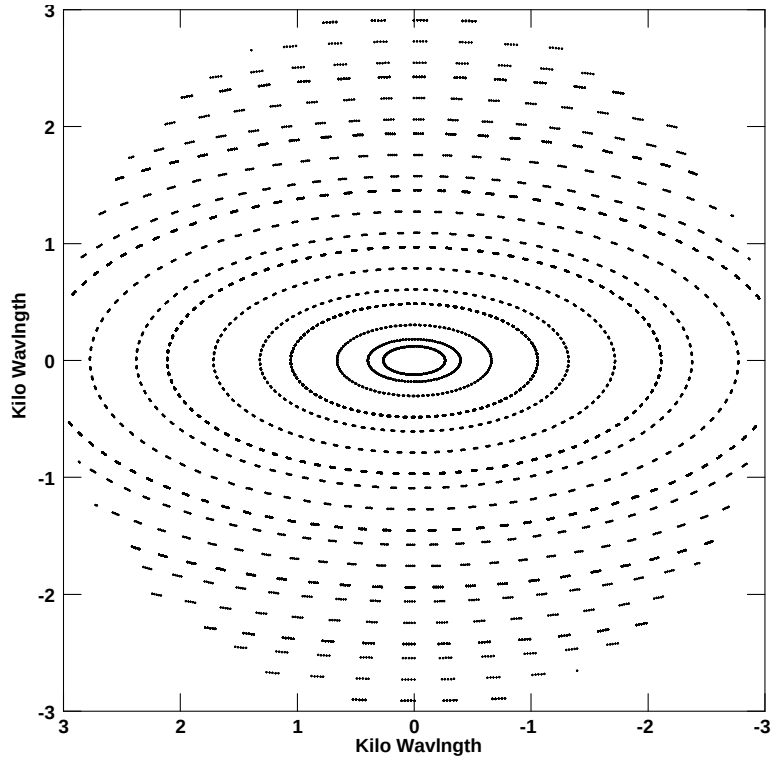

(a) Relative to the observations of the Coma relic at a declination of 27°.

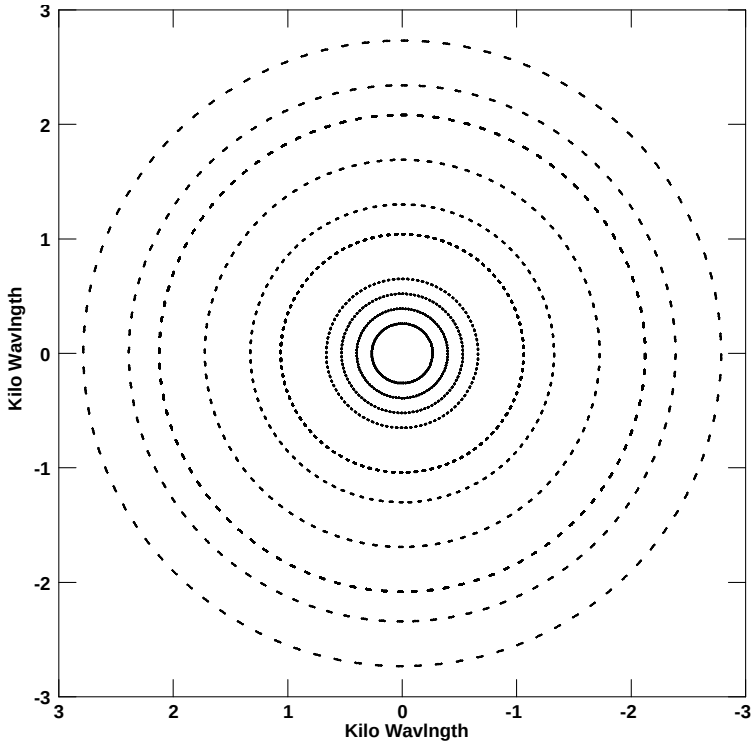

(b) Relative to the observations of the A2256 relic at a declination of 78°.

Fig. 3.1: Portion of the (u, v) coverages for the WSRT observations presented in Sects. 3.3.2 and 4.3.1 (upper and bottom panel respectively). The data shown refers to 1 (out of 64) channel of 1 (out of 8) frequency bands of 1 (out of 3) pointing. Only the range of spatial frequencies 0-3 kλ is shown (for both data sets the entire range extends up to 21 kλ).

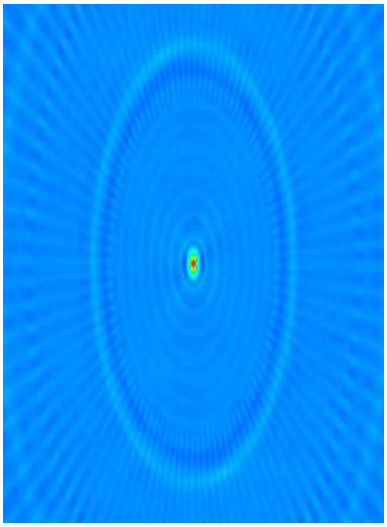

(a) Relative to the observations of the Coma relic at a declination of 27°.

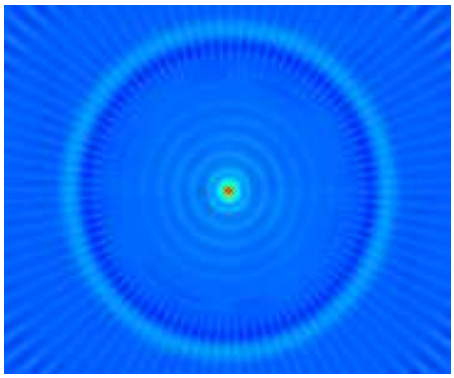

(b) Relative to the observations of the A2256 relic at a declination of 78°.

Fig. 3.2: Synthesis beams relative to the WSRT observations presented in Sects. 3.3.2 and 4.3.1 (left and right panel respectively).

sitivity there. Sources structures beyond the primary beam are completely lost. In case one wants to image a source larger than the primary beam, the observations must be carried out in *mosaic mode*, i.e. with more than one pointing centers (see Sec. 3.3.2).

IN THE FOURIER DOMAIN:
The visibilities $V'_{INT}(u, v)$ sampled by an interferometer can be expressed as:

$$V'_{INT}(u,v) = (V(u,v) * a_{INT}(u',v')) \times b_{INT}(u,v) + N \tag{3.3}$$

where:

- $V'_{INT}(u,v)$ are the sampled visibilities, i.e. the sampled Fourier components of the brightness distribution;
- $V(u,v)$ is the Fourier transform of the true brightness distribution, i.e. all the Fourier components contained in the source brightness distribution;
- $a_{INT}(u',v')$ is the Fourier transform of the *antenna primary beam*, i.e. the Fourier transform of the beam of the single antennas constituting the interferometer;
- $b_{INT}(u,v)$ is the interferometer sampling function, i.e. the Fourier transform of the *dirty synthesised beam*;
- N is a thermal noise term;

and the symbol $*$ denotes a convolution while $\times$ stands for a multiplication.

This means that *of all the Fourier components constituting the source signal falling in the interferometer's field of view (primary beam), the interferometer measures (samples) only those corresponding to the configuration of antennas used.*

IN THE IMAGE DOMAIN:
With enough sampling of the (u-υ) plane, the Fourier inversion of the sampled visibilities $V'_{INT}(u, v)$ (with interpolation of the missing information) provides the so-called *dirty image* I^D_{INT} of the source, i.e. the reconstructed source brightness distribution.

$$I^D_{INT}(x, y) = (I(x, y) \times A_{INT}(x', y')) * B^D_{INT}(x, y) + N \tag{3.4}$$

where:

- I^D_{INT} is the *dirty image*, i.e. the true brightness distribution modified by the interferometer response;
- $I(x, y)$ is the true brightness distribution;
- $A_{INT}(x', y')$ is the antenna primary beam;
- $B^D_{INT}(x, y)$ is the dirty synthesised beam;
- N is a thermal noise term;

and a convolution in the Fourier domain becomes a multiplication in the image domain and vice versa.

This means that *the reconstructed brightness distribution is the convolution of the source brightness distribution falling inside the field of view (primary beam) by the dirty synthesis beam, plus some thermal noise.*

The quality of the reconstructed image can be increased with the *clean* (or *deconvolution*) *process* (Högbom, 1974). In this process, the dirty image is deconvolved from the *dirty* synthesised beam and it is re-convolved with a *clean* synthesised beam $B^C_{INT}(x, y)$, providing the *clean image* of the source:

$$I^C_{INT}(x, y) = (I(x, y) \times A_{INT}(x', y')) * B^C_{INT}(x, y) \tag{3.5}$$

The most common way to choose the clean beam is to fit an elliptical Gaussian to the main lobe of the dirty beam. The resulting beam will have the same width as the the dirty one, but no side-lobes.

There is no way to recover the *true* brightness distribution, as in the reconstructed image it will always be convolved with the interferometer response. What we can do is try to have a sampling function as complete as possible (many elements array with different separations; long observations to exploit the earth's rotation) to reduce the need of interpolation. What we can not do is to sample the innermost portion of the (u,υ) plane, because two antennas can not be placed closer than the diameter of the dishes. The minimum separation between

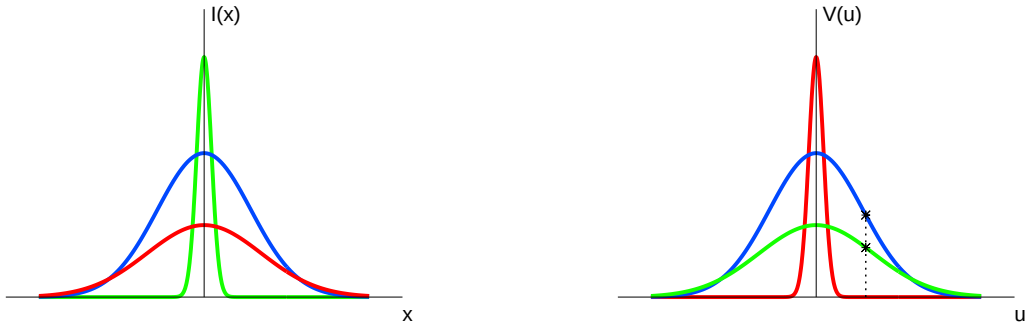

(a) Image (sky) domain.

(b) Fourier domain.

Fig. 3.3: Schematic mono-dimensional view of the relation between the brightness distribution $I(x)$ of a source and its Fourier transform $V(u)$ (qualitative). A narrow distribution in the image domain (green) transforms to a broad distribution in the Fourier domain and vice versa (red). A pair of antennas with given separation and observing at a wavelength λ places itself in a specific position in the u axis in the Fourier space (crosses).

the antennas constituting the interferometer d_{min}, i.e. the minimum spatial frequency u_{min}, determines the maximum physical scale structures in the source that can be measured by the interferometer. In particular, an interferometer with minimum separation d_{min} is not sensitive to structures larger than

$$x_{max}(rad) \sim \frac{\lambda}{d_{min}} = \frac{1}{u_{min}(\lambda)}. \tag{3.6}$$

This is the so-called *missing short (or zero) spacings* problem. In the same way, the maximum separation between the antennas d_{max} determines the minimum physical scale structure on the source that the interferometer is able to resolve, i.e. the resolution θ of the observations:

$$\theta_{INT}(rad) \sim \frac{\lambda}{d_{max}} \sim \frac{1}{u_{max}(\lambda)}. \tag{3.7}$$

Summarizing, *an interferometer with many elements acts as a filter of the spatial frequencies contained in a radio source, and it is sensitive only to those contained between the minimum u_{min} and the maximum u_{max} spatial frequency and, as a consequence, it is sensitive only to structures in the source with physical scales between the range* $\sim 1/u_{max} - 1/u_{min}$.

Figure 3.3 shows a schematic mono-dimensional view of the relation between the brightness distribution $I(x)$ of a source and its Fourier transform $V(u)$. A pair of antennas with given separation and observing at a wavelength λ samples the signals in the Fourier space corresponding to a specific spatial frequency u (crosses), i.e. it places itself in a specific position in the u axis in the Fourier space (crosses). A point-like source can be represented as a narrow Gaussian in the image plane (green Gaussian). Its Fourier transform will be a broader Gaussian in the Fourier domain, i.e. the source signal contains many Fourier components. A point-like source is therefore observed with good response either with small or large baselines. Vice versa, an

extended structure in the image domain (red Gaussian) will appear as a small Gaussian in the Fourier domain. The more extended is the source and more narrow will be its Fourier transform and more difficult will be sample the signal with small antennas separation. There will be a diameter for which the spatial frequencies contained in the radio source are all smaller than that sampled by the interferometer and no signal will be revealed. In this case some sort of shorter spacing data must be measured and added to the data. That might be interferometric data from a more compact configuration or it can be total power data from a single dish. Because any object larger than the primary beam will also suffer from short spacing problems, mosaicking usually implies the addition of total power to the interferometric data.

3.1.2 Theory of single dish observations

Further readings about single-dish radio astronomy include e.g. Stanimirovic et al. (2002).

Single dishes do not offer the possibility of instantaneous imaging as with interferometers by Fourier transform of the visibilities. Instead, several other methods of observation can be used. To take a real image with a single dish it is necessary to raster the field of interest (*mapping*), by moving the telescope e.g. along right ascension (RA), back and forth, shifting each scan in declination (DEC) with respect to the other by an amount of no more than ∼40% of the half-power beam width (HPBW) to fully sample the map. At centimeter wavelengths this has the advantage of allowing to cover a much larger area than with a single pointing of an interferometer. Moreover this method allows to adjust the map size to the size of the source of interest. Using this technique, a single dish is in principle capable of tracing all large-scale features of very extended radio sources. One may say that it *samples* spatial frequencies in a range from the the map size down to the beam width. This depends critically on the way in which the zero-level is set. The simplest way to do it is to assume the absence of sources at the map edges, set the intensity level to zero there, and interpolate linearly between the two opposite edges of the map. A higher-order interpolation is able to remove the variable atmospheric effects more efficiently, but it may also remove real underlying source structure. Rastering the field in two orthogonal directions may help in finding emission close to the map edges using the so-called *basket-weaving* technique (Sieber et al., 1979; Emerson & Graeve, 1988).
We can consider a single dish as consisting of a large number of small panels packed closely together acting as interferometer elements. In this way we can think of a single dish as an interferometer having a continuous range of baselines available from 0 to the diameter of the antenna D_{SD}. Single-dish observations then provide a measurement of the source total flux density, corresponding to the zero spacing (u, v)= (0,0). Mathematical representation similar to that for interferometers can be used for single dishes. The product of single dish observations is an image, that is a dirty image in the language of interferometer, because the clean process is usually not performed on single dish data (although techniques for single-dish map clean process have been proposed (see e.g. Klein & Mack, 1995)) and carried out (Rottmann et al., 1996).
The brightness distribution observed by a single-dish can be expressed, similarly to the interferometers case, as:

$$I^D_{SD}(x, y) = (I(x, y) * A_{SD}(x, y)) + N \tag{3.8}$$

where:

- $I^D_{SD}(x, y)$ is the observed brightness distribution;
- $I(x, y)$ is the true brightness distribution;
- $A_{SD}(x, y)$ is the single dish beam;
- N is a thermal noise term.

Similar to interferometer, *the source brightness distribution measured by a single-dish is the convolution of the true source brightness distribution by the single dish beam.* A_{SD} has very similar properties than A_{INT} but it defines the resolution of the observations:

$$\theta_{SD}(rad) \sim \frac{\lambda}{D_{SD}}. \tag{3.9}$$

Speaking in the language of interferometers, the Fourier transform of $I^D_{SD}(x, y)$ provides the "sampled" single dish visibilities $V'_{SD}(u, v)$: (N.B. properly speaking, a single-dish does not sample the source signal in the Fourier space!)

$$V'_{SD}(u, v) = (V(u, v) \times b_{SD}(u, v)) \tag{3.10}$$

where:

- $b_{SD}(u, v)$ is the Fourier transform of the single dish beam, i.e. the sampling function of the single-dish (that will be a continuous function from zero up to the spacing corresponding to the antenna diameter).

3.1.3 Theory of combination of interferometric and single dish data

A nice description of the principles of merging single dish and interferometric data is also given by Stanimirovic (1999) and Stanimirovic (2002)

The combination of interferometric and single-dish data allows to take advantage of both worlds, making high resolution images sensitive to a wide range of spatial scales and with the total power information. The idea is to use the single-dish "visibilities" to fill the inner portion of the (u,v) plane below $u_{min,INT}$, where the interferometer becomes blind.
In order to have a successful combination, the two data sets must have a region of overlap in the (u,v) plane, i.e. a sufficient range of spatial scales to which both instruments are sensitive. This translate in the condition that the single dish diameter must be greater than around twice the minimum interferometer baseline.
There are different methods to perform the data combination, involving different steps in the image or Fourier domain. For all of this methods the first important step is the cross-check of the calibration scales of the two data sets. The *calibration factor* f_{CAL} can be defined as the ratio of the flux density of an unresolved source in the interferometer and single-dish maps:

$$f_{CAL} = \frac{S_{INT}}{S_{SD}}. \tag{3.11}$$

In case of perfect cross-calibration $f_{CAL} = 1$. If no suitable compact sources are present in the field to directly determine f_{CAL}, this factor can be estimated comparing the surface brightness of the observed field in the overlap region of the (u,v) plane, where the same structures should be sampled by both the two instruments.

The different methods for the combination of single-dish and interferometric data can be summarized as:

- METHOD 1: In this method the inputs are the final clean (deconvolved) interferometric image I^C_{INT} and the final (non-deconvolved) single-dish image I^D_{SD}. These images are Fourier transformed (labeled as V'_{INT} and V'_{SD}) and combined in the Fourier domain applying the calibration factor and tapering functions, g and h (such that their sum is equal to the Gaussian function having a full width at half maximum of the interferometer):

$$V'_{COMB} = g \cdot V'_{INT} + f_{CAL} \cdot h \cdot V'_{SD}. \tag{3.12}$$

  The result is then Fourier transformed back into the image domain, providing the final combined image.
  This method was applied, for example, by Fletcher et al. (2011) and by Mora & Krause (2013).

- METHOD 2: In this method the inputs are the dirty (non-deconvolved) interferometric image I^D_{INT} and the final (non-deconvolved) single-dish image I^D_{SD} and both dirty beams B^D_{INT} and A_{SD}. This images are combined in the image domain according to:

$$I^D_{COMB} = \frac{I^D_{INT} + \alpha_{BEAM} \cdot f_{CAL} \cdot I^D_{SD}}{1 + \alpha_{BEAM}} \tag{3.13}$$

  and:

$$B_{comb} = \frac{B_{INT} + \alpha_{BEAM} \cdot A_{SD}}{1 + \alpha_{BEAM}} \tag{3.14}$$

  where $\alpha_{BEAM} = \theta_{INT}/\theta_{SD}$ accounts for the different beam sizes.
  The convolution relationship still exists between the composite dirty image I^D_{COMB} and the true sky brightness I, i.e. the composite dirty image is the convolution of the true sky brightness distribution with the composite dirty beam. Deconvolving (cleaning) the composite dirty image with the composite beam hence solves for I, providing the final combined image.
  This method was applied in Stanimirovic et al. (1999).

- METHOD 3: This method involves merging during the deconvolution, with subsequent joint deconvolution of the single-dish and interferometer data with different approaches (for example applying the maximum entropy method (MEM) as non-linear deconvolution algorithm). See Stanimirovic (2002) for more details.

- METHOD 4: Recently a new pipeline for the combination of single-dish and interferometric data has been proposed (Faridani et al., 2014). In this method the combination is performed completely in the image domain with a linear method. The inputs are the

final clean (deconvolved) interferometric image I^C_{INT} and the final (non-deconvolved) single-dish image I^D_{SD}. The interferometric image is first smoothed to the resolution of the single dish, and then subtracted from the single-dish data. The resulting difference image, containing only the large-scale emission detectable by the single dish, is then added to the interferometric image.

The final product of all these methods is an image whose resolution equals that of the interferometric image, while the total flux is the same as in the single dish image.
Stanimirovic (1999) shows a comparison of the performances of the first three methods. All methods produce comparable results in case of high S/N data. METHOD 1 is very robust and it is the fastest and least computer intensive. For low S/N data METHOD 2 seems advantageous. The MEM method is theoretically the best way but it heavily depends on the quality of the single-dish image. Moreover, joint deconvolution requires a good knowledge of the single-dish beam.
Finally we stress that the good result of the combination strongly depends on the quality of both single dish and interferometer data, as well as on the observational set-up adopted for both observations.

3.2 The radio relic in the Coma cluster

The Coma cluster, shown in the first Chapter in Fig. 1.1, is one of the nearest galaxy cluster (z=0.0232, Struble & Rood (1991)), and the first where both a peripheral radio relic (B1253+275) and a central radio halo (Coma C) have been observed (Large et al., 1959). Since then, both structures have been studied at several radio frequencies. Deep low frequencies observations have shown that a bridge of diffuse radio emission connects the halo, the relic and the tailed radio galaxy NGC4789 (Kim et al. (1989), Giovannini et al. (1990), Pizzo (2010), Brown & Rudnick (2011)). The presence of diffuse emission on even larger scales around Coma has been suggested by Kronberg et al. (2007).
The radio relic B1253+275 have been investigated by several authors in the last decades (Ballarati et al. (1981), Andernach et al. (1984), Giovannini et al. (1985), Cordey (1985), Giovannini et al. (1991), Thierbach et al. (2003), Pizzo (2010), Brown & Rudnick (2011)). However, its origin is still greatly debated.
Giovannini et al. (1991) first interpreted the relic as due to the past activity of the Coma galaxy IC 3900, which is presently radio quiet and was located at the center of the radio structure during the active phase and moved away after ceasing the nuclear activity. Alternatively, they suggested that the tailed radio galaxy NGC4789 could have provided electrons that underwent some kind of in-situ acceleration, to both the bridge and the relic. Enßlin et al. (1998) related the relic emission to the presence of an *accretion shock* wave caused by the formation of the large-scale structures. He also suggested NGC4789 as an ideal candidate for being the source of magnetized plasma injected upstream into the accretion flow. In this scenario, relativistic electrons from the jets of the radio source are convected by the flow within the radio bridge to the accretion shock where they are re-accelerated and radiate. However, accretion shocks are expected to have Mach numbers M >10 (Miniati et al., 2000), higher than what is usually observed in the relic position in different clusters (see e.g. Brüggen et al., 2012)). In the particular case of the Coma cluster, Feretti & Neumann (2006) did not detect any evidence

of a shock at the relic position, and suggested that it might have been formed by turbulence. However, Ogrean & Brüggen (2013) presented a re-analysis of the same XMM-Newton observation and measured a temperature jump at the SW edge of the relic which points towards the presence of a shock of Mach number $1.9^{+0.16}_{-0.40}$. However, no clear density discontinuity consistent with the temperature jump is observed. Akamatsu et al. (2013) found evidences of a shock with consistent Mach number from the analysis of Suzaku data.
Recently Brown & Rudnick (2011) tentatively detected an extension to the radio relic at 1.4 GHz, which makes its total extent ∼2 Mpc (in contrast with the size of ∼ 600 × 200 kpc previously reported by Giovannini et al. (1991)). The extended relic borders a previously undetected wall of galaxies in the infall region of the Coma cluster. They suggested that the radio relic is due to an *infall shock*, as opposed to the outgoing *merger shocks* believed responsible for other radio relics (see Sect.). The infall shock is caused by the dense clump of galaxies with its own intragroup medium, penetrating the ICM in the early stages of a merging event. They are different from merger shocks, which form during later stages of a merger.

3.3 Radio observations and data reduction

3.3.1 Effelsberg observations in the L-band

A ∼2 squared degrees field centered in the Coma cluster was observed with the Effelsberg-100m Telescope at a central frequency of 1408 MHz (21 cm; L band). The receiver used is a single horn system placed at the primary focus of the telescope. A total of 8 coverages of the entire field were preformed in the night between the 27 and 28 November 2013. Table 3.1 summarizes the observational parameters.

Tab. 3.1: L-band Effelsberg observational parameters.

Map center (J2000)		Frequency	Bandwidth	Map size
RA	DEC	(MHz)	(MHz)	(°× °)
12:57:25.17	+27:33:47.9	1408	32	2.1 × 2.1

The singular coverages maps were processed in the NOD2 software package, following standard procedures. After inspection and editing for Radio Frequencies Interferences (RFI), final images of the stokes I, U and Q were produced for each coverage using automatic pipelines available for each Effelsberg receiver. These images were then averaged together to produce the final I, U and Q images.
3C286 was used as calibrator of the flux scale (according to the scale of Baars et al. 1979, with a flux $S_{1408}(3C286) = 14.79$Jy) and of the polarization angle.
Figure 3.4 shows the final total intensity image of the entire field, where both the peripheral radio relic and the central radio halo emission are visible. The bridge of low brightness diffuse emission connecting the radio halo and radio relic observed at lower frequencies is also visible. The relic emission blends with the emission from tailed galaxy NGC4789 in the south-west direction, due to the low resolution and to the possible presence of a bridge of low-brightness emission connecting the two structures, observed at lower frequencies. The strong 3C source Coma A (3C277.3) is visible at the northern edge of the relic.

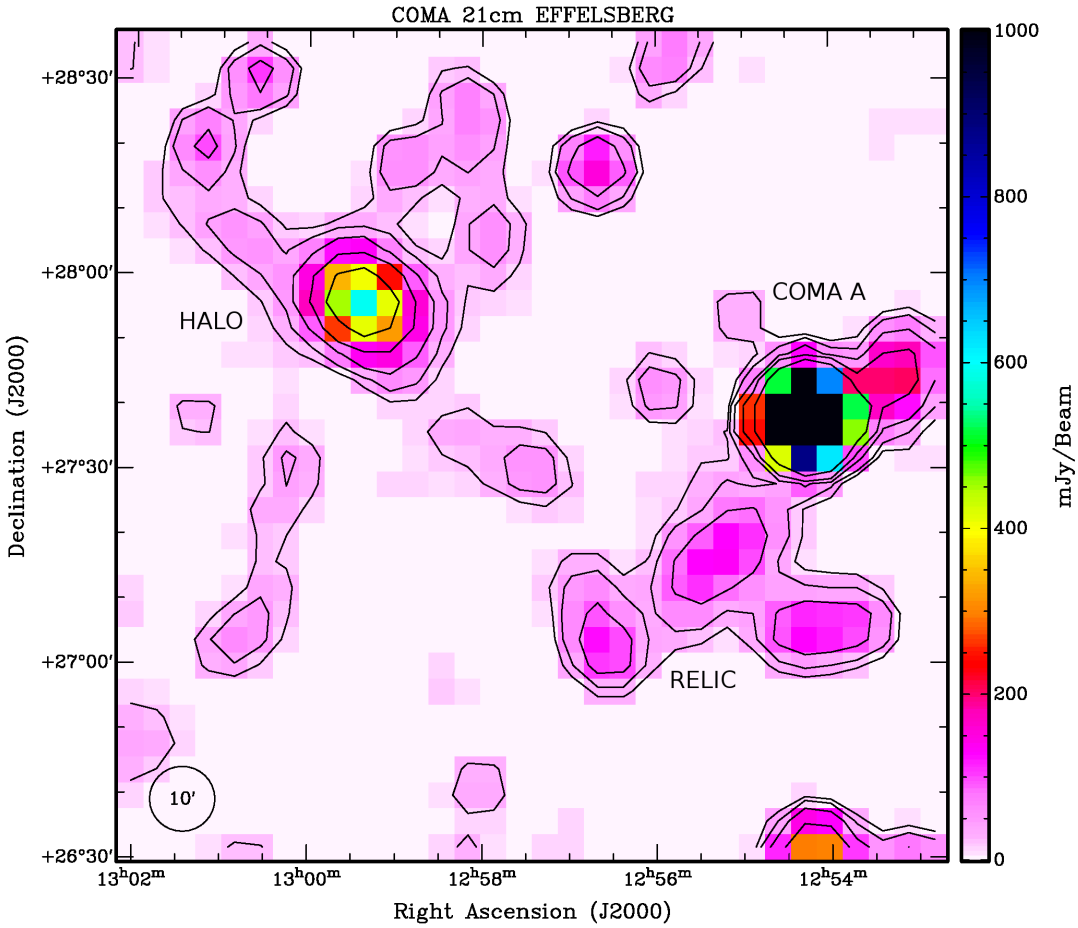

Fig. 3.4: Color scale and contours of the radio emission at 21 cm in the Coma cluster field, observed with the Effelsberg-100m Telescope. Contours are drawn at [1, 2, 4, 8, 16] × 3σ, with $3\sigma = 2 \cdot 10^{-2}$ Jy/beam. The beam is 9′.4 × 9′.4.

3.3.2 WSRT observations in the S-band

The radio relic in the Coma cluster was observed at 2273 MHz (13 cm, S-band) with the WSRT. The S-band receiver used, covers the frequency range from 2210.0 MHz to 2336.8 MHz with eight contiguous frequency bands (subdivided in 64 channels) of 20 MHz width each; the resulting central frequency is 2273 MHz and the total bandwidth is 160 MHz. The WSRT is an interferometer consisting of fourteen parallactic 25 m dishes on an east-west baseline that uses earth rotation to synthesize the uv-plane. Ten of the antennas (labeled RT0-RT9) are on fixed mountings, 144 meters apart, while the remaining four dishes (labeled RTA-RTD) are movable along two rail tracks, allowing different observing configurations. To observe the Coma radio relic we choose the maxi-short configuration (RT9-RTA separation of 36 m, RT9-RTB=90m, RT9-RTC=1332m, RT9-RTD=1404m) which has optimized imaging performance for extended sources.
The WSRT field of view at 2273 MHz is mainly limited by the effect of the primary beam

attenuation. For the WSRT this can be described by the function

$$cos^6(c \cdot \nu \cdot r) \tag{3.15}$$

where r is the distance from the pointing center in degrees, ν is the observing frequency in GHz and the constant c= 68 is, to first order, wavelength independent at GHz frequencies (declining to c=66 at 325 MHz and c = 63 at 4995 MHz). The resulting field of view at 2273 MHz is 0°.37. In order to image a field big enough to recover the relic extended emission, the observations were carried out in the *mosaic mode*. Three different pointing centers were chosen (details on Table 4.1). In order to have a good u, υ coverage for each pointing, the observations were performed switching the telescope from one pointing to another every five minutes, totalizing four hours of observations for each pointing for a total of twelve hours for the entire relic. Figure 3.1a shows a small portion of the (u,υ) coverage of the observation. The entire coverage extends up to $\sim$ 21 kλ, providing a potential resolution of $\sim 10''$, according to eq. 3.7. However, part of the very extended emission from the relic is missed because of the missing short spacing problem. The nominal minimum baseline of 36 m of the maxi-short configuration used, causes the observations to be not sensitive to structures larger than $\sim$12′.5, according to eq. 3.6.

The excellent phase stability of the WSRT system allows to observe primary calibrators

Tab. 3.2: S-band WSRT observational parameters.

Pointing center (J2000)		Frequency	Bandwidth	Exposure time
RA	DEC	(MHz)	(MHz)	(h)
12:54:49.999	+27:21:15.120	2273	160	4
12:55:15.000	+27:13:45.120	2273	160	4
12:55:40.000	+27:06:15.120	2273	160	4

only at the beginning and the end of an observation to calibrate the data. 3C286 and 3C147 were observed for this purpose. 3C286 was used as main flux density calibrator using the Baars et al. (1977) scale.

Careful inspection (on a channel by channel and baseline by baseline base) of the data were performed in order to remove RFI. Data were flagged also for antennas shadowing using the WSRT shadowing calculator available in the ASTRON web page[4]. Flagging, calibration, imaging and self-calibration were performed with the AIPS (Astronomical Image Processing System) package, following the guideline provided in the ASTRON web page[5].

The three pointings were imaged and self-calibrated separately with the IMAGR task in AIPS. Images of the Stokes parameter I, U and Q were obtained for each pointing and were then combined together (separately for I, U and Q) and corrected for the primary beam attenuation with the FLATN task in AIPS. Due to this correction, the rms noise at the map edges increase to $\sim 1.2 \cdot 10^{-4}$ Jy/beam, being $\sim 4 \cdot 10^{-5}$ Jy/beam at the map center. Figure 3.5 shows the final relic mosaic (the image shown is without primary beam correction). The high resolution of the observations allows to distinguish the diffuse relic emission from the emission of the

[4] `https://www.astron.nl/~heald/tools/wsrtshadow.php`

[5] `http://www.astron.nl/radio-observatory/astronomers/analysis-wsrt-data/.`

many discrete sources present in the field, some of which are labeled in the image. The relic emission shows a peculiar morphology that resemble that of a two-sided lobes radio galaxies, although, as already pointed out in literature, its large physical extent combined with its low radio brightness exclude the possibility that the relic is a normal radio-active galaxy. The tailed radio galaxy NGC4789, suggested to be the source of relativistic electrons re-accelerated in the relic emission, is visible in the south-west. The map does not show any bridge of diffuse emission connecting the tailed galaxy with the relic emission. Coma A is visible in the upper right corner of the image. However, it lies at the border of the northern pointing primary beam, and no reliable flux density measurements are possible there after the PB correction of the image.

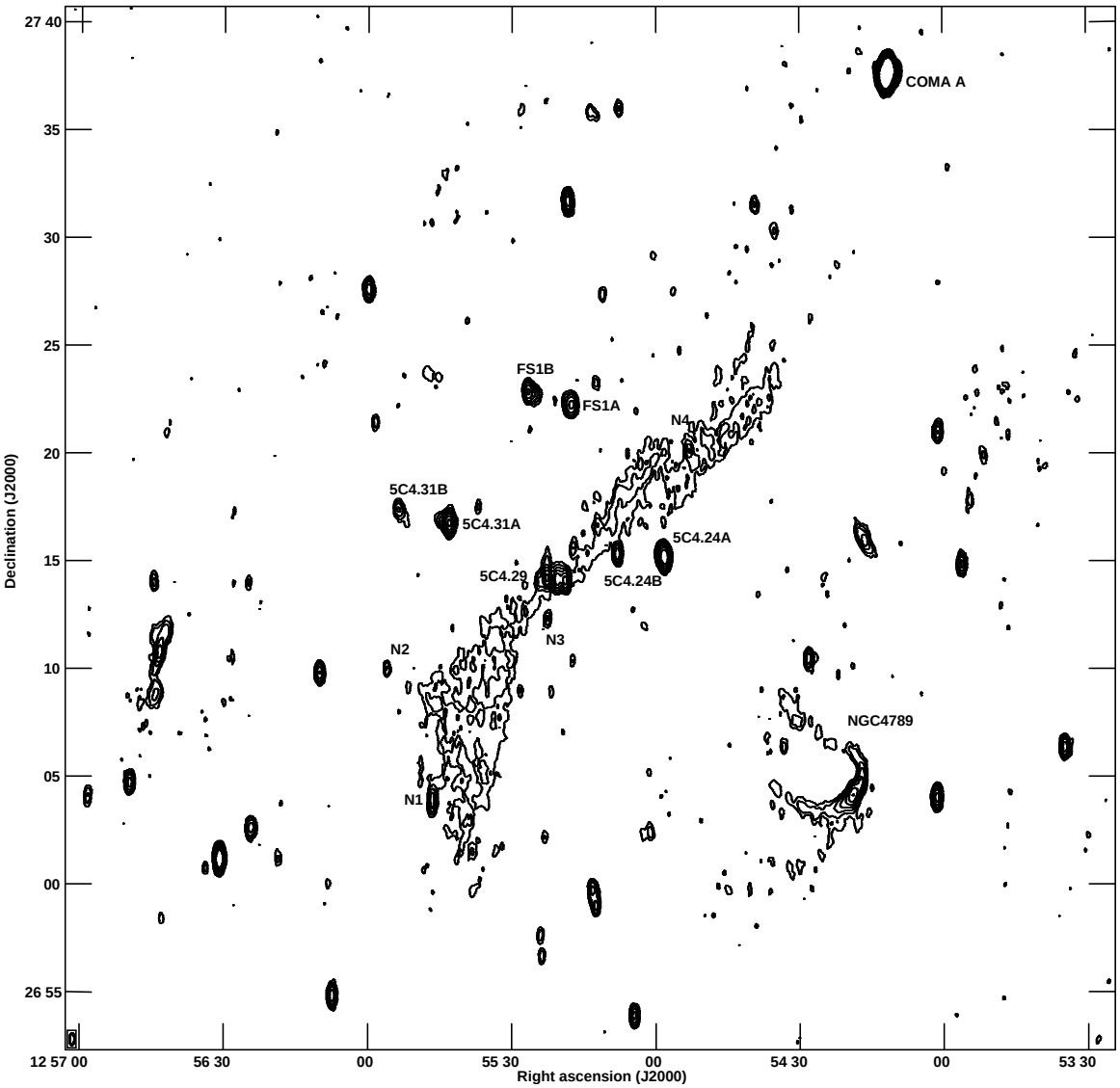

Fig. 3.5: Contours of the radio emission at 13 cm in the Coma relic field, observed with the WSRT. Contours are drawn at [1, 2, 4, 8] $\times$ 3σ, with 3σ = 7 $\cdot$ 10^{-5} Jy/beam. The beam, shown in the lower left corner of the image, is 33.′17 $\times$ 13.′16 at a position angle -0.67°. The image is not corrected for the primary beam attenuation.

3.4 Data combination in the L-band

To overcome the resolution poorness of the Effelsberg L-band image, we combined our data with data retrieved from the NRAO VLA Sky Survey (NVSS) (Condon et al., 1998). The NVSS is a 1.4 GHz continuum survey performed with the VLA interferometer, covering the entire sky north of -40° declination, with a set of 2326 continuum images of the Stokes I, Q, and U. Each of these images cover a 4°× 4° fields and can be obtained as FITS files using either a Web browser [6] or ftp. For our purpose we downloaded two adjacent fields (pointing center summarized in Table 3.3), as the field observed with Effelsberg fell at the border of the two NVSS fields. The two NVSS images were mosaicked in a single image with the FLATN task in AIPS.

Tab. 3.3: NVSS fields.

Name of the field	Pointing center (J2000)	
	RA	DEC
C1248P28	12:48:00.0	+28:00:00.0
C1304P28	13:04:00.0	+28:00:00.0

For the combination we choose the METHOD 1 presented in Sec. 3.1.3. The method has been performed with the IMERG task in AIPS. The steps performed within this task are:

- both the single-dish and cleaned interferometer images are Fourier transformed;
- the visibilities from both instruments are compared in the range of overlapping spatial frequencies, and a normalization factor, accounting for the calibration factor and the resolution difference between the two data sets, is calculated;
- after normalization, the single dish visibilities are merged with the interferometric visibilities producing an output consisting of the inner plane ($u < u_{min,INT}$) from the single-dish, the outer plane ($u > u_{max,SD}$) from the interferometer and a combination of the two within the overlapping region ($u_{min,INT} - u_{max,SD}$);
- the merged visibilities are Fourier transformed back in the image plane

The important parameters of the task are the range of overlapping spatial frequencies sampled (UVRANGE) and the normalization factor (FACTOR=$f_{CAL} \cdot \alpha_{BEAM}$). The latter can be calculated with the task itself, once the uv-range where to compare the visibilities is specified.
We first re-gridded the Effelsberg image to the same geometry as the NVSS image (same image size, same coordinate center, same pixel size) with the task OHGEO in AIPS. The blanked pixels in both images were set to zero. We used the strong 3C point source present in the field, Coma A, to check the calibration and alignment consistency between the Effelsberg and NVSS images. Table 3.4 summarizes the parameters obtained modeling the source with a Gaussian fit (JMFIT task in AIPS). We shifted the Effelsberg image accordingly to make the peak of Coma A coincident in the two images. We calculated the calibration factor as described in

[6] `http://www.cv.nrao.edu/nvss/findFITS.shtml`.

Tab. 3.4: COMA A parameters.

Parameter	NVSS image	Effelsberg image
Flux density (Jy)	2.980 ± 0.001	2.95±0.03
X-axis peak position (pixel)	694.73	692.45
Y-axis peak position (pixel)	937.26	938.55

Sect. 3.1.3 eq. 3.11 using the flux density of Coma A. We obtained $f_{CAL} = 1.01$. The resolution of the NVSS imag is $45'' \times 45''$, while that of the Effelsberg image is $9\farcm4 \times 9\farcm4$, giving a resolution ratio factor $\alpha_{BEAM} = 6.34 \cdot 10^{-3}$. The resulting FACTOR parameter is $6.4 \cdot 10^{-3}$.
In theory, one can calculate the exact UVRANGE of overlap from the size of the single dish and the shortest baseline of the interferometer and use it together with the above calculated FACTOR as input to the task to get the merged map. In practice the overlap between the two instruments is much more complicated than this, e.g. the single dish is not uniformly illuminated out to D_{SD}, especially at higher frequencies. For this reason we varied the UVRANGE parameter (within a plausible range) and let the task calculate the normalization factor. We chose the best uv-range as the one at which the FACTOR calculated by the task comparing the visibilities, equaled the factor we calculated. The NVSS shortest spacing sampled is $u_{min,INT}$ ~170 λ, corresponding to the minimum antenna separation of ~ 37 m (Condon et al., 1998). For Effelsberg, considering the whole aperture gives a $u_{max,SD} \sim 100m/0.21m = 476\lambda$, while assuming an aperture efficiency of ~ 54 % at 21 cm (as specified in the Effelsberg web page) we have $u_{max} \sim 257\lambda$. The final overlap uvrange, selected with the above criterion, is 170-240 λ.
The final combined map has a resolution of $45''$ and contains information on spatial frequencies in the range 0 - 4.5 kλ. It is the first complete image with high resolution available for the Coma radio relic at this frequency.
Figure 3.6 shows the comparison of the emission before (upper panel) and after (lower panel) the combination (both maps are smoothed to a resolution of $90''$ to increase the signal to noise ratio). The success in recovering the diffuse emission from the radio relic is evident. We checked the flux in the final combined image (with the original resolution of $45''$) inside the rectangular area showed in black in Fig. 3.6b. Results are summarized in Table 3.5. The flux difference between the images before and after combination inside the testing box is ~225 mJy. We checked the flux recovery with the combination process subtracting from the Effelsberg image the NVSS image convolved to the same resolution of $9\farcm4$ (shown in Fig. 3.7). In the image are visible the residual of the Coma A single-dish side-lobes after the subtraction. The residual flux calculated in the relic area is ~ 217 mJy. The flux densities of the point sources in the field is the same before and after the combination (within a 5% error), as expected. The data combination succeeded in recovering the missing extended emission from the diffuse relic. However the difference flux is likely not the proper flux density of the radio relic as it contains also some contribution form the bridge of emission connecting the relic with the tailed source NGC4789, as visible from Fig. 3.7. Moreover, some of the relic emission was already recovered in the NVSS image. In Sect. 3.7 we present the estimation of the relic flux density at this frequency.

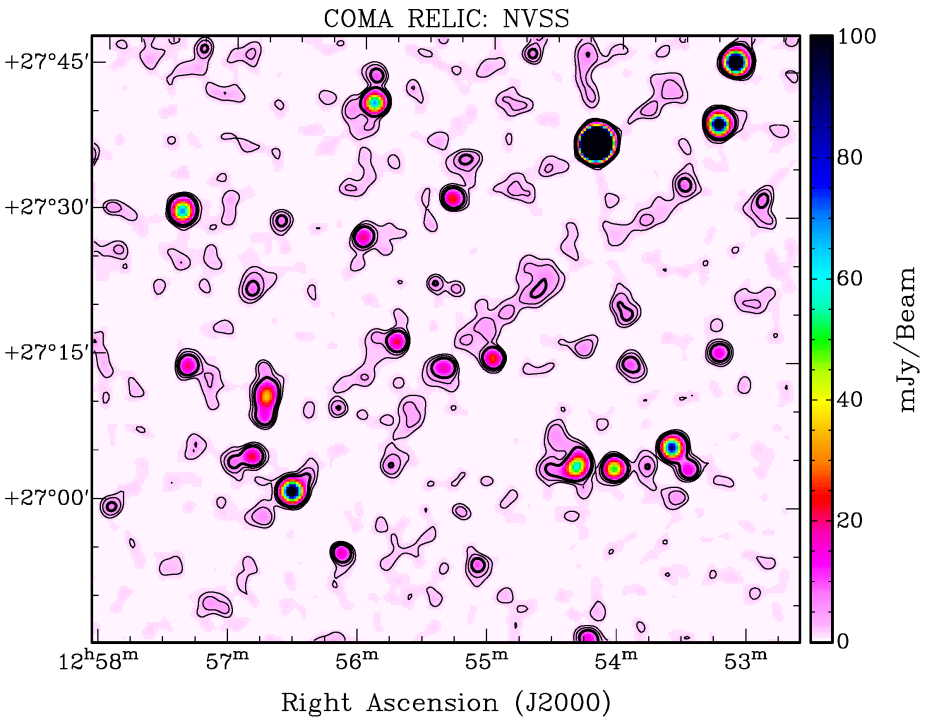

(a) Before data combination.

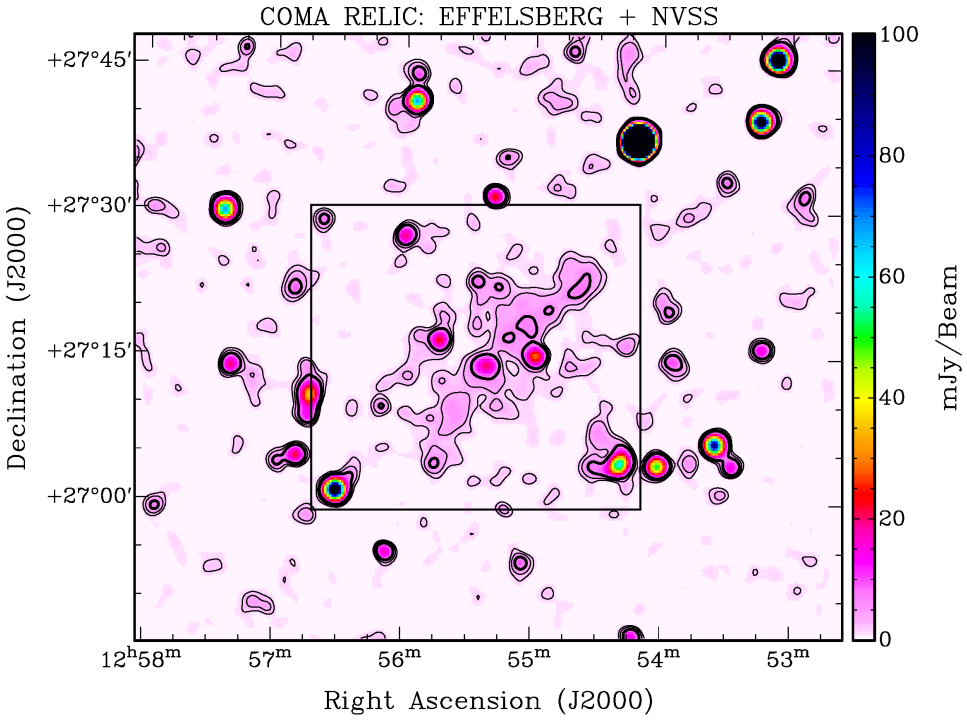

(b) After data combination.

Fig. 3.6: Comparison of the total intensity radio emission at 21 cm in the Coma relic field before and after data combination. Contours level are drawn at [1,2,4] × 0.0015 Jy/beam. The beam is 90″ for both images.

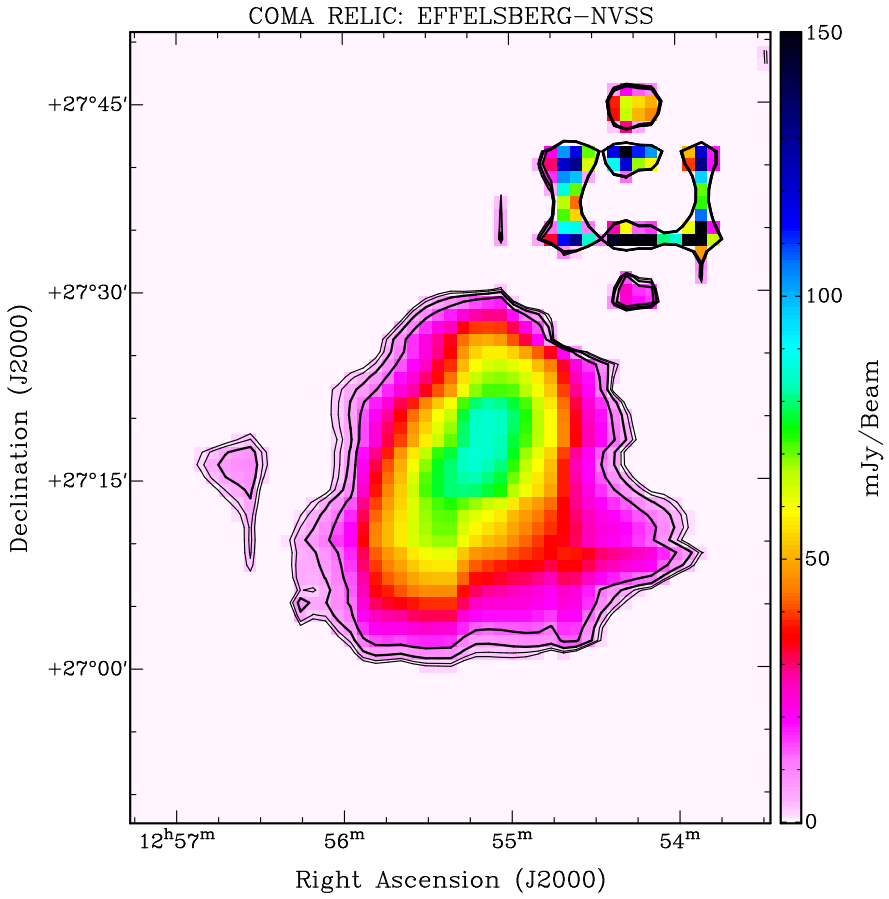

Fig. 3.7: Effelsberg 21 cm total intensity image of the Coma relic field with NVSS emission subtracted out. Contours are drawn at [1,2,4,8] × 0.001 Jy/beam. The beam is 9′.4 × 9′.4. Residuals of the Coma A single-dish side-lobes after the subtraction are visible in the upper-right corner.

Tab. 3.5: Flux density comparison before and after data combination in the L band.

Flux from NVSS map (mJy)	Flux from combined map (mJy)	Recovered flux (mJy)
327.3	552.8	225.5

(a) Testing box.

Name	RA (J2000)	DEC (J2000)	Flux from NVSS map (mJy)	Flux from combined map (mJy)
Coma A	12:54:11.6	27:37:32.6	2980	2980
	12:53:14.51	27:39:41.97	130.0	128.0
	12:53:06.9	27:46:06.9	190.0	189.0
	12:53:13.38	27:16:01.88	17.1	16.3
	12:53:34.78	27:06:13.99	93.2	92.5
	12:54:01.47	27:03:56.96	53.0	52.7
	12:56:30.98	27:01:08.8	133.0	133.0
	12:56:07.63	26:54:50.49	18.8	18.0
5C4.24A	12:54:58.43	27:15:12.17	27.0	29.6
5C4.31A	12:55:43.37	27:16:46.36	22.5	23.4
	12:55:18.30	27:31:40.22	25.7	24.7
	12:55:59.94	27:27:31.3	20.8	20.4
	12:57:24.33	27:29:54.61	77.0	76.1
5C4.29	12:55:21.04	27:14:11.04	23.4	27.9

(b) Field sources.

3.5 Data combination in the S-band

To overcome the zero-spacing problem and achieve complete spatial frequency coverage in the S-band observations, the missing information on larger scale was obtained from Effelsberg observations at 2.64 GHz (11 cm, S band; PI: E. Fürst, unpublished data). The total field size observed is 3°×3° and is centered in RA=12 59 24.81 DEC=27 43 50.1 (J2000), covering both the radio relic and halo emission. A total of 42 coverages were obtained along Right Ascension and Declination, providing a very sensitive map of the field. 3C286 was used as the main flux density calibrator according to the Baars et al. (1977) flux scale (S_{2640}=10.5 Jy). The flux scale was checked with Coma A, which has a flux of 1.93 Jy in the final calibrated map, as expected from Helmboldt et al. (2008). The big final map shows both the diffuse emission from the radio relic and the radio halo, as well as 160 point-like sources. The resolution of the image is 4.′4×4.′4.
The combination was performed with the IMERG task in AIPS. Different strategies were tested:

- individual combination of each WSRT pointing not corrected for the primary beam attenuation with the Effelsberg image convolved with the WSRT primary beam and subsequent mosaic with primary beam correction of the three merged images;
- individual combination of each WSRT pointing corrected for the primary beam attenuation with the Effelsberg image and subsequent mosaic of the three merged images;
- combination of the WSRT mosaic not corrected for the primary beam attenuation with the Effelsberg image convolved with the WSRT primary beam and subsequent primary beam correction of the merged image;
- combination of the WSRT mosaic corrected for the primary beam attenuation with the Effelsberg image;

We chose the last method, based on best results.
The first step was to regrid the Effelsberg image to the same geometry as the WSRT image . The blanked pixels in both images were set to zero. Coma A was modeled with a Gaussian and subtracted from the Effelsberg image before the combination. The resolution ratio between the two data sets is $\alpha_{BEAM} \sim 3.9 \cdot 10^{-3}$.
We checked directly the WSRT visibilities to see the effective u, υ-range covered by the observation; for all the three pointings we have u, υ-range ∼0.170-21 kλ. In the case of these observations, the combination is complicated by the small difference in the central observing frequency of the WSRT and Effelsberg observation (13 cm and 11 cm respectively) and by the absence, after the correction for the primary beam, of suitable point-like sources to directly calculate the calibration factor. This same problem has been overcome in the literature by using an average spectral index derived by a comparison of the flux densities of compact sources present in the field, to extrapolate the single-dish data to the center frequency of the interferometric data (see e.g. Kronberg et al., 2007). We pretended the Effelsberg observations to be at the same frequency of the WSRT and let the task calculate the normalization factor to match the visibilities amplitude in the overlapping region. Assuming an observing wavelength of 13 cm and an aperture of 100m, we obtain $u_{max;sd} \sim 770\ \lambda$. We varied the UVRANGE inside the range 170-770 λ. The best u, υ-range was judged by calculating the relic integrated flux in the

merged map and trying to get this as close as possible to the flux predicted from the integrated spectrum available in literature (α=1.19±0.06 Pizzo (2010), predicted flux S_{2273} = 128 ± 10 mJy). The final UVRANGE was 170-700 λ and the relic integrated flux in the merged map (after point source contribution subtraction) is 123 ± 12 mJy.
The final combined map has a resolution of $33''.17 \times 13''.16$, and complete uv-coverage in the range 0 - 21 kλ.
Figure 3.8 shows the relic emission in the S-band before and after the data combination. Also in this case the data combination succeeded in recovering the missing diffuse emission from the radio relic. The flux was missing along the minor axis of the relic. Table 3.6 summarizes the flux comparison of the relic and discrete sources before and after combination.

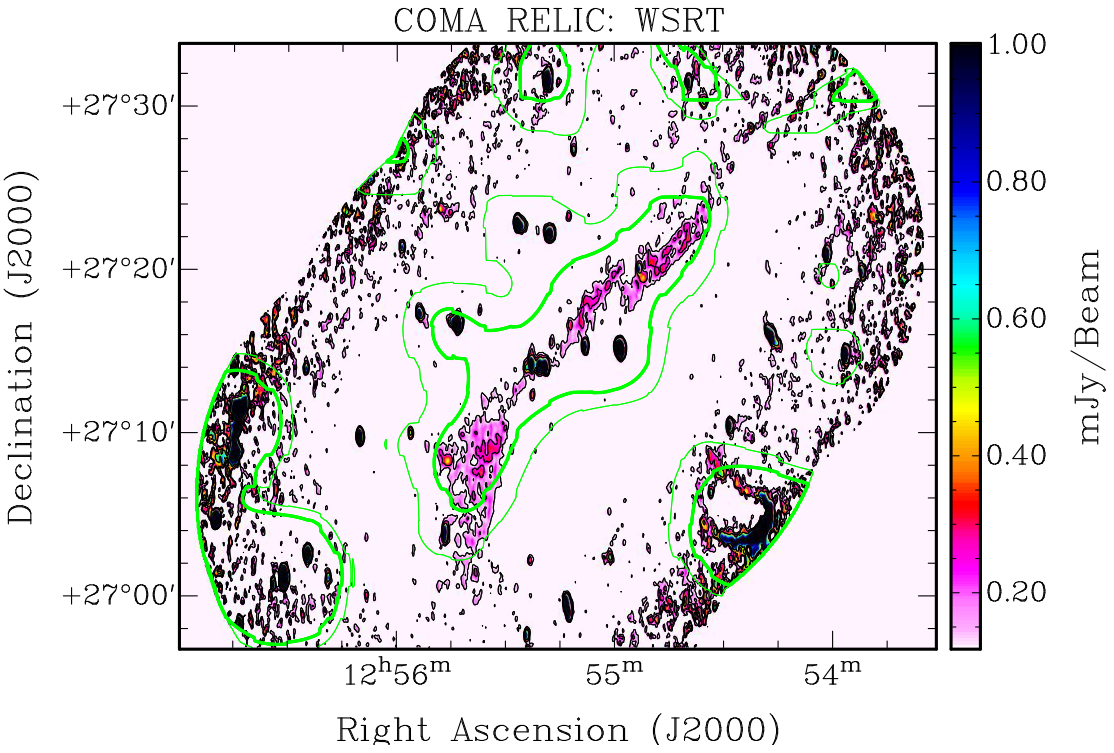

(a) Before combination.

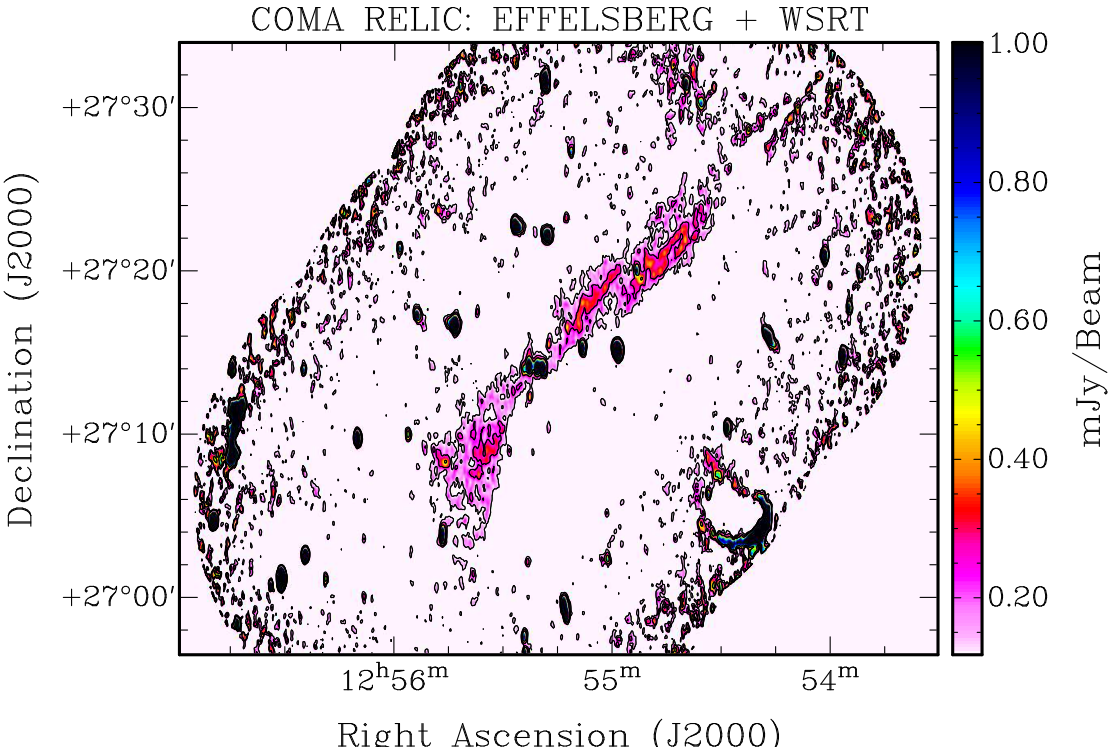

(b) After combination.

Fig. 3.8: Comparison of the total intensity radio emission at 13 cm in the Coma relic field before and after data combination (black contours and color scale). Black contours levels are drawn at [1,2,4] × 0.00012 Jy/beam. The beam is 33.″17 × 13.″16 at a position angle of -0.67°. Green contours in the upper panel represent the Effelsberg 11 cm map and are drawn at [1,2]× 0.007 Jy/beam.

Tab. 3.6: Flux density comparison before and after data combination in the S-band.

Flux from WSRT map (mJy)	Flux from combined map (mJy)	Recovered flux (mJy)
79.0	123.0	44.0

(a) Relic flux after subtraction of point source contribution.

Name	RA (J2000)	DEC (J2000)	Flux from WSRT map (mJy)	Flux from combined map (mJy)
FS1A	12:55:17.70	+27:22:15.12	5.01	5.19
FS1B	12:55:26.60	+27:22:51.09	7.70	7.85
5C4.31A	12:55:43.24	+27:16:49.44	14.1	14.2
5C4.31B	12:55:53.76	+27:17:23.04	2.25	2.37
5C4.24A	12:54:58.30	+27:15:13.56	23.1	23.2
5C4.24B	12:55:08.02	+27:15:21.11	3.06	3.24
	12:55:18.90	+27:14:05.40	5.56	5.86
5C4.29	12:55:20.57	+27:14:09.86	4.70	4.98
	12:55:22.76	+27:14:15.11	5.18	5.47
N1	12:55:46.67	+27:03:55.4	3.34	3.27
N2	12:55:56.14	+27:10:-1.24	0.62	0.75
N3	12:55:22.64	+27:12:21.11	0.42	0.61
N4	12:54:53.05	+27:20:06.01	1.47	1.88

(b) Field sources.

3.6 Is the relic 2 Mpc long?

Brown & Rudnick (2011) report a tentative detection of an extension to the Coma radio relic which makes its total extent ∼67′ (∼ 2 Mpc), in contrast with the size of ∼ 30′ reported by Giovannini et al. (1991) and Thierbach et al. (2003). The diffuse relic, as seen in their 1.4 GHz GBT image after a manual subtraction of the source Coma A, extends through the position of the subtracted source to the north-west. The extended relic is also seen in the image of the absolute value of the Stokes Q (without Coma A subtraction). However, in their WSRT 352 MHz image, the relic is only 28′ long. They argue that this is due to the instrumental contamination from Coma A.

None of our images support such an extension of the radio relic emission.
The low resolution of the 21 cm Effelsberg observations (Fig. 3.4) causes the relic emission to blend with Coma A in the north in the image, making a firm determination of the relic extent difficult. We estimate that the relic extends to ∼ 27.3′ before it blends with Coma A. The emission at the north-west of Coma A is due to the blending of the emission of two point sources (visible at higher resolution in the upper-right corner of Figs. 3.6). Moreover, in the difference image (Fig. 3.7) obtained by subtracting the NVSS image smoothed to the same resolution from the Effelsberg 21 cm image, the upper boundary of the relic emission is clearly visible. From this image we measure 29.′6 for the relic extent. The residuals of the Coma A subtraction are also clearly visible in the upper-right corner of the image. These residuals are due to the fact that the Effelsberg image is convolved with a *dirty* beam with secondary side-lobes, while the NVSS image is a *clean* image convolved with a *clean* beam where the secondary side-lobes have been removed. When convolving the NVSS image to the same resolution of the Effelsberg image, the width of the primary beam is the same, while the side lobes are still missing. The subtraction therefore leads to the positive residuals visible in the image.
Also at the higher resolution of the combined L-band image (Fig. 3.6b), the relic appears detached from Coma A, and no extension is clearly visible. At the resolution of this image, we measure a relic size of 27.′8. We remind that this image has complete uv-coverage from 0 up to ∼4.5 kλ, and any extended emission present in the field should be recovered with the Effelsberg+NVSS data combination.
The same holds true for the combined S-band image (Fig. 3.8b). However, the WSRT northern pointing borders at the position of Coma A, and the PB correction causes a local increase of the noise, which makes a firm statement about the borders of the relic emission difficult. However, Fig. 3.8a shows the contours of the Effelsberg 11 cm emission (green contours), where Coma A was subtracted with a Gaussian fit. The 3σ emission from the relic has clear borders in the north direction. Also in this case the residuals from the subtraction of Coma A are visible. From this image we measure ∼ 29.′64.
The values measured for the relic extent at different frequencies and at different resolution are summarized in Table 3.7.
We conclude that our data suggest an extent for the relic of no more than ∼30′ (∼ 800 kpc).
This is supported by images of the relic field available in the literature. In particular from observations at low frequencies, where lower brightness steep diffuse emission should come up more clear. For example in Fig. 6.4 from Pizzo (2010) at 150 MHz, where a big field of the Coma cluster is shown and where the bridge of emission connecting the halo, relic and

NGC4789 is clearly visible, the 3σ contours in the relic region clearly detach from the Coma A emission, and no extension to the north is visible. Fig. 1 of Venturi et al. (1990) also shows the radio emission at 326 MHz of a big field of the Coma cluster. Also in this case the relic does not extend further north of Coma A. Finally, no clear extension is visible in the new LOFAR images of the Coma cluster field retrievable in the web[7] for which the author reports a relic extent of $\sim$ 800 kpc. If any extended emission with very low brightness below the 3σ noise level of our images exists, it might not be directly related to the relic/shock, but rather with a larger scale diffuse emission on the scale of the Coma cluster.

Tab. 3.7: Coma relic extent at different wavelengths and resolution.

Ref. to image in text	Frequency (MHz)	Resolution	Extent in arcmin	Extent in kpc
Effelsberg L-band image 3.4	1408	$9'.4 \times 9'.4$	$\sim$ 27.3	$\sim$720.7
Effelsberg + NVSS image 3.6b	1408	$90'' \times 90''$	$\sim$ 27.8	$\sim$734.0
Effelsberg - NVSS image 3.7	1408	$9'.4 \times 9'.4$	$\sim$ 29.6	$\sim$781.4
Effelsberg S-band image 3.8a	2640	$4'.4 \times 4'.4$	$\sim$ 29.64	$\sim$782.5
Effelsberg + WSRT image 3.8b	2273	$33'.17 \times 13'.16$	$\sim$ 26.6	$\sim$702.2

3.7 The integrated radio spectrum of the Coma relic

In order to estimate the flux density of the diffuse relic emission, the flux contribution from the discrete sources embedded in the emission needs to be carefully subtracted. We used the source flux densities that we measured in our WSRT 2273 MHz image, the published flux at 1400 MHz (Giovannini et al., 1991) and the extrapolation of the fluxes to 2640 MHz. Sources flux densities are summarized in Table 3.8.

We calculated the flux of the relic at 21 cm from the combined NVSS+Effelsberg image presented in Sec. 3.4 (Fig. 3.6b). After subtracting the flux of the point-sources, we measure a relic flux S_{21cm} =195±20 mJy.
We calculated the flux of the relic at 11 cm from the original Effelsberg image (green contours in Fig. 3.8a). After subtraction of the source contribution we obtain a flux S_{11cm} =116±12 mJy.
Table 3.9 summarizes the flux of the relic densities calculated in the present work and published in literature. As these measurements arise from different works and are calculated from images produced with different telescopes, we raised the 1-σ error of the flux to 10% (where lower) for the computation of the total spectrum. The integrated spectrum of the Coma relic in the frequency range 139-4759 MHz is consistent with a straight power law with a spectral index $\alpha = 1.21 \pm 0.03$ (shown in Fig. 3.9), consistent with what was previously reported by Pizzo (2010). We did not use the flux of the relic at 2273 MHz measured in the combined map (Fig. 3.8b) for the spectrum fit, because it was forced to the value predicted by the previously published spectrum (see Sec. 3.5) and therefore it is not an independent measure. The data point is, however, plotted (open red circle) on the total spectrum for comparison.

[7] http://www.astron.nl/lofarscience2014/Documents/Tuesday/Session%20I/Bonafede.pdf

Tab. 3.8: Coma relic field sources.

Name	S_{1400} (mJy)	S_{2273} (mJy)	S_{4860} (mJy)	α_{1400}^{2273}	α_{2273}^{4860}	$S_{2.64}$ (mJy)
FS1A	8.10 ± 0.20	5.01 ± 0.17	—	1.05	—	4.28
FS1B	11.90 ± 0.26	7.70 ± 0.14	—	0.95	—	6.67
5C4.31A	21.70 ± 0.44	14.10 ± 0.14	7.80 ± 0.16	0.94	0.78	12.55
5C4.31B	6.80 ± 0.17	2.25 ± 0.15	—	2.42	—	1.56
5C4.24A	29.90 ± 0.60	23.10 ± 0.15	8.60 ± 0.17	0.56	1.3	19.01
5C4.24B	3.60 ± 0.12	3.06 ± 0.12	1.80 ± 0.05	0.35	0.70	2.75
	7.40 ± 0.18	5.56 ± 0.166	1.90 ± 0.05	0.63	1.41	4.50
5C4.29	4.20 ± 0.13	4.70 ± 0.20	4.40 ± 0.10	-0.25	0.09	4.64
	7.80 ± 0.18	5.18 ± 0.17	1.80 ± 0.05	0.9	1.4	4.20
N1	7.94 ± 1.36[a]	3.34 ± 0.17	—	1.9	—	2.51
N2	—	0.62 ± 0.11	—	—	—	—
N3	—	0.42 ± 0.14	—	—	—	—
N4	5.13±1.45[a]	1.47 ± 0.15	—	2.73	—	1.00

[a] Measured from NVSS image.

In the scenario of diffusive shock acceleration for radio relics (see Sect. 2.3.2) and applying the Rankine-Hugoniot conditions, this spectral index predicts a shock Mach number $M = 3.2^{+0.28}_{-0.15}$.

Tab. 3.9: Coma relic integrated flux densities.

Frequency (MHz)	Flux densities (Jy)	References
139	4.0 ± 0.2	Pizzo (2010)
151	3.3 ± 0.5	Cordey (1985)
326	1.4 ± 0.03	Giovannini et al. (1991)
408	0.91 ± 0.10	Ballarati et al. (1981)
610	0.611 ± 0.05	Giovannini et al. (1991)
1400	0.195 ± 0.020	present work
2273	0.123 ± 0.013[a]	present work
2640	0.116 ± 0.012	present work
2675	0.112 ± 0.010	Thierbach et al. (2003)
4759	0.054 ± 0.015	Andernach et al. (1984)

[a] Forced to this value (see Sec. 3.5 for more details).

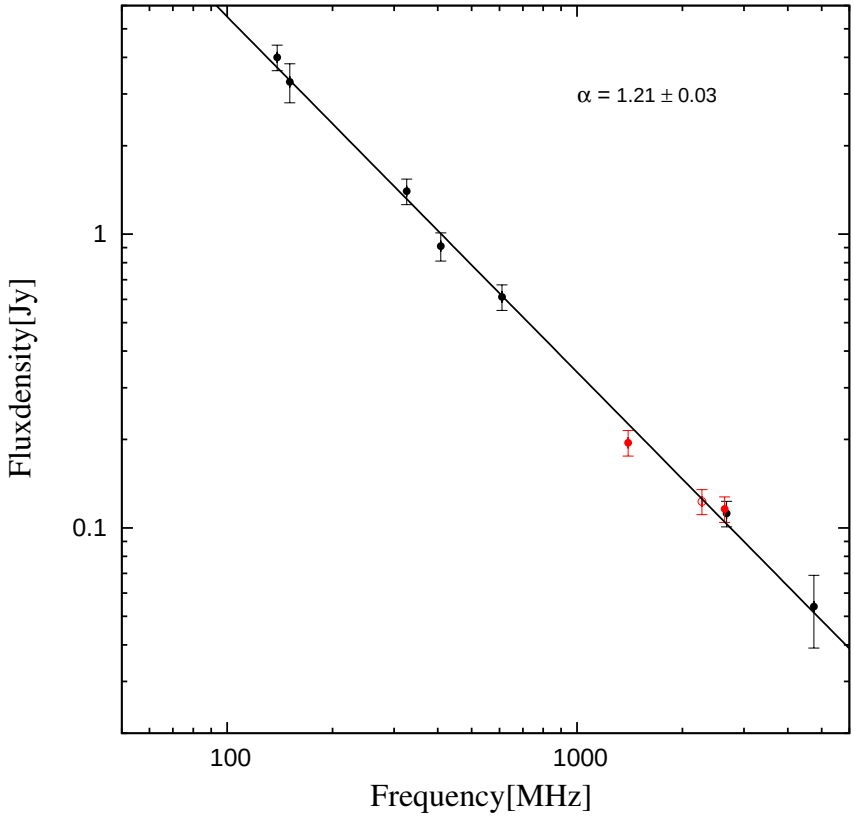

Fig. 3.9: The Coma relic integrated radio spectrum. Black circles are flux density values from literature, while red circles are measurements from this work. The open red circle represents the relic flux at 2273 MHz that was not used for the fit (see text for more details).

3.8 Planck SZ determination of a pressure discontinuity*

The detection of shock features at radio relic positions have so far been obtained through X-ray observations. An independent method for confirming the presence of shock waves at radio relic positions would be to detect the pressure discontinuity directly from the Sunyaev-Zel'dovich (SZ) effect imaging. The SZ effect measures the line-of-sight integral of the pressure of the thermal gas, and recent instrumental advances have opened up the SZ effect as a promising tool to study cluster astrophysics. Yet no direct determination of the shock front at radio relics from SZ has been published. Here we report a first tentative detection of a pressure discontinuity at the position of the Coma relic from the analysis of SZ data.

A $30° \times 30°$ map of the Comptonization parameter y (see Sect. 1.2.2) was constructed from Planck data by forming linear combinations of maps, using all six frequency bands of the Planck High Frequency Instrument. The data were taken from the nominal 15-months survey (Planck data release 2013). A Gaussian filter was applied to smooth all maps to a common resolution of $10'$. More details on the data reduction can be found in Erler et al. (submitted to MNRAS). The resulting Compton-y map is shown in Fig. 3.10. The noise level on pixel scale is $\sigma_{pix} = 2.16 \times 10^{-6}$, in good agreement with the noise properties of the Planck published results on Coma by the Planck team (Planck Collaboration et al., 2013b).

We investigate the ICM pressure in the relic direction as seen from the Planck data, and

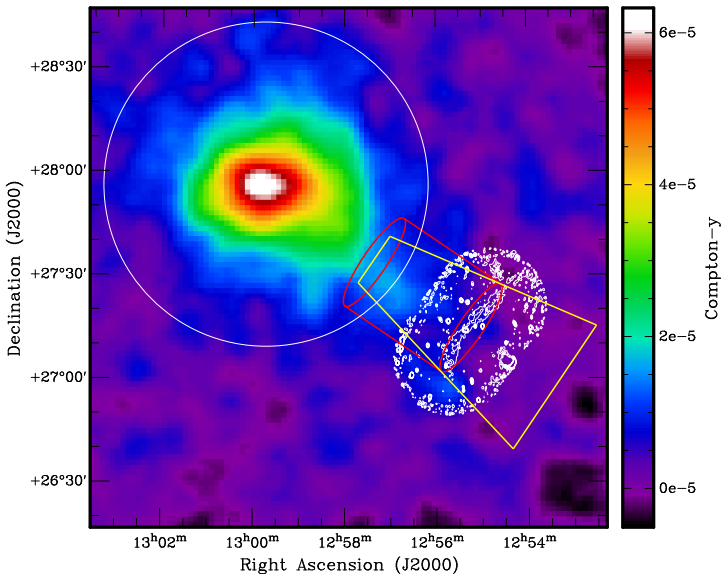

Fig. 3.10: The Comptonization map derived from the linear combination of Planck data. The thin white circle denotes the R_{500} for Coma, the white contours are from the S-band combined image and show the position of the relic, which is located at roughly $1.6 \times r_{500}$. The red cylinder shows our assumed geometry of the 3D pressure tube, consistent with the relic length, and the yellow wedge marks the 2D region from which the profile used during our analysis is extracted.

whether a pressure discontinuity is directly visible at the position of the radio relic. We used the S-band combined image (Sect. 3.5) to constrain the position and width of the relic/shock

*Erler, Basu, Trasatti, Klein, Bertoldi (submitted to MNRAS)

front. High-frequency radio emission in a radio relic should mark the location of freshly accelerated electrons closest to the shock front, it is a cleaner indicator of the shock front geometry. Due to the high ratio between the major and minor axis of the radio relic, we assumed that it represents an edge-on shock front in the plane of the sky. Figure 3.11 shows the result of radial profile extraction along 18 identical cones of width 20° from the Coma cluster center (12:59:47, +27:55:53). The blue data points are the projected pressure along the direction of the relic, whose errors are computed from the covariance of 1000 similarly shaped cones in a 30° × 30° y-map. The other solid lines mark the y-profiles in other directions, with the two neighboring cones marked separately in color. Clearly, there is an excess of pressure in the re-

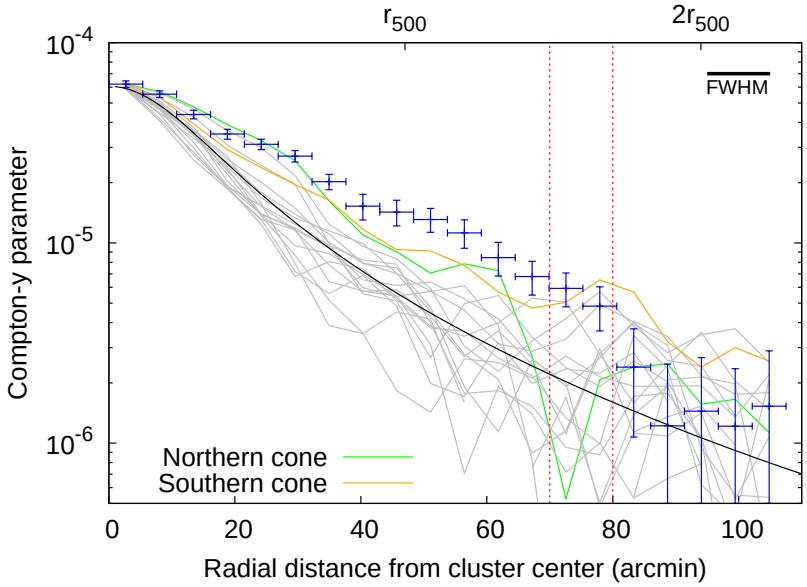

Fig. 3.11: SZ profiles for the Coma cluster. The blue data points with errors mark the radial profile along the relic direction, extracted from a cone-shaped region of opening angle 20°. The thin gray lines mark the radial profiles in similar cones in all the other radial directions. The two neighboring cone profiles below and above the relic cone are additionally marked in color. The black continuous line is the GNFW model fit for the average radial profile, excluding the cone that contains the radio relic. The two vertical dotted lines mark the prior boundaries on the radio relic position derived from the S-band radio data.

gion between R_{500} and R_{200} of the cluster in the relic direction, roughly terminating at the edge of the relic as seen from radio data (the relic width is shown by the two vertical dotted lines). Inside R_{500} the high pressure comes from a general elongation of the Coma cluster in this direction, as also noted by the Planck collaboration analysis. Beyond the relic position the data is generally consistent with noise for all cones. We can see an indicative jump for the projected pressure where the radio relic ends, but its significance is low. To quantify this small effect and deproject the underlying pressure discontinuity, we explored different classes of models (more details in Erler et al. submitted to MNRAS). Of the three models we tested, a power law featuring a pressure discontinuity at the position of the relic provides the best fit to the SZ data. The best fit pressure ratio suggests a mildly supersonic shock ($M \sim 3$), bolstering the hypothesis of shock origin of the Coma radio relic. Our Mach number results are tied to the assumption of a "shock tube" geometry, which we base on the high-resolution radio measurement of the

Coma relic. The S-band radio data fixes the width of the propagating shock front (or the high pressure filament) at roughly 730 kpc in the plane of the sky. Such cylindrical shock fronts can be seen from the hydro simulations of cluster mergers (e.g. Vazza et al., 2012), and therefore provides a simple yet realistic model for deprojecting the Planck y-map. The derived Mach number value agrees within one σ with the estimates from the radio spectral index (Sect. 3.7), as well as with estimates from XMM Newton ($M = 1.9^{+0.16}_{-0.40}$, Ogrean & Brüggen (2013)) and from Suzaku ($M = 2.2 \pm 0.5$, Akamatsu et al. (2013)). The current SZ-based errors are larger than the X-ray spectroscopic measurements, although different X-ray studies vary widely on their treatment of background systematics and the quoted X-ray Mach numbers do not necessarily reflect on those systematics (e.g. Simionescu et al. (2013) fails to derive a meaningful temperature measurement beyond the relic position using the same *Suzaku* data).

The analysis of the SZ data (with radio priors) presented in this section supports the idea of an outwardly moving shock front, likely caused by the first infall of the group NGC 4839. We find no evidence for inward moving shock from the pressure profile models. However, the causal connection between the infalling group NGC 4839 and the shock front detected at the radio relic remains speculative, and we do not claim to know the origin of the shock that is likely causing the radio emission in the Coma relic.

3.9 Conclusion

In this chapter we have presented a radio and Sunyaev-Zeldovich analysis of the radio relic in the Coma cluster. The main point of this study can be summarized as follows.

- We presented new observations of the Coma radio relic performed at 1400 MHz (=21 cm, L-band) with the Effelsberg-100m Telescope and at 2273 MHz (=13 cm, S-band) with the WSRT. The Effelsberg observations cover a wide field on the Coma cluster, and both the peripheral radio relic and the central radio halo are visible. The bridge of low brightness diffuse emission connecting the halo and the relic is also visible. The high resolution of the WSRT observations allows to distinguish the diffuse relic emission from the emission of the many discrete sources present in the field. The relic emission shows a peculiar morphology that resemble that of a two-sided lobes radio galaxies, although, as already pointed out in literature, its large physical extent combined with its low radio brightness exclude the possibility that the relic is a normal radio active galaxy.

- We showed the results of single-dish and interferometric data combination in the L and S bands. The method presented is powerful and allow to recover the large-scale diffuse emission, preserving a high resolution, which make it well suitable for the study of diffuse emission in galaxy clusters at GHz frequencies.

- None of our image support the tentatively detection claimed in literature of an extension to the radio relic which makes its total extend $\sim$ 2 Mpc. Our data suggest an extent for the relic of no more than $\sim 30'$ ($\sim$ 800 kpc), in agreement with other authors in literature.

- We presented new relic flux density measurements at 1400 and 2640 MHz. Fitting our data with data available in literature we find that the Coma relic integrated spectrum in the frequency range 139-4759 MHz is consistent with a straight power law with a

spectral index $\alpha = 1.21 \pm 0.03$, consistent with what previously reported. In the scenario of diffusive shock acceleration for radio relic and applying the Rankine-Hugoniot conditions, this spectral index predicts a shock Mach number $M = 3.2^{+0.28}_{-0.15}$.

- We collaborated in the analysis of SZ Planck data to investigate whether a pressure discontinuity is directly visible at the position of the radio relic. We tested different models and found that a power-law featuring a pressure discontinuity at the position of the relic provides the best fit to the SZ data. The best fit pressure ratio suggests a mildly supersonic shock ($M \sim 3$), in agreement with what predicted from the radio integrated spectrum, bolstering the hypothesis of shock origin of the radio relics. The analysis supports the idea of an outwardly moving shock front, likely caused by the first infall of the group NGC 4839.

Chapter 4

The radio relic in Abell 2256: overall spectrum and implications for the electron acceleration*

4.1 Introduction

The proposed formation mechanisms differ in the predictions of the morphological and spectral characteristics of the different classes of relics. DSA of both thermal and pre-accelerated electrons, should produce larger and more peripheral structures, with strong polarization, and pure power-law integrated synchrotron spectra (Brüggen et al., 2012). Fermi processes naturally predicts an *injection* power law energy distribution for the accelerated electron population of the form[1] $f(E) \propto E^{-\delta_{inj}}$. From synchrotron theory, the emission produced by this population of electrons is also described by a power law[2]

$$S(\nu) \propto \nu^{-\alpha_{inj}} \qquad \text{with} \qquad \alpha_{inj} = \frac{\delta_{inj} - 1}{2}. \tag{4.1}$$

Emitting particles are naturally subject to energy losses. These losses are governed by many physical factors such as the properties of the magnetic field (see Kardashev, 1962; Jaffe & Perola, 1973; Komissarov & Gubanov, 1994, for a description of the different models of electron aging). The absence of any constant injection of new electrons would lead to a cutoff in the high energy region of the integrated spectrum, moving towards lower frequencies in the course of time. The presence of constant injection of particles with the same energy spectrum, on the other hand, would eventually mask the cutoff, leading instead to a break with a change of 0.5 in the spectral index of the integrated emission (Kardashev, 1962):

$$\alpha_{obs} = \alpha_{inj} + 0.5. \tag{4.2}$$

This condition translates, in case of DSA, in the assumption that the properties of the shock remain unchanged (stationarity for the shock). If the shock has been present in the ICM for a time exceeding the electron cooling time, a single power law with spectral index α_{obs} is ex-

*Trasatti, Akamatsu, Lovisari, Klein, Bonafede, Brüggen, Dallacasa, Clarke (subm. to A&A)

[1]The distribution is truncated at high energy due to the existence of a maximum energy to which electrons can be accelerated.

[2]The synchrotron spectrum has an exponential cutoff at high frequency reflecting the truncation in the particle distribution.

pected for the integrated radio spectrum (stationarity for the spectrum). The observed spectral indices reported in Table 4 of Feretti et al. (2012) for straight integrated spectra range from 1.1 to 1.6. A gradient is expected in the spectral-index distribution across the source, with the flattest values marking the position of the shock front where the particle get accelerated and the steepening showing the radiative losses as the electrons are advected away from the shock. Such a gradient is clearly observed in the radio relic in CIZA J2242.8+5301 (van Weeren et al., 2010; Stroe et al., 2013).
In case of revival via adiabatic compression of old radio plasma left behind by radio galaxies and pushed towards the cluster outskirts by buoyancy, we expect instead more filamentary and smaller radio structures (< 50 kpc), again strongly polarized, but with steeper and curved integrated spectra due to the already aged population of electrons that are re-accelerated. In fact the adiabatic compression would just shift the already aged spectrum at high energies upward, without modifying the spectral slope. Even steeper spectra are expected in case of AGN relics. The average spectral indices reported in Table 4 of Feretti et al. (2012) for integrated spectra with measured steepening, range from 1.7 to 2.9.
With these ingredients, detailed studies of the integrated spectrum and of the spectral-index distribution across the sources, allow to test the current models and study the shock properties in case of DSA. This is accomplished by observations made over a broad range of frequencies. However, an accurate measurement of the integrated spectra of radio relics is a difficult task. These sources usually contain a number of discrete sources, whose flux density needs to be carefully subtracted from the total diffuse emission. This requires high-resolution imaging at many frequencies using radio interferometers. However, increasing the observing frequencies, interferometers encounter the technical problem of the *missing short spacings* that makes them "blind" to very extended structures. On the other hand, single dishes are optimal to catch all the emission from a field but they lack angular resolution. Indeed, integrated spectra over a wide range of frequencies are available in the literature only for few of these objects (see Feretti et al., 2012).
An independent measure of the properties of shocks is provided by deep X-ray observations. Through the measurements of temperature and/or pressure jumps at the location of the shock, properties such as the shock Mach number M and the shock compression ratio C can be inferred (see review by Brüggen et al., 2012). In the *test particles approximation*[3] of DSA, if the particle diffusion is specified, the shock Mach number is the primary parameter that determines the efficiency of the acceleration mechanism and the energy distribution of the particles at injection (Kang & Ryu, 2010). In this case, a simple direct relation between the shock Mach number M and the injection index δ_{inj} of the energy electrons distribution exists:

$$\delta_{inj} = \frac{2(M^2 + 1)}{(M^2 - 1)}. \tag{4.3}$$

However, radio relics are usually observed in the outskirts of clusters where the very low density of electrons ($n_e < 10^{-4}$ cm^{-3}) make the detection of shocks in the X-ray very challenging (Akamatsu & Kawahara, 2011). Indeed, few clear X-ray shock detection are known in literature (see review by Brüggen et al., 2012). In conclusion, multi-frequency radio measurements, combined with deep X-ray observations, allow a search for and a proper study of these shocks to test the shock-origin model for relics.

[3]When the dynamical feedback of the Cosmic Rays electrons pressure is ignored.

4.2 The radio relic in Abell 2256

One of the most intriguing clusters hosting both a radio relic and a radio halo is the galaxy cluster A 2256 ($z = 0.058$). It also shows all typical signatures of a merging cluster system although its dynamical state is not yet completely understood. This cluster has been the first observed with LOFAR at very low frequencies (20 - 63 MHz) by van Weeren et al. (2012b). They collected data up to 1400 MHz and found a radio integrated spectrum for the relic that can be described by a power law with a relatively flat spectral index $\alpha_{63}^{1369} = 0.81 \pm 0.03$. The occurrence of similar flat spectral indices have been reported by Kale & Dwarakanath (2010) in the frequency range 150-1369 MHz. Assuming stationary conditions in the test-particle case of DSA, this would require an injection spectral index which is not consistent with the flattest possible injection spectral index from DSA . Indeed, a direct consequence of the test-particle approach to DSA is that in the limit of strong shocks ($M \gg 1$) the particle index δ_{inj} approaches a asymptotic value of 2. This means that particle energy distribution produced by test-particle DSA cannot be flatter than 2 (it must be $\delta_{inj} \gtrsim 2$). As a consequence the synchrotron spectra at injection cannot be flatter than 0.5 ($\alpha_{inj} \gtrsim 0.5$). So, we should not observe relics with spectra $\alpha_{obs} \lesssim 1$. The flat spectrum could be reconciled with shock acceleration if the shock has been produced very recently ($\sim$ 0.1 Gyr ago) and stationarity has not been reached yet. In this case a steepening of the integrated spectrum is expected at frequencies $\gtrapprox$ 2000 MHz.
In this chapter we present new high-frequency radio observations (Sect. 4.3) of A 2256 at 2273, 2640 and 4850 MHz MHz performed both with an interferometer (the Westerbork Synthesis Radio Telescope, WSRT) and a single dish (the Effelsberg-100m Telescope), complemented by X-ray observations (Sect. 4.4) performed with the Suzaku and XMM-Newton satellites. In Sect. 4.5 we present a new determination of the relic radio spectrum over the widest sampled frequency range collected so far for this kind of object (63 MHz-10450 MHz)[4]. In Sect. 4.6 we show the ICM temperature in regions across the radio relic emission. In Sect. 4.7 we consider the effect of the thermal Sunyaev-Zeldovich (SZ) decrement on our flux density measurements at high frequencies. Discussion and conclusions are presented in Sects. 4.8 and 4.9.
We adopted the cosmological parameters H_0 =71 km s^{-1} Mpc^{-1}, Ω_Λ=0.73 and Ω_m=0.27 (Bennett et al., 2003), which provide a linear scale of 1.13 kpc arcsec^{-1} at the redshift of A 2256.

4.3 Radio observations and data reduction

A 2256 was observed with the WSRT at 2273 MHz and with the Effelsberg 100-m telescope at 2604 and 4850 MHz.
In this section we present the observations and the main steps of the calibration and image-making process. All the observations include full polarization information. In this section we focus on the total intensity properties of the cluster. We postpone a detailed local analysis based on polarization properties and spectral index maps to Chap. 5.

[4] A very recent paper reports the first observation of a radio relic at 16 GHz (Stroe et al., 2014).

4.3.1 WSRT observations in the S-band

For this project we choose for the WSRT the maxi-short configuration which has optimized imaging performance for very extended sources. The receiver covers the frequency range from 2210.0 MHz to 2336.8 MHz with eight contiguous IFs of 20 MHz width each; the resulting central frequency is 2273 MHz and the total bandwidth is 160 MHz. We are potentially sensitive to emissions on scale up to $\sim 13'$ with a full resolution of $\sim 9''$.
The main limiting factor of the field of view is the effect of the primary beam attenuation. For the WSRT this can be described by the function $cos^6(c \cdot \nu \cdot r)$ where r is the distance from the pointing center in degrees, ν is the observing frequency in GHz and the constant c= 68 is, to first order, wavelength independent at GHz frequencies (declining to c=66 at 325 MHz and c = 63 at 4995 MHz). The resulting field of view at 2273 MHz is 0.37°. In order to image a field big enough to recover the extended emission in A 2256, the observations were carried out in the *mosaic mode*. Three different pointing centers were chosen (details in Table 4.1). In order to have a good uv coverage for each pointing, the observations were performed switching the telescope from one pointing to another every five minutes, having four hours of observations for each pointing for a total of twelve hours for the entire cluster. The excellent phase stability of the system allow to observe primary calibrators only at the beginning and the end of an observation to calibrate WSRT data. 3C286 and 3C48 were observed for this purpose.

Flagging, calibration, imaging and self-calibration were performed with the AIPS (Astro-

Tab. 4.1: WSRT Observational parameters.

Pointing center (J2000)		Frequency	Bandwidth	Exposure time	Telescope
RA	DEC	(MHz)	(MHz)	(h)	configuration
17 01 07.998	+78 45 03.701	2273	160	4	maxi-short
17 04 25.000	+78 45 03.701	2273	160	4	maxi-short
17 02 42.300	+78 34 59.988	2273	160	4	maxi-short

nomical Image Processing System) package, with standard procedures following the guideline provided on the ASTRON web-page[5].3C286 was used as the main flux density calibrator using the Baars et al. (1977) scale (task SETJY in AIPS). The three pointings were imaged and self-calibrated separately. A multi-resolution clean was performed within the IMAGR task in AIPS to better reconstruct the complex diffuse emission present in the cluster. Images of the Stokes parameter I, U and Q were obtained for each pointing and were then combined together (separately for I, U and Q) and corrected for the primary beam attenuation with the FLATN task in AIPS.

4.3.2 Effelsberg observations in the S and C bands

Part of the observations were performed with the Effelsberg 100m Telescope. We used the 11 cm (=2640 MHz) and 6 cm (=4850 MHz) receivers. Single-dish observations do not suffer from the zero-spacing problem, and can trace large scale features, although with modest resolution.

[5] `http://www.astron.nl/radio-observatory/astronomers/analysis-wsrt-data/`.

The data reduction of Effelsberg data was performed with the NOD2 software package, following the standard procedures provided on the MPIfR web-page[6]. The raw images of both A 2256 and the calibrators were partly processed using dedicated pipelines available for each receiver. The default strategy to calibrate Effelsberg data is to observe primary calibrators during the session and then use automatic 2-D Gauss fit pipelines to calculate the factor to scale the final image converting it from mapunit/beam to Jy/beam (task RESCALE in AIPS).

Observations at 2640 MHz

The Effelsberg 11 cm receiver is a single-horn system equipped with a polarimeter with eight small-band frequency channels, each 10 MHz wide, covering the frequency range 2600-2680 MHz, plus one broad-band channel, 80 MHz wide, over the same frequency range. The resulting central frequency is 2640 MHz and the total bandwidth is 80 MHz. The resolution of the observation is $4\farcm5 \times 4\farcm5$.
To map the A 2256 field we used the *mapping mode*, which consist in rastering the field of interest by moving the telescope e.g. along longitude (l), back and forth, each sub-scan shifted in latitude (b) with respect to the other. At centimeter wavelengths atmospheric effects (e.g. passing clouds) introduce additional emission/absorption while scanning, leaving a stripy pattern along the scanning direction (the so-called scanning effects). Rastering the same field along two perpendicular directions (both along longitude and latitude) helps in efficiently suppressing these patterns, leading to a sensitive image of the region (Emerson & Graeve, 1988). This technique, called *basket-weaving technique*, helps also in setting the zero-base level. The details of the observations are summarized in Table 4.2. For each coverage of the field, the receiver provides four images (R, L, U, Q) for each of the nine channels. As circular polarization is generally very weak, the images in R and L are very similar and can be averaged in the later steps of data reduction providing the total intensity image.
We performed a total of 14 coverages in the longitude direction and 15 coverages in the latitude direction; due to RFI (Radio Frequency Interference) and pointing problems we had to discard a small portion of the data. The time required to complete one coverage is $\sim$ 17 minutes in both direction, so we have a total observing time on source of 8.2 hours. The observations were carried out in the night between the 15th and 16 August 2012.
3C286 and 3C48 were used as absolute flux density calibrators using the Baars et al. (1977)

Tab. 4.2: Effelsberg observational parameters.

Map center (J2000)		Frequency	Bandwidth	Map size
RA	DEC	(MHz)	(MHz)	($'\times'$)
17 04 00	+78 04 00	2640	80	48×48
17 04 00	+78 04 00	4850	500	40×35

scale that provide flux densities at 2640 MHz of 10.65 Jy and 9.38 Jy respectively for the two calibrators.

[6]https://eff100mwiki.mpifr-bonn.mpg.de/doku.php?id=information_for_astronomers:user_guide:reduc_maps .

Observations at 4850 MHz

The Effelsberg 6 cm receiver is a double-horn system, with the two feeds fixed in the secondary focus with a separation of 6 cm, each with one broad-band (500 MHz) frequency channel in the range 4600-5100 MHz. The resulting central frequency is 4850 MHz and the total bandwidth is 500 MHz. The resolution of the observation is $2\farcm43 \times 2\farcm43$.
Multi-horn systems use a different technique to overcome the scanning effect problem. The scanning is done in an azimuth-elevation coordinate system, and must be done only in azimuth direction so that all horns will cover the same sky area subsequently. At any instant each feed receives the emission from a different part of the sky but they are affected by the same atmospheric effects, which then cancel out taking the difference signal between the two feeds (Emerson et al. 1979). Similarly to the 11 cm receiver, data in (R, L, U, Q) are provided for each of the two horn.
We performed a total of 25 coverages of the A 2256 field, 15 during the night between the 22nd and the 23rd of June and 10 on the 26th of June 2011. Due to RFI problems only 22 coverages could be used.
For the calibration we observed 3C286 and NGC7027 during the session. The flux densities used for the two calibrators are 7.44 Jy (from Baars et al., 1977) and 5.48 Jy (from Peng et al., 2000) respectively.

4.4 X-ray observations and data reduction

In this section we present the X-ray observations of A 2256 performed with Suzaku and XMM-Newton and the main steps of data reduction.
Suzaku observed the radio relic region in A 2256 (OBSID: 801061010) with an exposure time of 95.2 ks. The satellite X-ray Imaging Spectrometer (XIS: Koyama et al. 2007) has a very low detector background, which allows to investigate weak X-ray emission targets such as cluster outskirts (see Reiprich et al., 2013, for a review). The XIS was operated in the normal clocking, 3×3 and 5×5 mode. To increase the signal-to-noise ratio we filtered the dataset using a geomagnetic cosmic-ray cut-off rigidity (COR) > 8 GV. The filtered exposure time is 89.2 ks. The data were processed using standard Suzaku pipelines (see Akamatsu et al., 2012, for more details).
We complemented Suzaku observations with XMM-Newton observations retrieved from the archive (Rev. 0619 and 0651 performed on the 2003-04-27 and 2003-06-30 respectively) and reprocessed with SAS v11.0.1. The data were heavly affected by soft proton flares. The data were cleaned for periods of high background due to soft proton flares with a two stage filtering process (see Lovisari et al., 2009, 2011, for more details on the cleaning process). In this screening process bad pixels have been excluded and only event patterns 0-12 for the MOS detectors and 0 for the pn detector were considered. The filtered exposure time is ∼19 ks for MOS1, ∼20 ks for MOS2 and ∼9 ks for pn.
For both satellites the background emission can be described as the sum of a particle background component and a sky background component. The former is produced by the interaction of high-energy particles with the detectors. The latter can be subdivided into at least two thermal components, one unabsorbed due to the Local Hot Bubble (LHB: kT∼0.08 keV) and

one absorbed due to the Milky Way Halo (MWH: kT~0.3 keV), and a power-law component due to the Cosmic X-ray Background (CXB: Γ=1.41).
The particle background has been modeled and subtracted from the data of both satellites before the spectral fits presented in Sect. 4.6.1. For the Suzaku observations its contribution has been estimated from the Night-Earth database with the *xisnxbgen* FTOOLS (Tawa et al., 2008). For XMM-Newton the particle component spectra have been extracted from the filter wheel closed (FWC) observations and renormalized by using the out-of-field-of-view events. These spectra were supplied as background spectra to the XSPEC fitting routine.
Unlike the particle background, the sky background was not subtracted from the data but its different components were modeled together with the ICM emission during the spectral fitting. To fix the model parameters for the different components in Suzaku observations, we used spectra extracted from a 1 degree offset observation performed with the satellite (PI: Kawaharada, OBSID: 807025010). For XMM-Newton data, we followed the method presented in Snowden et al. (2008) in which the different components are estimated using a spectrum extracted from ROSAT data in an annulus beyond the virial radius of the cluster. The offset spectra were fitted with a sky background model considering the LHB, MWH and CXB components. In the fitting, we fixed the temperature of the LHB component to 0.08 keV. Abundance (Anders & Grevesse, 1989) and redshift of LHB and MWH were fixed to 1 and 0, respectively. The temperature of the MWH determined in the fit is 0.21 ± 0.03 keV. We also checked for the possibility of an additional "hot foreground" component with $kT \sim 0.6 - 0.8$ keV (Simionescu et al. 2010) adding another thermal component to the background model described above. However, the intensity of this additional component resulted not significant in the offset field and was not included in the background modeling.

4.5 Radio analysis and results

4.5.1 Radio images

WSRT image

In Figure 4.1 we present the 2273 MHz total intensity WSRT image of the central region of A 2256. The image has been produced with natural weighting of the visibilities in the range $[u_{min} - u_{max}]$=[260 - 21035 λ]. The shortest spatial frequency sampled u_{min} determines the largest spatial scale recovered by this observations $LSS \simeq 1/u_{min} = 13'.22$. The image has been corrected for the primary beam attenuation that determines an increase of the noise in the edge of the image. The high resolution ($9''.84 \times 9''.44$) allowed us to analyze the substructures of the diffuse relic emission in detail. The map shows several of the well-known radio features present in the cluster (notation from Bridle et al., 1979; Rottgering et al., 1994): the radio relic emission (sources G and H), the head-tail sources A, B, C and I, the complex source F (here resolved in the three components F1, F2 and F3), as well as many other discrete sources, some of which labeled in this work as I2, I3, K2, G2, J2. The radio halo emission present in the center of the cluster around source D (Clarke & Ensslin, 2006) is completely filtered out due to a combination of effects: its low surface brightness at this frequency, combined with the lack of sampled short spacings in the WSRT observations, that determines the loss of the very extended weak emission.
The relic emission exhibits two regions of enhanced surface brightness: a well-defined arc-like

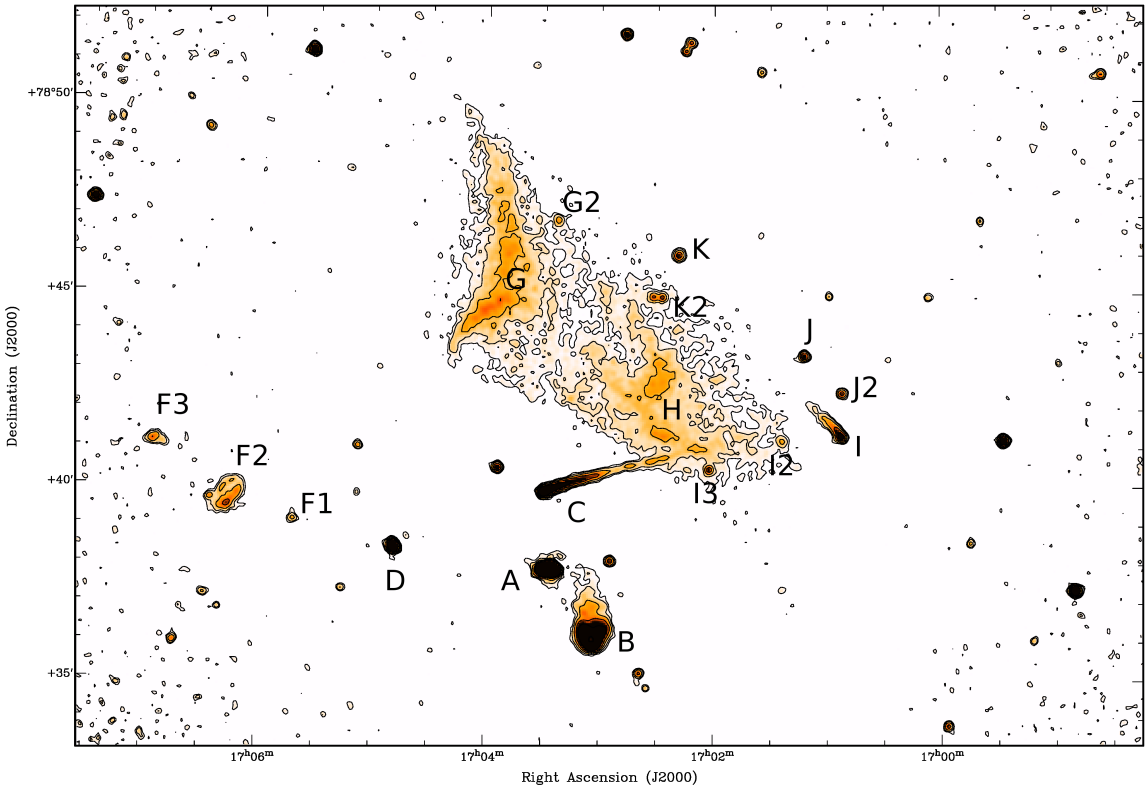

Fig. 4.1: WSRT 2273 MHz total intensity radio image with contours drawn at [1, 2, 4, 8] × 3σ, with $3\sigma = 8 \cdot 10^{-5}$ Jy/beam and color scale starting at the same level. The beam size is $9\farcs84 \times 9\farcs44$. The image is corrected for the primary beam attenuation.

region (G region) in the northern part, and a less defined region (H region) in the western part (see Fig. 4.1). The two regions are connected by a bridge of lower brightness emission. At full resolution the entire relic emission covers an area of about $10\farcm6 \times 5'$. The size reported by Clarke & Ensslin (2006) at 1.4 GHz and at a resolution of $52'' \times 45''$ is $16\farcm9 \times 7\farcm8$. Convolving our WSRT image to the same resolution we obtain a similar angular size (not shown). Nevertheless, as we might be anyway missing some of the flux on the most extended scales, we do not use this image for the computation of the relic integrated spectrum.

EFFELSBERG images

In Figure 4.2 we show the 2640 MHz (left panel) and 4850 MHz (right panel) Effelsberg images of A 2256. In both images, the diffuse emission from the relic is mixed up with the emission from the more compact sources present in the field due to the low resolution of the observations. In the 2640 MHz image the relic emission is blended with the emission from the A+B+C complex and from source F. At 4850 MHz it is easier to separate the relic emission from the emission of the A+B complex, but still part of the tail of source C is inevitably superimposed on the Western part of the relic. Moreover, Brentjens (2008) derived a spectrum α=1.5±0.2 for the radio halo between 351 and 1369 MHz. If there is no steepening in the spectrum of the halo, we expect a flux density of $\sim$ 37 mJy at 2640 MHz and a flux density of $\sim$ 15 mJy at 4850 MHz. Since a single dish is sensitive to all the emission in the field,

its emission is smoothed with the other sources in our Effelsberg images if the halo spectrum keeps straight at these frequencies. Constraining the halo spectrum at high frequencies would require a dedicated careful analysis that is beyond the aims of this work.

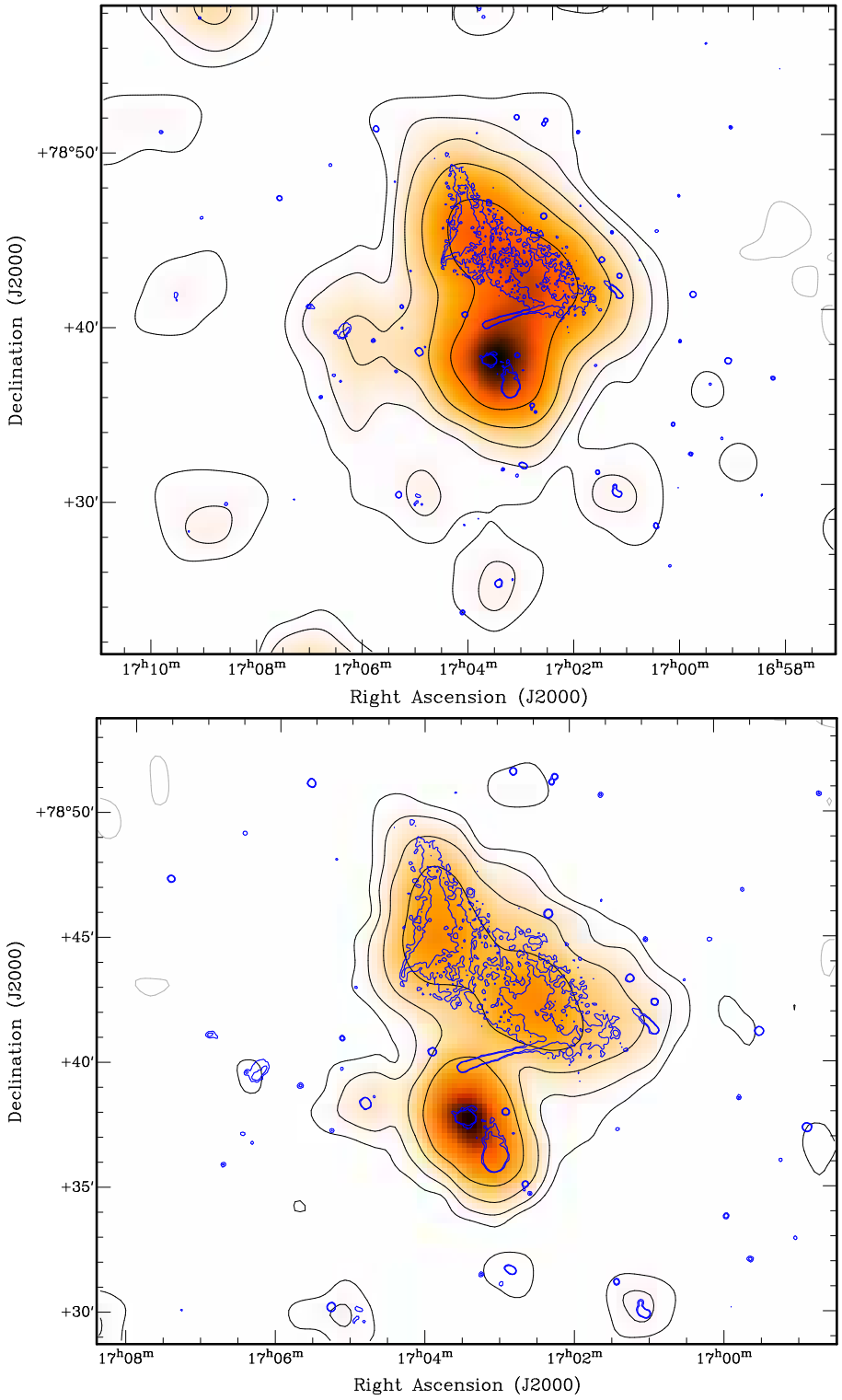

Fig. 4.2: Upper panel: Effelsberg 2640 MHz total intensity radio image in color scale and black contours drawn at [-1, 1, 2, 4, 8, 16] × 3σ, with $3\sigma = 4 \cdot 10^{-3}$ Jy/beam. The beam size is 4.′4 × 4.′4. Lower panel: Effelsberg 4850 MHz total intensity radio image in color scale and black contours drawn at [-1, 1, 2, 4, 8] × 3σ, with $3\sigma = 1.86 \cdot 10^{-3}$ Jy/beam. The beam size is 2.′43 × 2.′43. In both images the blue contours are from the WSRT 2273 MHz radio image not corrected for the primary beam attenuation and are drawn at [1, 2] × $8 \cdot 10^{-5}$ Jy/beam.

4.5.2 Spectral analysis

For the spectral analysis of the radio relic in A 2256 we combined our high-frequency observations with images obtained at other frequencies provided by the authors: the 351 MHz WSRT image (Brentjens, 2008), the 1369 MHz VLA C and D configuration images[7] (Clarke & Ensslin, 2006) and the Effelsberg 10450 MHz image (Thierbach, 2000). We moreover got information on the flux densities in the LOFAR image at 63 MHz published by van Weeren et al. (2012b) by the author. All the different images were calibrated according to the flux scale of Baars et al. (1977) or to its extension to lower frequencies (below 408 MHz; Perley & Taylor, 1999) [8]. In this way we were able to cover the widest range of frequencies (63 MHz- 10.45 GHz) used so far for the determination of the spectrum of a radio relic.
We estimated the uncertainties σ_S on the flux density *measurements* S with the following formula:

$$\sigma_S = \sqrt{{\sigma_{rms}}^2 + {\sigma_{cal}}^2}, \tag{4.4}$$

where:

- $\sigma_{rms} = rms \times \sqrt{N_{beam}}$ is the error due to the image noise, with rms being the image rms noise level (in the chapter referred to as σ level) and N_{beam} the number of beams covered by the source;
- $\sigma_{cal} = E_{cal} \times S$ is the error due to calibration uncertainties, determined in turn by two factors: the accuracy of the absolute flux density scale adopted and the uncertainties related to the application of such scale to our data; being these two factors uncorrelated we used $E_{cal} = \sqrt{\epsilon^2_{scale} + St^2_{scale}}$.

The spectral data provided by Baars et al. (1977) for the flux density calibrators have an absolute uncertainty of 5%. For the term St^2_{scale} we used the standard deviation on the calibration factor derived from the Gaussian fit of the calibrators images produced during the session for the Effelsberg observations, and the dispersion of antenna gains for the WSRT data. This translates into errors of 1.6% for the Effelsberg 11cm data, of 1.2% for the Effelsberg 6 cm data and of 2% for the WSRT 13 cm data. Combining this with the uncertainties on the Baars et al. (1977) scale, we end up with $E_{cal}(11cm)$=5.3%, $E_{cal}(6cm)$=5.2% and $E_{cal}(13cm)$=5.4%. For the other images we assumed a similar value St_{scale}=6%.
Where not otherwise specified, we estimated the uncertainties σ_f on the quantities f *calculated* from measured quantities χ_i (e.g. spectral indices and extrapolated flux densities of discrete sources) applying the following error propagation formula:

$$\sigma_f = \sqrt{\sum_{i=1}^{N} \left(\frac{\partial f}{\partial \chi_i}\right)^2 \cdot \sigma^2_{\chi_i}}. \tag{4.5}$$

[7] We used the high resolution C configuration data to measure the flux density of discrete sources while for the determination of the relic flux density we used the D configuration image.

[8] The overall flux scale for the LOFAR observations at 63 MHz was obtained comparing the measured integrated flux densities of five bright sources in the field of view with predicted fluxes partly based on flux densities measurements from the 1.4 GHz NVSS (Condon et al., 1998) and the 74 MHz VLSS (Cohen et al., 2007), both based on the Baars et al. (1977) scale.

The spectra of the total cluster, relic+sources, relic, G and H regions presented in the next sections have been determined calculating the flux densities at different frequencies on images convolved to the same lowest resolution available ($4\farcs4 \times 4\farcs4$) and with the same regions for the integration. The errors associated to the spectral indices are the errors from the fits of the data.
All the spectra, including those of the discrete sources embedded in the relic emission, are plotted over the same fixed x-axis range (frequency range 40 - 14000 MHz) for easy comparison.

Total cluster emission

We first considered the integrated radio flux density of the entire cluster (halo, relic and discrete sources combined) measuring the flux density in the circular region centered at J2000 position α = 17 03 45 δ = +78 43 00 with 10′ radius, as described by Brentjens (2008). The cluster radius was determined by Brentjens (2008) as the one at which the derivative of the integrated flux within the circle respect to the radius of the circle settles to a constant value. The measured flux densities at 351, 1369 (D configuration), 2640, 4850 and 10450 MHz are summarized in Table 4.5. The total cluster radio emission between 351 and 10450 MHz can be modeled by a single power-law with spectral index α= 1.008 ± 0.018 (Fig. 4.10a).
Brentjens (2008) modeled the cluster flux density as the sum of two spectral components, one due to the halo and the other due to the relic and discrete sources combined. He showed that the second term becomes dominant at frequencies above 100 MHz. Being the radio relic the dominant contributor to the flux density at high frequency, its spectrum at the same frequencies cannot be flatter than the total cluster emission spectrum. This shows qualitatively that at high frequencies the relic spectrum does not keep the 0.85 slope observed at low frequency by van Weeren et al. (2012b). In Sect. 4.5.2 we will quantify this steepening.

Discrete sources

Figure 4.3 shows the area selected for measuring the radio relic flux densities. From the high-resolution image it is possible to see which are the discrete sources included in such area: the tail of source C C_{tail}, K, J, I, G2, K2, J2, I2 and I3. To estimate the flux density from the discrete sources that needs to be subtracted from the total emission, we produced two images at 1369 MHz (VLA C configuration) and 2273 MHz (WSRT) using the same uv-range (262-15460 λ), pixel-size and restoring beam and we calculated the spectral index of the discrete sources embedded in the relic emission between these two frequencies. Moreover we measured the flux density at 10450 MHz for the different components of source C and for the sources J and I2. Where available, we combined our data with data collected from the literature and we modeled the integrated spectra of the discrete sources over the frequency range 63 - 10450 MHz. Details on the flux derivation are given below. The spectra of the sources C, K, J, I and I2, for which more than two flux density measurements were available, are plotted individually in Figs. from 4.4 to 4.8 and all together in red in Fig. 4.9. For the sources K2, J2, I3 and G2 only our flux density measurements at 1369 and 2273 MHz were available and we simply assumed straight spectra. This assumption may lead to a slight over estimate of the flux densities at both low and high frequencies (as for standard radio source synchrotron spectra we expect a flattening at low frequencies and a steepening at high frequencies). On the

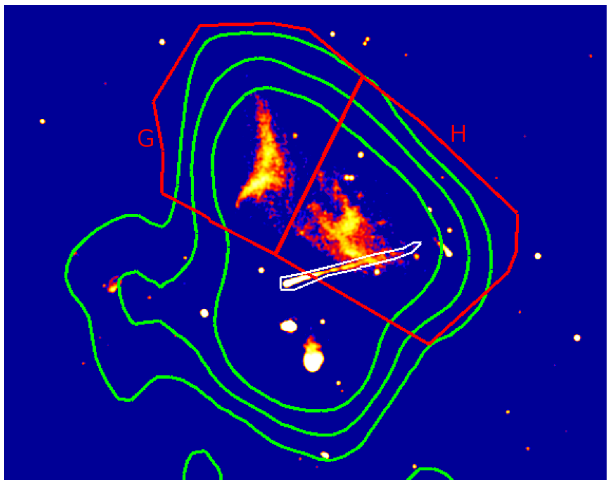

Fig. 4.3: Regions used for the spectra computation. The red region mark the region considered for the relic spectrum computation. The total region is further subdivided in regions G and H. In color scale the WSRT high resolution image with the green contours from the 2640 MHz Effelsberg image over-plotted. The white region mark the C source.

other hand, they are weak sources and their flux densities are not crucial for the relic spectrum determination. Their spectra are plotted in blue in Fig. 4.9. This figure shows the spectra of the discrete sources included in the region selected, compared to the total flux density in the region (relic+sources, black lines). The main flux density contribution among the discrete sources in the relic area come from the tail of source C, especially at lower frequencies. The source appears noticeably narrow and long at high resolution, $\sim 410''$ in total in our 2273 MHz image (see Fig. 4.3). The published flux densities in literature refer to the source as a whole. We modeled the source distinguishing between the head (long $76''$) and the tail as we are interested only on the contribution from the latter. In Figure 4.4 the spectrum over the range 63-10450 MHz is plotted for the entire source (black solid line), the head (red dashed line) and the tail (blue dotted-dashed line). As common among head-tail sources, the head is flatter than the tail and the spectrum steepens at high frequency for both components. At lower frequencies, the tail contains almost all the emission of the sources. At high frequencies the electrons in the tail are older while the head is more clearly visible.
Sources J and I2 have an inverted-spectrum. Their spectra (plotted in Figs. 4.6 and 4.8) have a convex shape at GHz frequencies, typical of inverted-spectrum sources, and are likely young radio objects.

Here we report the details of the derivation of the discrete sources flux densities. The sources position in brackets are expressed in the J2000 coordinate system. All the values are listed in Tables 4.3 and 4.4. Values in the tables in *italic* are assumed or extrapolated in this work, while values in normal font are measured values eather in this work or published in literature.

***Source C_{tail}* (17 03 28, +78 39 57)**
The peak of the emission of source C coincides with an optical galaxy with magnitude 15.3 (Bridle et al., 1979). The head-tail morphology for source C was first suggested by
Bridle & Fomalont (1976). We modeled the source distinguishing between the head (long

75″.6) and the tail as we are interested only on the contribution from the latter. At the highest frequency (10450 MHz) the head of the source is still clearly visible, while it's difficult to establish if the flux in the tail region is from the tail or from the underlying relic. The measured fluxes are $S(head)_{10450} = 2.1 \pm 0.6$ mJy and $S(tail)_{10450} = 1.9 \pm 0.7$ mJy and consequently $S(all)_{10450} = 4.0 \pm 0.0$; the last two can be considered as upper limits. Combining this values with the fluxes we measured at 2273 MHz ($S(all)_{2273} = 33.7 \pm 1.8$ mJy; $S(head)_{2273} = 17.3 \pm 0.9$ mJy ; $S(tail)_{2273} = 16.4 \pm 0.9$ mJy), we obtain spectral indices $\alpha(all)^{10450}_{2273} = 1.40 \pm 0.14$, $\alpha(head)^{10450}_{2273} = 1.40 \pm 0.19$ and $\alpha(tail)^{10450}_{2273} = 1.42 \pm 0.25$. We used these values of the spectral indices to extrapolate the fluxes of the components at 2640 and 4850 MHz. Lin et al. (2009) report a measured flux for the source C (referred to in the paper as 1706+787) of 5.06±0.60 mJy at 4.9 GHz, classifying the source as a point source. Due to the wrong classification, we believe that their observations resolve out the tail of the source and the reported flux refers to the source head only. Indeed, their reported flux is in agreement with the flux that we extrapolated for the head of the source ($S(head)_{4850} = 6.0 \pm 0.9$ mJy).
Rottgering et al. (1994) report a flux for the entire source at 327 MHz of 246 ± 20 mJy; combining this with our measurements at 1369 MHz ($S(all)_{1369} = 56.5 \pm 3.4$) we find that the spectral index for the entire source keeps the same slope as in the range 1369-2273 MHz, $\alpha(all)^{1369}_{327} = 1.03 \pm 0.07$. To separate the emission between the head and the tail we used the spectral index profile along the tail of the source C between 327 and 1447 MHz published by Rottgering et al. (1994, Fig.7 Right side). From the plot we deduced that the averaged spectral index of the head (selecting the range 0 - ∼75 ″ in the x axes) is $\alpha(head)^{1369}_{327} = 0.65 \pm 0.10$. From this we got a flux at 327 MHz for the head of 63.4 mJy and consequently a flux for the tail of $S(tail)_{327} = 246.0 - 63.4 = 182.6$ and a spectral index $\alpha(tail)^{1369}_{327} = 1.23$. We used this spectral index to calculate the fluxes at 351 MHz.
At 153 MHz van Weeren et al. (2012b) report a flux for the enire source C of $S(all)_{153} = 480 \pm 50$ mJy. The resulting spectral index is $\alpha(all)^{327}_{153} = 0.88 \pm 0.17$. From Figure 5.4 (right panel) of Intema (2009) we deduce a value for the spectral index between 153 and 325 MHz for the head of the source of $\alpha(head)^{325}_{153} = 0.50 \pm 0.10$. We used this value to calculate the flux of the head $S(head)_{153} = 92.7 \pm 10.7$ mJy. Consequently the tail has $S(tail)_{153} = 387.3 \pm 51.1$ mJy and $\alpha(tail)^{325}_{153} = 1.00$. We estrapolated the fluxes to 63 keeping costant the spectral indices of the entire source and of the head. For the tail we obtain $S(tail)_{63} = 903.5 \pm 257.0$ mJy.

***Source K* (17 02 18.4, +78 46 03.30)**
Source K was first identified by Bridle et al. (1979) and can be associated with a star-forming galaxy (Miller et al., 2003).
Rottgering et al. (1994) report a flux for the source of 7.0±1.0 mJy at 327 MHz and a flux of 3.4±0.3 mJy at 1446 MHz. The latter is in agreement within the error bars with what we measured at 1369 MHz (3.3 ± 0.2 mJy). Combining these values with what we find at 2273 MHz (1.9±0.2 mJy) we obtain a spectral index $\alpha^{1446}_{327} = 0.52 \pm 0.07$ with a steepening at high frequency $\alpha^{2273}_{1369} = 1.09 \pm 0.02$. We extrapolated the fluxes at 63 MHz and 351 MHz using α^{1446}_{327} and the fluxes at 2640 and 4850 MHz using α^{2273}_{1446}. The contribution of the source to the total flux at 10450 MHz is negligible ($\ll 1$ mJy).

***Source J* (17 01 12, +78 43 27)**
Source J was first identified by Bridle et al. (1979). Measuring the fluxes at 1369 and 2273 MHz, we found that the source has an inverted-spectrum, in agreement with what reported by

Rottgering et al. (1994). The source is indeed not visible at the 327 MHz (Rottgering et al. (1994) report an upper limit of 1 mJy), but become visible at 1369 MHz and its flux increase at 2273 MHz. At 10450 MHz the source is again at a level <1 mJy. Fitting our measurements with the flux reported by Rottgering et al. (1994) at 327 and 1447 MHz, we find a spectral index $\alpha_{327}^{2273} = -0.25 \pm 0.15$ and $\alpha_{2273}^{10450} \geq 0.35$. We used this value to extrapolate the fluxes at 2640, 4850 and 10450 MHz.

***Source I* (17 00 52.68, +78 41 23)**
Source I is a head tail source first identified by Bridle et al. (1979). The flux we measured at 1369 MHz (9.3 ± 0.8) is in agreement with what reported in literature at close frequencies ($S_{1447} = 8.2 \pm 1.8$ mJy from Rottgering et al. (1994); $S_{1400} = 10$ mJy from Owen & Ledlow (1997), included in the fit). At 2273 MHz we measure a flux of 6.8±0.4 mJy that imply a spectral index $\alpha_{1369}^{2273} = 0.69 \pm 0.10$. At higher frequencies the source has been observed with the VLA by Lin et al. (2009) (and classified as extended source). They report $S_{4900} = 2.14 \pm 0.45$ mJy and $S_{8500} = 1.25 \pm 0.36$ mJy. Fitting these values with our measurement at 2273 MHz we find a spectral index $\alpha_{2273}^{8500} = 1.38 \pm 0.12$ that we used to extrapolate the fluxes at 2640, 4850 and 10450 MHz. At 327 MHz Rottgering et al. (1994) report a flux of 8 ±1 mJy that would imply an inverted spectrum. However in their published map only the head is clearly visible, while the tail is resolved out. We treated their reported flux as a lower limit and we averaged it with the flux resulting from the extrapolation with the spectral index α_{1369}^{2273} found (25.9 mJy), that represents, on the other hand, an upper limit. The resulting averaged flux is $S_{327} = 17.0 \pm 8.9$ and consequently $\alpha_{327}^{1447} = 0.39 \pm 0.21$ mJy. We used this value to estrapolate the fluxes at 63 and 351 MHz.

***Source I2* (17 01 24, +78 41 13)**
We measure, for source I2, a flux of 1.00 ± 0.07 mJy at 1369 MHz and 1.9 ± 0.1 mJy at 2273 MHz implying an inverted spectrum. The source is indeed invisible in the 327 MHz VLA map published by Rottgering et al. (1994). At 10450 MHz we measure an upper limit <1 mJy.

Sources K2 (17 02 30, +78 45 00), J2 (17 00 51, +78, 42, 28), I3 (17 02 02, +78 40 32), G2 (17 03 22.7, +78 46 56.1)
For these sources only our measurements at 1369 MHz and 2273 MHz are available. We estrapolated the fluxes at the other frequencies assuming straight spectra.

Tab. 4.3: Properties of the source C in the A2256 field.

Component	63 MHz S (mJy)	153 MHz S (mJy)	327 MHz S (mJy)	351 MHz S (mJy)	1369 MHz S (mJy)	2273 MHz S (mJy)	2640 MHz S (mJy)	4850 MHz S (mJy)	10450 MHz S (mJy)
ALL	*1048 ± 256*	480 ± 50	246 ± 20	*228.7 ± 17.7*	56.5 ± 3.4	33.7 ± 1.8	*27.3 ± 1.4*	*11.7 ± 1.3*	< 4.0 ± 0.9
HEAD	*144.5 ± 26.9*	*92.7± 10.7*	*63.4 ± 5.5*	*60.6 ± 5.1*	25.0 ± 1.5	17.3 ± 0.9	*14.0 ± 0.8*	*6.0 ± 0.9*	2.1 ± 0.6
TAIL	*903.5 ± 257.0*	*387.3 ± 51.1*	*182.6 ±20.7*	*168.1 ± 18.4*	31.5 ± 1.9	16.4 ± 0.9	*13.3 ± 1.6*	*5.7 ±1.5*	< 1.9 ± 0.7

Component	α_{63}^{153}	α_{153}^{327}	α_{327}^{1369}	α_{1369}^{2273}	α_{2273}^{10450}
ALL	*0.88 ± 0.17*	0.88 ± 0.17	1.03 ± 0.07	1.02 ± 0.16	1.40 ± 0.14
HEAD	*0.50 ± 0.10*	*0.50 ± 0.10*	*0.65 ± 0.10*	0.72 ± 0.15	1.40 ± 0.19
TAIL	*0.95 ± 0.35*	*1.00 ± 0.22*	*1.23 ± 0.10*	1.30 ± 0.16	*1.42 ± 0.25*

Tab. 4.4: Properties of the discrete sources in the A2256 field.

Source	63 MHz S(mJy)	327 MHz S(mJy)	351 MHz S(mJy)	1369 MHz S(mJy)	1446 MHz S(mJy)	2273 MHz S(mJy)	2640 MHz S(mJy)	4850 MHz S(mJy)	4900 MHz S(mJy)	8500 MHz S(mJy)	10450 MHz S(mJy)
K	*16.3 ± 3.0*	7.0 ± 1.0	*6.7 ± 0.1*	3.3 ± 0.2	3.4 ± 0.3	1.9 ± 0.2	*1.6 ± 0.2*	*0.8 ± 0.1*	(...)	(...)	*≪1*
J	*< 0.65*	< 1	*1.0 ± 0.1*	1.2 ± 0.1	2.1 ± 0.3	1.7 ± 0.2	*< 1.5*	*< 1.2*	(...)	(...)	< 1
I	*32.2 ± 20.3*	*17.0 ± 8.9*	*16.4 ± 8.7*	9.3 ± 0.8	8.2 ± 1.8	6.8 ± 0.4	*5.5 ± 0.3*	*2.4 ± 0.3*	2.1 ± 0.5	1.2 ± 0.4	*0.8 ± 0.2*
I2	*≪1*	*≪1*	*≪1*	1.0 ± 0.07	(...)	1.9 ± 0.1	*< 1.8*	*< 1.4*	(...)	(...)	< 1
K2	*56.0 ± 27.8*	(...)	*11.3 ± 2.6*	3.2 ± 0.19	(...)	2.0 ± 0.1	*1.7 ± 0.1*	*1.0 ± 0.1*	(...)	(...)	*≪ 1*
J2	*7.9 ±6*	(...)	*3.0 ± 1.0*	1.4 ± 0.2	(...)	1.1 ± 0.2	*1.0 ± 0.1*	*0.7 ± 0.1*	(...)	(...)	*≪1*
I3	*35.2 ± 18.6*	(...)	*8.9 ± 2.1*	3.0 ± 0.2	(...)	2.0 ± 0.1	*1.8 ± 0.1*	*1.1 ± 0.1*	(...)	(...)	*≪ 1*
G2	*23.9 ± 13.7*	(...)	*5.5 ± 1.4*	1.7 ± 0.1	(...)	1.1 ± 0.1	*1.0 ± 0.1*	*0.6 ±0.1*	(...)	(...)	*≪1*

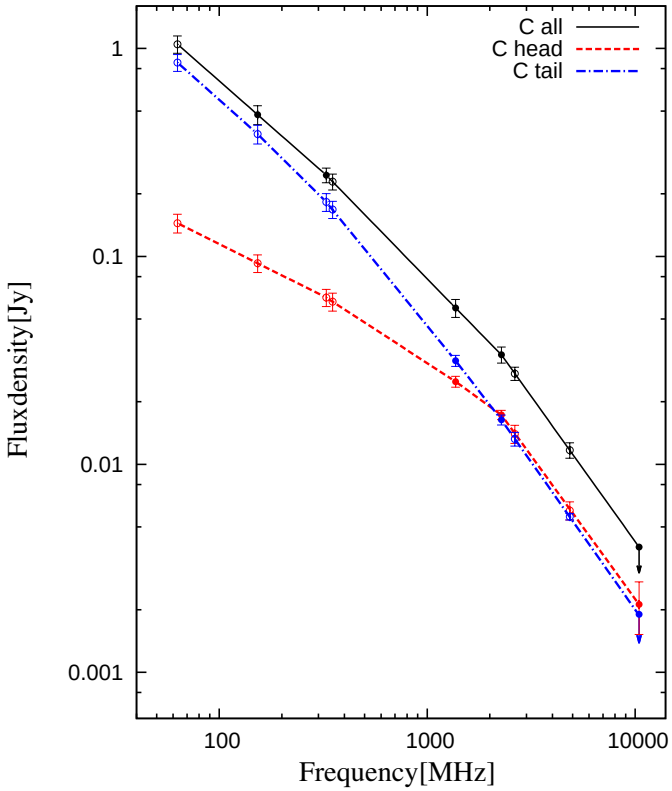

Fig. 4.4: C source spectrum. Filled circles are measured flux densities while open circles are extrapolated flux densities. The black solid line is the spectrum of the entire source; the red dashed line is the source's head spectrum; the blue dotted-dashed line is the spectrum of the tail. See text for more details.

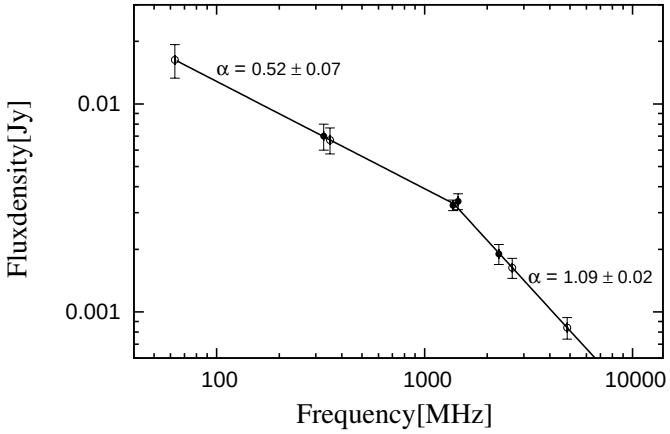

Fig. 4.5: K source spectrum. Filled circles are measured flux densities while open circles are extrapolated flux densities.

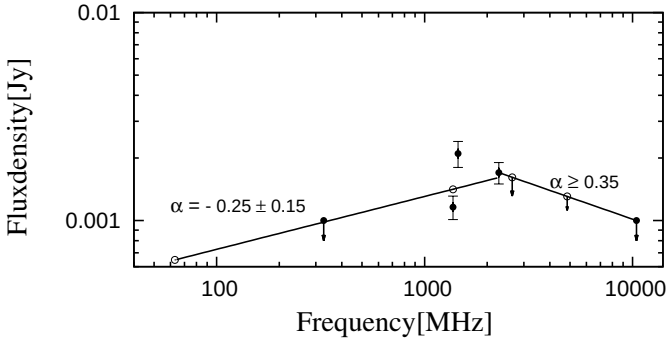

Fig. 4.6: J source spectrum. Filled circles are measured flux densities while open circles are extrapolated flux densities.

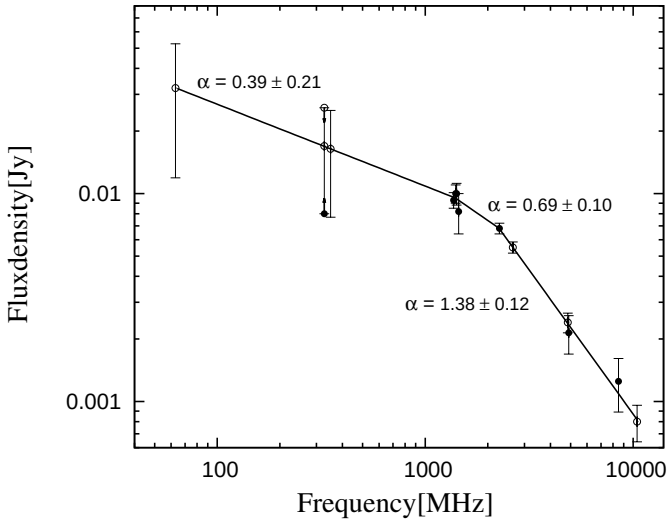

Fig. 4.7: Source I spectrum. Filled circles are measured flux densities while open circles are extrapolated flux densities.

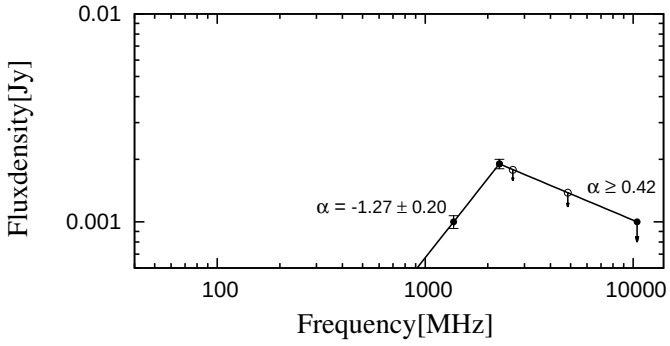

Fig. 4.8: Source I2 spectrum. Filled circles are measured flux densities while open circles are extrapolated flux densities.

Radio relic spectrum

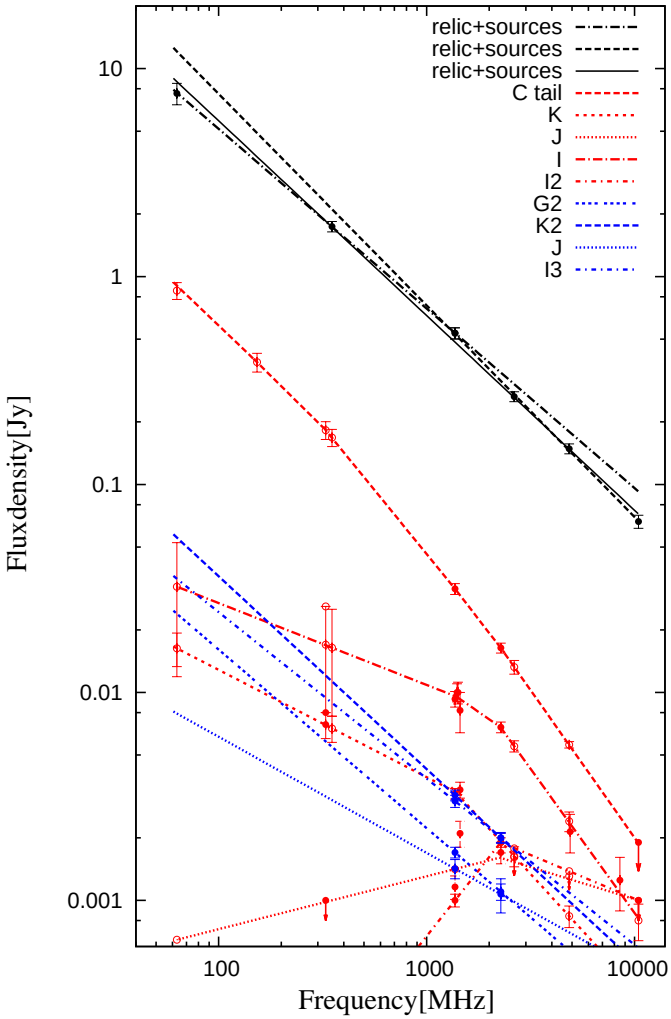

Fig. 4.9: Spectra of the different components in the relic region shown in Fig. 4.3. In black we show the flux densities and spectra of the emission from the entire region (relic+sources). The dashed and dot-dashed lines represent a the double power law fit to the data; the solid line is a single power law fit. In red and blue we show the spectra of the discrete sources included in the region. Red spectra are plotted individually in Figs. from 4.4 to 4.8. Blue spectra are straight power-law fits to the measured flux densities at 1369 and 2273 MHz. See text for more details.

To avoid that resolution effects at different frequencies may alter the determination of the relic integrated spectrum, we convolved all the images used for the flux densities computation to the same resolution of 4.′4× 4.′4. At such low resolution, it is not easy to identify the region where to measure the relic flux density. We adopted the following strategy: we first computed the relic flux density from the 4850 MHz image at full resolution, where it is easier to separate the relic emission from the complex A+B emission. We then choose the relic region in the 4850 MHz image convolved to the resolution of $4.4' \times 4.'4$, matching the flux density measured at full resolution at the same frequency. The selected area is shown in Fig. 4.3. The region is

further divided into two regions of enhanced radio brightness (regions G and H) discussed in the next section. As discussed in the previous section, this region include the radio relic and sources C_{tail}, K, J, I, G2, K2, J2, I2 and I3.
We first considered the total emission from the region. Although the flux density measurements of the relic+sources in the range 63-10450 MHz can be fitted with a single power law with $\alpha_{63}^{10450} = 0.93 \pm 0.02$ (black solid line in Fig. 4.9), hints of a steepening at frequencies > 1369 MHz are present. A separate fit of the spectra between 63 and 1369 MHz and between 1369 and 10450 MHz shows indeed that these two frequency ranges are best represented by two different power laws, with $\alpha_{63}^{1369} = 0.863 \pm 0.003$ (dot-dashed black line in Fig. 4.9) and $\alpha_{1369}^{10450} = 1.02 \pm 0.02$ (dashed black line in Fig. 4.9). All the fits are plotted over the entire range 63-10450 MHz to highlight differences. Since the relic is the major contributor in the region both at low and high frequency, this suggests that a steepening might be present in its spectrum as well. Moreover the relic spectrum between 63 and 1369 MHz must be $\alpha(relic)_{63}^{1369} \leq 0.863 \pm 0.003$ as it cannot be steeper than the relic+sources spectrum. Similarly it must be $\alpha(relic)_{1369}^{10450} \geq 1.02 \pm 0.02$ as it cannot be flatter than the relic+sources spectrum. Indeed, after discrete sources subtraction we find that, although the relic spectrum between 63 and 10450 MHz is not inconsistent with a single power law with $\alpha(relic)_{63}^{10450} = 0.92 \pm 0.02$ (black solid line in Fig. 4.10b), it is best represented by two different power laws, with $\alpha(relic)_{63}^{1369} = 0.8488 \pm 0.0003$ (dot-dashed blue line in Fig. 4.10b) and $\alpha(relic)_{1369}^{10450} = 1.00 \pm 0.02$ (dashed red line in Fig. 4.10b). The measured relic flux densities (before and after discrete sources subtraction) are summarized in Table 4.6. The flux densities measured at 63 MHz, 351 MHz and 1369 MHz are in agreement within the error bars with the already published flux densities at the same frequencies. The low frequency spectral index is in agreement with what was found by van Weeren et al. (2012b).
Clarke & Ensslin (2006) report a relic mean spectral index between 1369 MHz and 1703 MHz of 1.2. However, this value has a big uncertainty (not quoted by author) since it is derived as the mean value from the spectral index image between two very close frequencies. We cannot therefore exclude it is in agreement with our value.

Regions G and H

Our high-resolution image shows that the relic can be divided into two separate parts: regions G and H in Fig. 4.3. The cases of double relics in the same cluster are getting more and more common since the first discovery of two almost symmetric relics located on opposite sides in A3667. Since then, several other double relics systems have been found (see Feretti et al. 2012). We have investigated the possibility that the two different parts have different properties fitting the spectra in the frequency range 351-10450 MHz, separately. After discrete sources subtraction, the flux densities of region G can be fitted with a single power-law with a spectral index of $\alpha(G)_{351}^{10450} = 0.97 \pm 0.04$ (black solid line in Fig. 4.10c). For homogeneity with the radio relic analysis, we performed a separate fit of the spectra between 351 and 1369 MHz and between 1369 and 10450 MHz. We find $\alpha(G)_{351}^{1369} = 0.85$ (dot-dashed blue line in Fig. 4.10c) and $\alpha(G)_{1369}^{10450} = 1.05 \pm 0.05$ (dashed red line in Fig. 4.10c).
For the H region the flux densities can be modeled with a single power-law with spectral index $\alpha(H)_{351}^{10450} = 0.92 \pm 0.02$ (black solid line in Fig. 4.10d) or with a double law with the same slope as the G region at low frequency $\alpha(H)_{351}^{1369} = 0.85$ (dot-dashed blue line in Fig. 4.10d) and a bit flatter spectra respect the G region at high frequency $\alpha(H)_{1369}^{10450} = 0.95 \pm 0.03$ (dashed

red line in Fig. 4.10d).
The measured flux densities before and after discrete sources subtraction are listed in Tables 4.7 and 4.8, while the spectra are plotted in Figs. 4.10c and 4.10d.

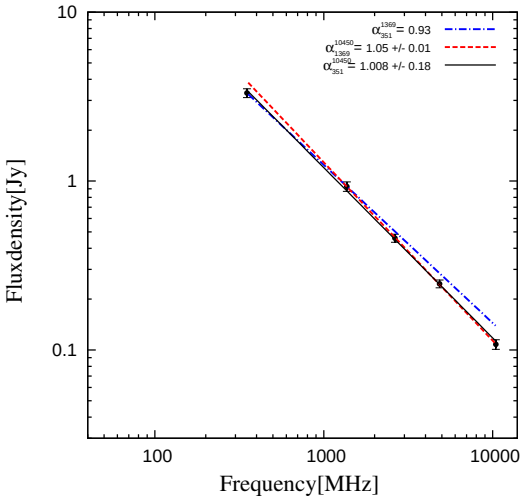

(a) Total cluster integrated spectrum.

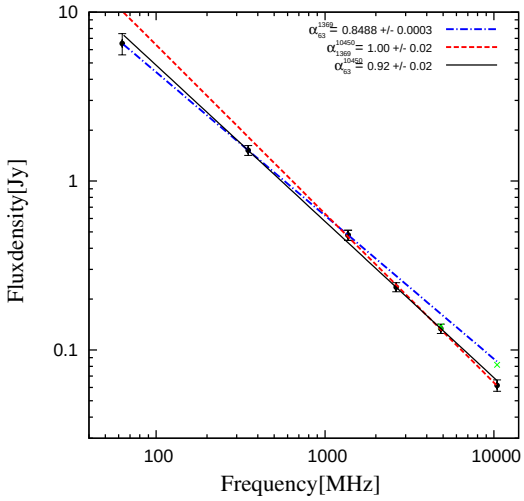

(b) Radio relic integrated spectrum.

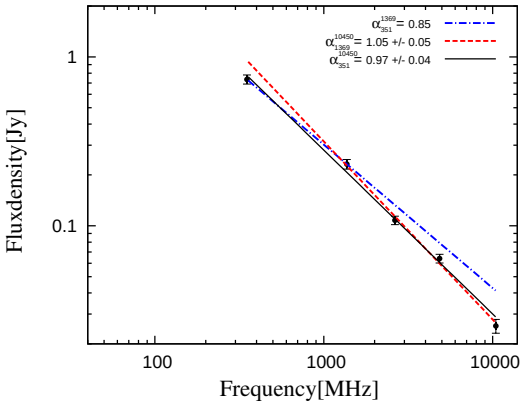

(c) G region integrated spectrum.

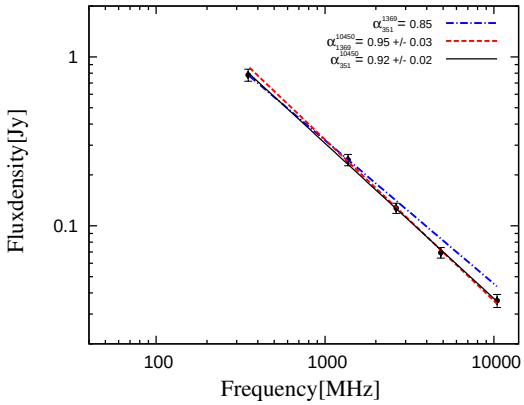

(d) H region integrated spectrum.

Fig. 4.10: In all the panels the red dashed and blue dot-dashed lines are a double power law fit to the data while the solid black line is the single power law fit. In panel (b) the green crosses are the upper limits to the radio relic flux taking into account the SZ effect. See text for more details.

Tab. 4.5: Total cluster flux densities.

ν (MHz)	S(mJy)
351	3320.0 ± 200.0
1369	928.6 ± 57.0
2640	459.0 ± 24.8
4850	246.3 ± 13.3
10450	107.8 ± 7.5

Tab. 4.6: Radio relic flux densities.

ν (MHz)	S(mJy) Before subtraction	S(mJy) After subtraction
63	7600.0 ± 900.0	6520.0 ± 940.0
351	1740.0 ± 100.0	1520.0 ± 100.0
1369	534.3 ± 33.1	478.5 ± 33.2
2640	264.6 ± 14.4	235.4 ± 14.5
4850	148.6 ± 8.2	133.7 ± 8.5
10450	66.4 ± 4.8	61.7 ± 4.8

Tab. 4.7: Region G flux densities.

ν (MHz)	S(mJy) Before subtraction	S(mJy) After subtraction
351	741.2 ± 45.8	735.7 ± 45.8
1369	233.3 ± 15.1	231.6 ± 15.1
2640	108.8 ± 6.2	107.8 ± 6.2
4850	64.6 ± 3.8	64.0 ± 3.8
10450	25.5 ± 2.4	25.5 ± 2.4

Tab. 4.8: Region H flux densities.

ν (MHz)	S(mJy) Before subtraction	S(mJy) After subtraction
351	996.8 ± 60.9	781.3 ± 64.3
1369	299.6 ± 19.0	245.8 ± 19.1
2640	155.5 ± 8.6	127.2 ± 8.8
4850	83.7 ± 4.8	69.4 ± 5.0
10450	40.7 ± 3.1	36.0 ± 3.2

Tab. 4.9: Observed synchrotron spectral indices of the different components.

	Single power law fit	Double power law fit	
	α_{63}^{10450}	α_{63}^{1369}	α_{1369}^{10450}
Total relic region	0.93 ± 0.02	0.863 ± 0.003	1.02 ± 0.02
Radio relic	0.92 ± 0.02	0.8488 ± 0.0003	1.00 ± 0.02
	α_{351}^{10450}	α_{351}^{1369}	α_{1369}^{10450}
Total cluster	1.01 ± 0.02		
Region G	0.97 ± 0.04	0.85	1.05 ± 0.05
Region H	0.92 ± 0.02	0.85	0.95 ± 0.03

4.6 X-ray analysis and results

4.6.1 ICM temperature

In the course of a merger, a significant portion of the energy involved is dissipated by shocks and turbulence leading eventually to the heating of the ICM gas. As mentioned in the Introduction, in the test particle regime of DSA theory the shock structure is determined by the canonical shock jump conditions (Rankine-Hugoniot). Applying these conditions, assuming the ratio of specific heats as 5/3, the expected ratio between the post-shock and pre-shock temperatures, respectively T_2 and T_1, is related to the shock Mach number through the following

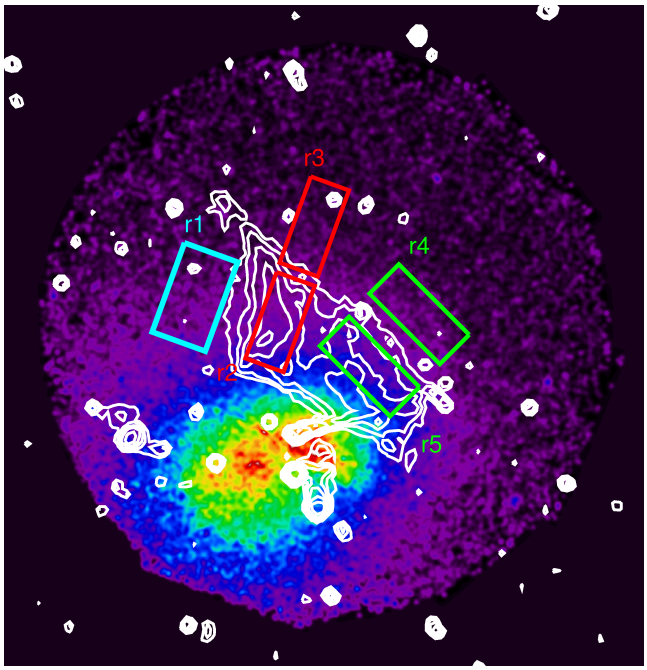

Fig. 4.11: Regions used for the ICM temperature extraction. Colors show the XMM-Newton X-ray image, while the contours show the radio emission at a lower resolution respect to Fig. 4.1.

relation:

$$\frac{T_2}{T_1} = \frac{5M^4 + 14M^2 - 3}{16M^2}. \tag{4.6}$$

We extracted the ICM temperature in different regions across the radio relic corresponding to the rectangular areas shown in Fig. 5.5. The observed spectra were assumed to consist of thin thermal plasma emission from the ICM, plus the total background contamination described in Sec. 4.4. The emission from the ICM was modeled with an additional absorbed thermal component in the total model (ICM+background). For the Suzaku analysis, to generate the auxiliary response files (ARF), we used an image constructed using a β-model ($\beta = 0.816$, $r_c = 5.64'$ from Markevitch & Vikhlinin, 1997) as input for the *xissimarfgen*. For XMM-Newton data, we fitted the spectra in the 0.5-8 keV energy range, excluding the 1.4-1.6 keV band due to the strong contamination from the Al line in all three detectors. Because of the low number of counts in the XMM-Newton spectra of region r1, r2 and r3, we kept the metallicity values in the fit frozen to the value obtained with the Suzaku analysis, which are better constrained [9]. Temperatures and normalizations of the thermal components were allowed to vary in the fit.

We observe a temperature drop across the G region of the radio relic, with the temperature jumping from $8.45^{+0.43}_{-0.33}$ keV in the region r2 (on the relic) to $4.95^{+0.48}_{-0.39}$ keV in the region r3 (outside the outer edge of the relic). XMM-Newton measurements in the same regions provide consistent temperatures although with bigger errors. This is in agreement with Sun et al. (2002) that found a hot region ($\sim$ 9 KeV) in positional coincidence with the G lobe of the

[9] (Z(r1)= 0.27 ± 0.05 $Z_\odot$, Z(r2)= 0.12 ± 0.04 $Z_\odot$, Z(r3)= 0.19 ± 0.12 $Z_\odot$).

Tab. 4.10: ICM temperatures kT(keV).

Region	Suzaku data	XMM-Newton data
r1	$6.53^{+0.28}_{-0.23}$	$6.70^{+1.04}_{-1.07}$
r2 (on G region)	$8.45^{+0.43}_{0.33}$	$8.29^{+1.16}_{-0.88}$
r3	$4.95^{+0.48}_{-0.39}$	$4.97^{+2.11}_{-1.83}$
r4	(...)	$5.89^{+1.06}_{-1.13}$
r5 (on H region)	(...)	$5.89^{+0.95}_{-0.70}$

radio relic. Radio relics are usually associated to *outgoing merger shocks* that travels from the core of a merging event outwardly towards the periphery of the clusters. If we apply such scenario to A 2256, connecting the radio relic emission to a shock front propagating outwardly in the north-western direction across the G region of the radio relic, we can consider r2 as the post-shock region and r3 as the pre-shock region. In this case we have a temperature ratio T_2/T_1=1.7. It is important to notice that this estimate is impacted by the angle of the shock front to the line of sight. If the shock is not in the plane of the sky, as it is likely the case for A 2256, projected mixing of shocked hot gas with cool gas will reduce the temperature of the shocked gas and increase the temperature of the cool gas, basically dropping the temperature ratio.
Regions r5 and r4, respectively on the H region of the relic and outside the outer edge, show almost equal temperatures $T(r5)=5.89^{+0.95}_{-0.70}$ and $T(r4)=5.89^{+1.06}_{-1.13}$ in the XMM-Newton images, although with big uncertainties. Unfortunately, region r4 is out of Suzaku field-of-view and cannot be checked. This is anyway in agreement with previous studies conducted by Sun et al. (2002) and Bourdin & Mazzotta (2008) that showed that this region is cold due to the presence of a cool sub-cluster at an early stage merging with the main cluster, approaching from somewhere west. Projection effects, affecting in particular region r5, can thus be responsible for the non detection of a temperature jump across the H region of the relic.
The measured temperatures in the different regions are summarized in Table 4.10 for both Suzaku and XMM-Newton data.

4.7 Is the Sunyaev-Zeldovich effect important?

The thermal Sunyaev-Zeldovich (SZ) effect (Sunyaev & Zeldovich, 1970) consists in the inverse Compton scattering to higher energies of the photons of the Cosmic Microwave Background (CMB) that interact with the hot electrons in the ICM of galaxy clusters. The effect depends on the pressure produced by the plasma along the line of sight and is parametrized through the *Comptonisation parameter y* (see Carlstrom et al., 2002, for a review). The SZ effect produces a modification of the CMB blackbody spectrum, creating a negative flux bowl on the scale of the cluster, at GHz frequencies. This might lead to two sources of errors in our flux densities measurements at high frequencies. The first derives from a wrong setting of the zero-level in the single dish images. The zero-level in single dish observations is usually set assuming the absence of sources at the map edges, setting the intensity level to zero there,

and interpolating linearly between the two opposite edges of the map. If the SZ decrement is important in the regions where zero flux was assumed (determining a negative flux in those areas), this results in a wrong setting of the zero-level of the entire map. This lead to a lower estimation of the flux densities integrated over any region in the map. In addition to this, there is the SZ decrement specific to the area used to compute the relic flux densities.
We used the integrated Comptonisation parameter Y_{SZ} as measured by Planck
(Planck Collaboration et al., 2011b) and the universal pressure profile shape as derived by Arnaud et al. (2010), to derive the predicted pressure and Comptonisation parameter profiles for A 2256 (see Planck Collaboration et al., 2013a). We used the derived y parameter radial profile to estimate the importance of the SZ decrement in different regions at the edges of the original Effelsberg 10450 MHz image, to check the zero-level setting. Integrating on areas free of sources at the map edges with angular diameter of $4'$, we find values of -0.1 / -0.3 mJy for the CMB flux decrement. We conclude that the effect of the SZ decrement on the zero-level setting of the 10450 MHz image is negligible. As the SZ effect increase increasing the frequency, we conclude that it does not affect the zero-level setting of the 2640 and 4850 MHz Effelsberg images.
Estimating the second effect is more complicated, especially if we believe that the relic in A 2256 is powered by a shock. In case of a shock, in fact, a sharp increase of the pressure at the shock front is expected, causing a local increase of the SZ decrement. An exact estimate of the amount of the effect requires a detailed knowledge of the shock geometry and orientation and of the pressure changes across the relic width. We estimate here an upper limit for the SZ effect on our high frequencies flux estimates. The radio relic fluxes have been calculated in an approximatively rectangular area of $\sim 18' \times 9'$, whose major axis is located at a projected distance of $\sim 7.2'$ ($\sim$ 500 kpc) from the cluster X-ray main peak. If we assume that we observe the shock in the plane of the sky, we can consider a physical distance of the relic from the cluster center of$\sim$ 500 kpc. This is a lower limit to the real distance relic-cluster center and maximize the SZ effect, that is higher in the denser central regions. We can derive a qualitative estimation of the possible shock pressure jump from the observed ICM temperature ratio across the relic. Inverting eq. 4.6 we obtain a Mach number $\sim$ 1.7. As discussed, this number can have been reduced by projection effects. We assume for the calculations a Mach number $M = 2$. Applying the Rankine-Hugoniot jump conditions, the ratio between the post-shock P_2 and pre-shock P_1 pressures, given the Mach number M, is P_2/P_1 $\sim$4. We estimated the SZ flux decrement in the area used for the radio relic flux measurements using eq. 3 from Carlstrom et al. (2002) and assuming a value $y_{POST} = 4y_{PRE}$ (where y_{PRE} was extracted from the y-profile at a corresponding distance of $7.2'$) constant over all the area. This assumptions bring to an over estimation of the SZ effect because the real width of the relic is expected to be much lower than the projected one, and the increased pressure is expected to decrease again moving away from the shock front in the downstream region. With these assumptions, we obtain SZ flux decrements of $\sim$ -20 mJy, $\sim$ -4.3 mJy, $\sim$ -0.3 mJy respectively at 10450 MHz, 4850 MHz and 2640 MHz. We stress that this numbers are upper limits for the SZ decrement. Assuming, for example, the physical distance of $\sim$700 Kpc from the center deduced by Enßlin et al. (1998) based on polarization properties, the effect at 10450 MHz reduces to $\sim$ -11 mJy.
We plotted in Fig. 4.10b (green crosses) the upper limits of the relic flux at 4850 and 10450 MHz, adding the upper limit SZ flux decrements (in absolute value) to the measured fluxes. The effect on the integrated radio spectrum is to make it even flatter.

4.8 Discussion

Independent of the acceleration mechanism, we can infer the range of energies (in terms of the Lorentz factor γ_e) of the emitting electrons in the relic region from the integrated spectrum via (Kang et al., 2012):

$$\gamma_e \approx 1.26 \times 10^4 \left(\frac{\nu_{obs}}{1GHz}\right)^{1/2} \left(\frac{B}{5\mu G}\right)^{-1/2} (1+z)^{1/2}. \quad (4.7)$$

The relic in A 2256 has been observed from very low frequencies ($\sim$ 20 MHz with LOFAR, van Weeren et al., 2012b, flux densities not published) up to very high frequencies ($\sim$ 10 GHz with Effelsberg). This implies, via Eq. 4.7, that the emitting electrons have energies between, at least, $\gamma_{e,min} \sim 2 \cdot 10^3 - 4 \cdot 10^3$ and $\gamma_{e,max} \sim 4 \cdot 10^4 - 9 \cdot 10^4$. For both $\gamma_{e,min}$ and $\gamma_{e,max}$, assuming magnetic fields between $B = 5 - 1\mu$G, respectively. The radiative lifetime for the less energetic electrons is $t_{rad}(\gamma_{e,min}) \sim 0.32 - 0.43$ Gyr (for $B = 5 - 1\mu$G respectively) and $t_{rad}(\gamma_{e,max}) \sim 0.016 - 0.019$ Gyr for the more energetic ones. Probably, whatever it is the acceleration mechanism, it is still at work since the particles emitting at 10 GHz lose rapidly their energy and the relic would become invisible at this frequency without a constant supply of new particles, soon after the end of the acceleration.
We have formulated five different possible scenarios to explain the properties of the relic, and we will discuss here the pros and cons for each of them.

4.8.1 Non-stationary DSA

Together, the regions G and H of the relic in A 2256 reach a length of $\sim$ 1 Mpc. To date the most plausible scenario to explain such *giant* radio relics invoke diffusive shock acceleration (DSA) during cluster mergers. Assuming that the shock is continuously accelerating particles following the same power law for a time exceeding the electrons cooling time, we expect a volume-integrated spectrum that is a single power law with spectral index $\alpha_{obs} = \alpha_{inj} + 0.5$ (stationarity for the spectrum). As shown in Sect. 4.5.2, the relic in A 2256 shows a peculiar broken power law that is difficult to explain in terms of test-particle DSA of a single population of electrons. At low frequencies (between 63 and 1369 MHz), we confirm the spectral index $\alpha \sim 0.85$ previously found by van Weeren et al. (2012b). This spectrum is too flat to be considered the stationary spectrum as it would imply an injection spectral index flatter than the flattest allowed by test-particle DSA theory (see Introduction). One solution is that, at low frequencies, we observe the *injection* synchrotron spectrum since a stationary spectrum is only attained if the time for energy losses is shorter than the age of the shock at *all* energies. Kang (2011) shows that the downstream integrated electron spectrum at a quasi-parallel shock is a broken power law which steepens from $E^{-\delta_{inj}}$ to $E^{-(\delta_{inj}+1)}$ above $E > E_{br}(t)$, with an exponential cutoff at energies higher than E_{eq}. E_{eq} is the maximum electron energy injected reached when the equilibrium between energy gains and losses is achieved and reflects the strength of the shock. E_{br} describes more properly the electron aging and can be used to estimate the shock age. As a consequence the volume-integrated synchrotron spectrum has a spectral break and

an high-frequency cut-off described by:

$$S(\nu) \propto \begin{cases} \nu^{-\alpha_{inj}} & \text{at } \nu < \nu_{br}(t) \\ \nu^{-(\alpha_{inj}+0.5)} & \text{at } \nu_{br}(t) < \nu < \nu_{eq} \\ exp(-\nu/\nu_{eq}) & \text{at } \nu > \nu_{eq} \end{cases}$$

If we assume that the shock started to accelerate particles recently, we would be able to catch the break frequency still in the observable frequency range. In the case of A 2256, we should assume ν_{br}=1.4 GHz, that implies that the relic age is $t_{rad}(\gamma_{e,1.4GHz}) \sim 0.04 - 0.05$ Gyr.
An injection spectral index ~ 0.85 would be also in agreement with what reported by Clarke et al. (2011). They observe a spectral index of 0.85 at the outer edge of the relic, steepening moving across the source towards the inner edge. This suggests that the relic is produced by a shock that is moving outwardly and is now located at the outer edge of the relic where it is accelerating particle according to the injection spectrum. However, the spectral index of the integrated synchrotron emission above the break frequency should be in this case $\alpha_{obs} = 1.35$, while we observe a flatter spectrum with slope $\sim$1.
Moreover, to produce an injection spectral index $\alpha_{inj} = 0.85$, we need a shock with Mach number given by (combining eqs. 4.1 and 4.3):

$$M = \sqrt{\frac{2\alpha_{inj} + 3}{2\alpha_{inj} - 1}} = 2.6. \tag{4.8}$$

Such a shock would produce a temperature ratio between the shocked gas and the thermal gas of ~ 3 (from eq.4.6). However, the lower temperature ratio measured with Suzaku and XMM-Newton data suggests the presence, if any, of a weaker shock.
The observed radio spectrum of the relic in A 2256 may be reconciled with test-particle DSA invoking a more complex situation in which the electrons emitting in the relic region belong to different populations with different history and aging. This might be due to a modification of the shock properties while propagating in the ICM and a consequent modification of the electron injection power law.

4.8.2 CRe modified DSA

The relic spectrum can be fitted also with a single power law between 63 MHz and 10450 MHz with a spectral index $\alpha_{63}^{10450} = 0.92 \pm 0.02$. The spectral index would be even flatter if the SZ decrement approaches our upper limits estimate. It would be quite unlikely that we are observing the injection spectrum because this would imply that $\nu_{br} > 10$ GHz that is equivalent to say that the relic brightned more recently than 0.016-0.019 Gyr. So, if what we observe is the stationary spectrum, it would again imply an injection spectral index flatter than the flattest allowed by test particle DSA.
A solution is to take into account the shock modification induced by the dynamical reaction of the accelerated particles. The condition on the flattest possible injection index is due to the test-particle approach to DSA. In CR modified shocks, the compression ratio can be higher and the injection synchrotron spectra can be flatter than 0.5 (e.g. Blasi, 2010).

4.8.3 DSA of pre-accelerated CRe

Kang & Ryu (2011) and Kang et al. (2012) argue that the existence of pre-accelerated CRs electrons might alleviate the problem of inefficient injection at weak shocks. They have suggested that the hot ICM first goes through a series of accretion shocks of high Mach numbers before getting subjected to weaker cluster merger shock, and that hence the ICM should contain some pre-existing CR population. Moreover, pre-existing non thermal particles might have been produced via turbulent re-acceleration (Brunetti & Lazarian, 2007, 2011) or through $p - p$ collisions of CR protons with thermal protons of the ICM (Miniati et al., 2001a). This pre-existing CR population may contain many different electron populations and may be described by a cumulative power law $f \propto E^{-\delta_{pre}}$. They show that if the spectrum of the pre-existing population is steeper than the spectrum that could be produced by the shock ($\delta_{pre} > \delta_{inj}$), then the re-accelerated CR spectrum gets flattened to $E^{-\delta_{inj}}$ by DSA. In the opposite case ($\delta_{pre} < \delta_{inj}$), the re-accelerated CR spectrum is simply amplified by the factor of $\delta_{inj}/(\delta_{inj}-\delta_{pre})$ and retains the same slope as the slope of pre-existing CRs (Kang & Ryu, 2011; Kang et al., 2012). Applying this to the radio relic in A 2256, we have to assume that the spectrum we observe has the same spectral slope as the one of the pre-existing population. In this case the shock we observe would be responsible only for the amplification of the particle spectrum. However, it is difficult to explain how the radio spectrum has kept such flat slope over a wide range of frequencies in spite of electron energy losses.

4.8.4 Adiabatic compression

The relic in A 2256 appears to be very filamentary. Enßlin & Brüggen (2002) presented detailed three-dimensional simulations of the passage of radio plasma cocoons filled with turbulent magnetic field through shock waves. They showed that, on contact with the shock wave, the radio cocoons are first compressed and finally torn into filamentary structures. Moreover, van Weeren et al. (2012b) proposed a viewing angle of about 30° from edge-on and a a true distance of ~0.5 Mpc from the cluster center for the radio relic. Both these two characteristics favor of a scenario where the relic is the result of re-energization of fossil plasma by adiabatic compression. On the other hand, the large size of the relic and the flat spectrum at high frequency make this scenario unlikely.

4.8.5 Independent relics

Finally, regions G and H might be another example of two independent relics, for example two radio Phoenices produced by the same shock or by different shocks front. We have checked for different properties of the two regions calculating their individual radio integrated spectra. Although the integrated spectrum of region G appears slightly steeper than that of region H, the two are consistently similar within the error bars and too flat to be reconciled with the observed shock. The absence of a pronounced steepening in the individual spectra also rules out the double phoenics origin.

The above discussion leads to the conclusion that test-particle DSA, as well as the adiabatic compression model, run into problems in explaining the observed radio and X-ray properties of the radio relic in A 2256.

Detailed spatial analysis based on polarization properties and spectral index maps (Trasatti et al. in prep.) will help in constrain the relic geometry and possibly its origin. Accurate profiles of the ICM surface brightness and temperature from X-ray observations, as well as pressure profiles from deep pointed SZ observations are needed to finally establish the presence of a shock front in the location of the radio relic in A 2256.

4.9 Conclusions

We have presented a radio and X-ray analysis of the radio relic in the cluster A 2256. The main points of this study can be summarized as follows:

1. We presented new high-frequency observations of A 2256 performed at 2273 MHz with the WSRT and at 2640 and 4850 MHz with the Effelsberg-100m telescope. The high resolution of the WSRT observations highlighted that the relic can be divided in two regions of enhanced surface brightness (regions G and H) connected by a bridge of lower brightness emission.

2. Combining our new observations with images available at other frequencies, we constrained the radio integrated spectrum of the radio relic in A 2256 over the widest frequency range collected so far for this kind of objects (63 -10450 MHz). We find that, although the relic spectrum between 63 and 10450 MHz is not inconsistent with a single power law with $\alpha(relic)_{63}^{10450} = 0.92 \pm 0.02$, a separate fit of the spectra between 63 and 1369 MHz and between 1369 and 10450 MHz shows that these two frequency ranges are best represented by two different power laws, with $\alpha(relic)_{63}^{1369} = 0.8488 \pm 0.0003$ and $\alpha(relic)_{1369}^{10450} = 1.00 \pm 0.02$. This broken power-law is difficult to explain in terms of stationary or non-stationary DSA of a single population of electrons.

3. We have investigated the possibility that the G and H regions have different properties in the frequency range 351-10450 MHz. We find that the singular spectra of regions G and H show a similar flat trend respect the total relic with $\alpha(G)_{351}^{10450} = 0.97 \pm 0.04$ and $\alpha(H)_{351}^{10450} = 0.92 \pm 0.02$.

4. We used Suzaku and XMM-Newton X-ray observations to measure the ICM temperature in the regions across the radio relic emission. We find a temperature ratio $T_2/T_1 \sim 1.7$ across the G region of the radio relic supporting the presence, if any, of a weak shock. No temperature jumps are observed across the H region of the relic, probably due to the projection in this area of a colder sub-cluster approaching the main cluster from the west.

5. The flat integrated radio spectrum of the entire relic, as well as of the regions G and H separately, and the low ICM temperature ratio cannot be explained together in the framework of test-particle DSA.

6. The absence of a pronounced steepening in the integrated radio spectrum of the relic as well as of the regions G and H separately, rule out a phoenices origin for the relic/s.

Chapter 5

Spectral and polarization study of the radio relic in Abell 2256*

5.1 Introduction

The diffuse synchrotron emission from radio relics and halos is a direct evidence of the presence of magnetic fields and relativistic particles in galaxy clusters. Unlike radio halos, relics show a high degree of polarization (up to 45-50 %) and ordered magnetic field vectors. Theoretical studies have shown that an integral part of DSA (Sect. 2.3.2) in strong shocks is magnetic-field compression, amplification and alignment with the shock front (Lucek & Bell, 2000; Bell, 2004). Recent simulations by Iapichino & Brüggen (2012) predict strong magnetic fields aligned with the shock surface of the order of 6 μG at 0.5 R_{vir}, which are in agreement with observations (e.g. Bonafede et al., 2009; van Weeren et al., 2010).
Synchrotron spectral indices away from the shock location steepen with time as a result of energy losses. For an edge-on relic produced by a shock moving in the plane of the sky, where no projection effects occur, a clear gradient in the spectral-index distribution across the source is expected, with the flattest values marking the position of the shock front where the particles are freshly accelerated and the steepening showing the radiative losses as the electrons are advected away from the shock.
The relic with the best radio evidence for DSA found to date has been observed in the northern outskirts of the merging galaxy cluster CIZA J2242.8+5301 (Figs. 2.2 and 2.7 van Weeren et al., 2010). This relic is polarized at a 50-60% level, the magnetic field is aligned with the major axis and the spectral-index gradient across its width is clearly observed. All these relic properties arise naturally for a head-on binary merger between two clusters of roughly equal masses in the plane of the sky, with the shock waves seen edge-on (van Weeren et al., 2011).
In case of DSA alignment of the polarization vectors and spectral distribution across the extent of radio relics can therefore be connected to the geometry of the shock passage.

5.2 The radio relic in Abell 2256

The galaxy cluster Abell 2256 (also discussed in Chap. 4) is a well known merging system hosting both a radio halo and a radio relic. So far, it is thought to consist of at least

*Trasatti, Lovisari, Klein et al. (in prep.)

three merging systems, based on the observed velocity dispersion of the galaxies in the cluster (Berrington et al., 2002; Miller et al., 2003) and X-ray observations of the ICM (Sun et al., 2002). The latter paper presented Chandra observations of the cluster that revealed the presence of three peaks in the X-ray emission: the main cluster, a colder sub-cluster located in the west, and a third smaller structure (called the shoulder) located 2′ east of the peak of the main cluster.
Clarke & Ensslin (2006) proposed two different merger scenarios to explain the radio features observed in this cluster: a current merger in a very early stage creating the radio relic, with the radio halo being the remnant from an older merger event, or an advanced merger of the primary cluster and the western sub-cluster in which the merger shock has already passed the core of the primary to create both the diffuse halo and relic emission, favoring the latter. They also conducted one of the few previous studies of the polarization properties of the cluster. They found that the entire radio relic shows a high level of polarization, with an average of 20% at 1.4 GHz. They also show the displacement of the magnetic field vectors in the region of the relic emission, although the Faraday correction for the Galactic contribution at the position of the cluster was made with an old value of the galactic rotation measure (RM = -4±37 rad·m^{-2}), based on an average of seven sources within 15° in the RM catalog of Simard-Normandin et al. (1981). They moreover suggest, based on a Faraday RM map, that the relic is on the near side of the cluster and does not experience significant Faraday rotation from the ICM.
Kale & Dwarakanath (2010) conducted a spectral study across the diffuse emission in A2256 and found an occurrence of flat spectral indices in the region of the radio relic ($\alpha_{150}^{350} \sim 0.7-1.1$ and $\alpha_{350}^{1369} \sim 0.7-0.9$). Similar results have been presented by Brentjens (2008).
We showed in Chap. 4 that the integrated spectrum of the A2256 radio relic keeps this flat behavior up to ∼ 10 GHz. In this chapter we present a detailed spatial study of the spectral and polarization properties of the diffuse emission. In Sect. 5.3 we recall the observations and present the main steps of the polarization calibration and imaging. Polarization and spectral properties are presented in Sects. 5.4 and 5.5, respectively. In Sect. 5.6 we present the X-ray properties of the ICM in the cluster. Discussion and conclusions are presented in Sects. 5.7 and 5.8.

5.3 Radio observations and data reduction

A 2256 was observed with the WSRT at 2273 MHz (13.2 cm, S-band) and with the Effelsberg 100-m telescope at 2640 MHz (11.35 cm, S-band) and at 4850 MHz (6.2 cm, C-band) in full polarization mode. The data calibration and total intensity results have been presented in Chap. 4. In this section we recall the observations and present the main steps of the polarization calibration and imaging.

5.3.1 WSRT observations in the S-band

The WSRT receiver used for the observations is equipped with circularly polarized feeds (RR, LL, RL, LR), which allowed us to follow standard procedures within AIPS to calibrate the polarization data. Without any polarization calibration, an unpolarized source would appear to be polarized at some percent level due to impurities of the feeds (*instrumental polarization*). Furthermore, without calibration of the R-L phase difference, the polarization angle is

undetermined. The best way to determine the leakage terms, which produce the instrumental polarization, is to observe an unresolved source (calibrator) over a wide range in parallactic angle. The polarization angle of the calibrator will appear to rotate in the sky with the parallactic angle, while the instrumental contribution stays constant. This allows to simultaneously solve for the source polarization properties and the leakage terms (task PCAL in AIPS). However, in the case of the WSRT, the antennas are equatorially mounted and the parallactic angle of the polarization remains fixed as a source is tracked. This allowed us to observe the calibrators only twice, at the beginning and at the end of the observation session. Calibration of the absolute polarization angle (or R-L phase difference) can be accomplished with a single observation of a polarized source having a known polarization angle (the true R-L phase difference is twice the source polarization angle). We used 3C286, which has a known polarization angle of 33° at frequencies above 1 GHz and a fractional polarization of 10% [1].
The three pointings were imaged and self-calibrated separately both in total and polarized intensity. Images of the Stokes parameters I, U and Q were obtained for each pointing from the polarization products:

$$I = \frac{LL + RR}{2} \qquad Q = \frac{RL + LR}{2} \qquad U = \frac{RL - LR}{2}$$

They were then combined (separately for I, U and Q) and corrected for the primary beam attenuation with the FLATN task in AIPS. Images of the polarized intensity $PI = (Q^2 + U^2)^{1/2}$, position angle of the polarization $\Psi = 0.5 \arctan(U/Q)$ and fractional polarization $FPOL = PI/I$ were obtained from the resultant I, U and Q mosaics (task COMB in AIPS). The polarized intensity map was produced by blanking whenever the S/N ratio in the output map fell below 3. The fractional polarization map was produced by blanking whenever both the input total intensity or linear polarization map values fell below their respective 3σ level. The polarization angle map was corrected for the Galactic contribution estimated from the recently reconstructed map of the Galactic Faraday Sky (Oppermann et al., 2012). At the position of the cluster (l=111.09, b=31.7) the map provides a Galactic Faraday depth of -22.87 ± 11.8 rad/m^2, which at the observing wavelength implies a rotation of the polarization vectors in the map of $\Delta\Psi = -22.87\text{rad} \cdot \lambda^2 = -22.^{\circ}8$.

5.3.2 Effelsberg observations in the S and C bands

Data in the four Stokes parameters (R, L, U, Q) were provided for each frequency channel, for each horn, and for each coverage of the field for the Effelsberg observations at 2640 MHz and 4850 MHz. As circular polarization is generally very week, the maps in R and L contain identical signals and can be averaged, providing the total intensity map.
The polarization data reduction was performed with the NOD2 software package, following the standard procedures, similar to the total intensity data. Images of the polarized intensity PI, position angle of the polarization Ψ and fractional polarization $FPOL$ were produced in AIPS with the same procedures as for the WSRT data. The correction for the Galactic polarization contribution implies a rotation of the polarization angle of -16.°7 at 2640 MHz and of -5.°04 at 4850 MHz.

[1] From the VLA calibrator manual

5.4 Polarization properties

The polarization E-vectors and the fractional polarization of the relic emission in A2256 at 2273 MHz, 2640 MHz and 4850 MHz are presented in Fig. 5.1, Fig. 5.2 upper panels and Fig. 5.2 lower panels respectively. The electric (polarization) vectors shown are perpendicular to the projection of the magnetic field onto the plane of the sky. The intrinsic polarization degree depends on the particle distribution, but the observed degree of polarization can be decreased by a disordered and complex magnetic-field structure. The alignment of the electric vectors of the linearly polarized emission in the radio relic region observed at all frequencies suggests that the intergalactic magnetic field is well ordered in these regions. The ordering is on scales of the order of few arcminutes, as it "survives" the big beam of the Effelsberg observations. The orientation of the polarization vectors differ between the north-eastern (G region) and south-western (H region) regions of the relic emission identified in the total intensity image at all frequencies and resolutions. However, the visible transition of the vectors' orientation from one region to the other suggests that the two regions are physically connected and not just superimposed by projection effects. In the high-resolution WSRT image the polarized emission with S/N>3 traces only the brightest regions of emission (Figs. 5.1a and 5.1b). However, plotting the polarized emission without any cut in S/N, we can see polarization along all the relic structure that looks significant upon visual inspection (Fig. 5.1c). In the north-eastern part of the relic, the B-vectors (perpendicular to the E-vectors shown) nicely follow the arc-like shaped emission. The same orientation is roughly observable also at higher frequencies in the Effelsberg images, although with much lower resolution (Fig. 5.2). In the south-western region the B-vectors are aligned with the major axis of the relic at 4850 MHz (Fig. 5.2c), while they appear to be rotated at lower frequencies (Fig. 5.2a). The fractional polarization reaches a mean level of $\sim$ 30% in both regions, with peaks of 45-50 % in the high-resolution WSRT image (Fig. 5.1b). In the low-resolution Effelsberg images the level of polarization is lower, due to beam depolarization. The north-eastern region of the relic is more polarized ($\sim$25-30 %) than the south-western one ($\sim$ 10-15%) at 2640 MHz (Fig. 5.2b), while they are similarly polarized at a level of $\sim$ 25-30 % at 4850 MHz (Fig. 5.2d).

5.5 Spectral index maps

We have produced a spectral-index map between 2640 and 4850 MHz, which is shown in Fig. 5.3a with the corresponding spectral index error map (Fig. 5.3b). In order to compare the intensities on the same spatial scale, we convolved the 4850 MHz Effelsberg map to a beam of $4\overset{'}{.}4 \times 4\overset{'}{.}4$ to match the resolution of the 2640 MHz map. The spectral index map was computed on a pixel by pixel base, only where the two maps are both above their respective 3σ level ($3\sigma_{2640MHz} = 4 \cdot 10^{-3}$ Jy/beam, $3\sigma_{4850MHz} = 3 \cdot 10^{-3}$ Jy/beam). The north-eastern part of the diffuse emission (region G), with spectral indices of -0.6 to -0.8, has a general flatter spectrum than the south-western part (region H). In particular in the south-western region of the relic there is a steepening from the NW edge (with values -0.6 to -0.8) toward the SE edge (with values -1.1 to -1.2). These values are in agreement with what was reported by Brentjens (2008) at lower frequencies: he found that the mean spectral index between 351 and 1369 MHz in the G region is -0.76 ± 0.03, while in the H region it is -1.17 ± 0.03. Kale & Dwarakanath (2010) also found occurrence an of flat spectral indices in the G and H region of the diffuse emission

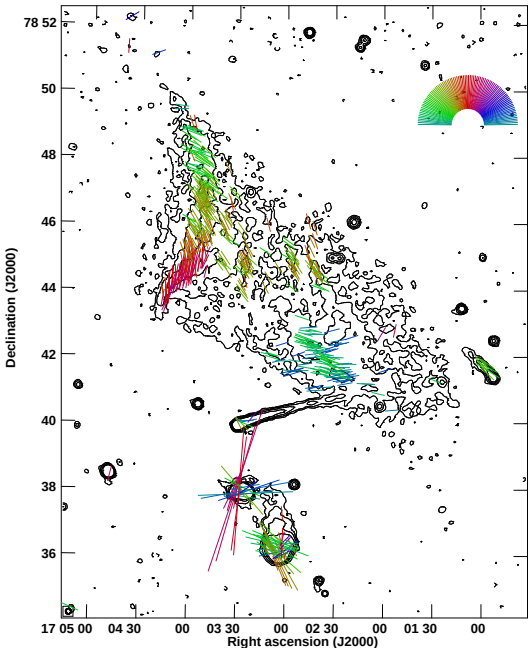

(a) Polarization E-vectors with S/N > 3.

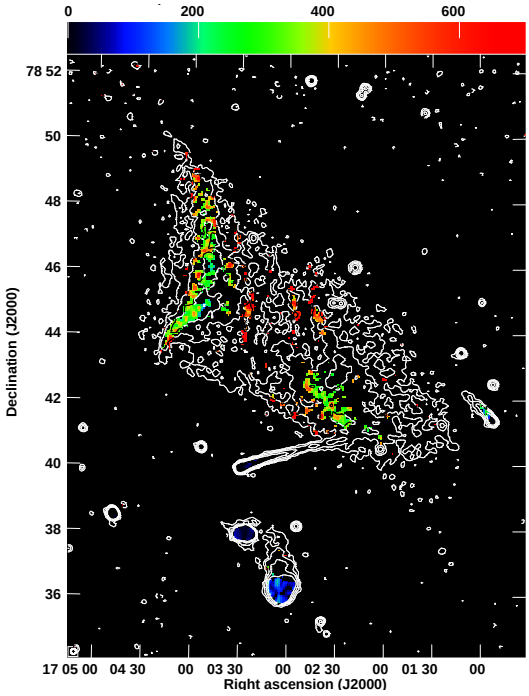

(b) Fractional polarization (polarization emission with S/N > 3).

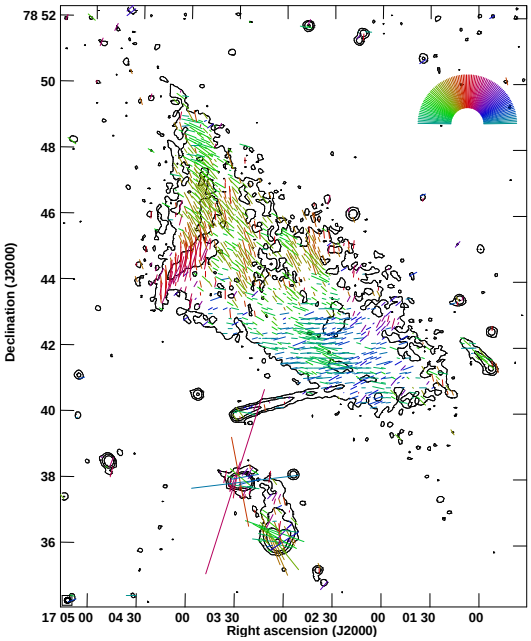

(c) Polarization E-vectors without S/N cuts.

Fig. 5.1: A2256 polarization properties at 2273 MHz from WSRT observations. In all panels the contours represent the total intensity emission (see Chap. 4). The beam, shown in the bottom-left corner, is $9\farcs84 \times 9\farcs44$.

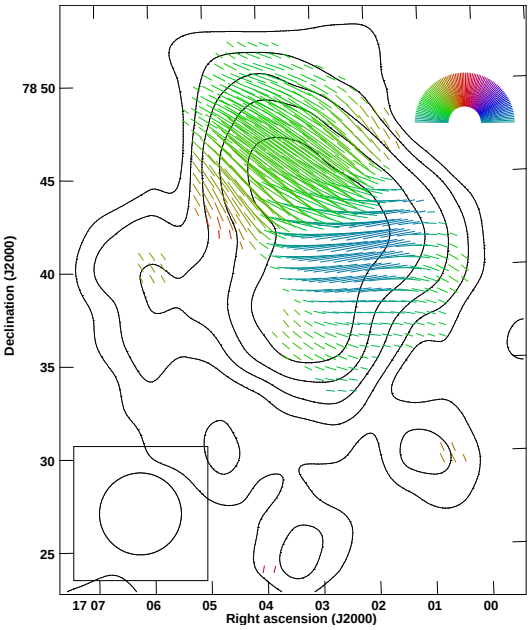

(a) Polarization E-vectors at 2640 MHz.

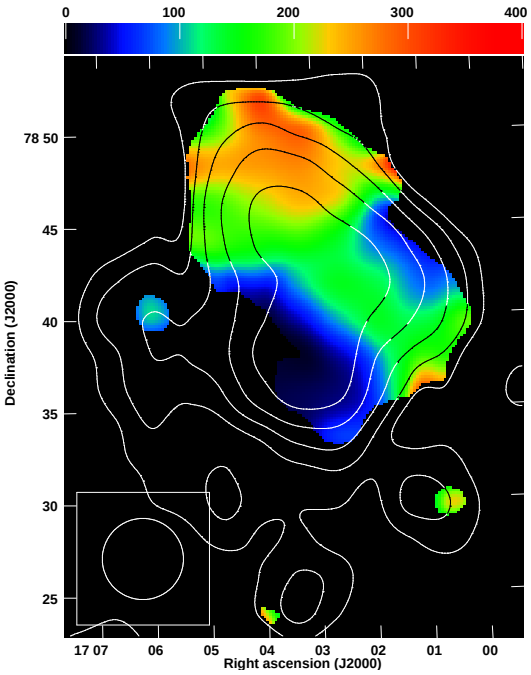

(b) Fractional polarization at 2640 MHz.

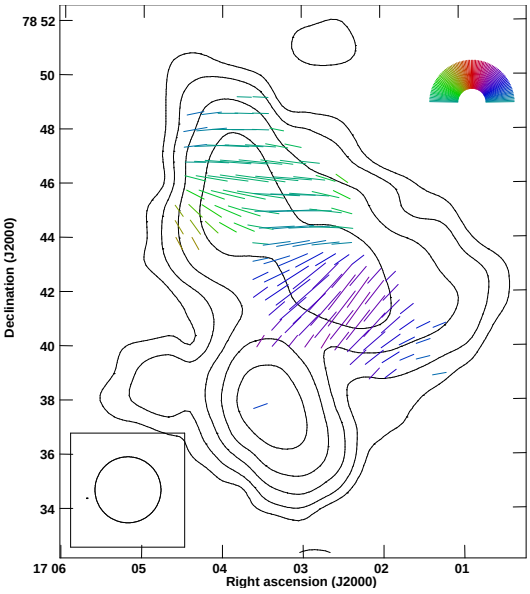

(c) Polarization E-vectors at 4850 MHz.

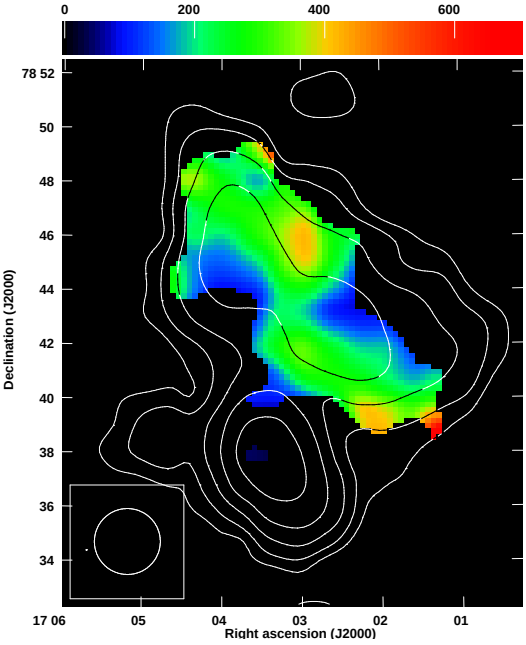

(d) Fractional polarization at 4850 MHz.

Fig. 5.2: A2256 polarization in S and C bands.

($\alpha_{150}^{350} \sim -0.7\text{to}-1.1$, $\alpha_{350}^{1369} \sim -0.7\text{to}-0.9$). We made another spectral-index map between 4850 and 10450 MHz (shown in Fig. 5.3c) with the corresponding spectral index error map (Fig. 5.3d). Also in this case we convolved the 10450 MHz data to a lower resolution to match the one at 4850 MHz and blanked below the 3σ lvel of the two images ($3\sigma_{4850MHz} = 1.86 \cdot 10^{-3}$ Jy/beam and $3\sigma_{10450MHz} = 1.9 \cdot 10^{-3}$ Jy/beam). Here the situation looks inverted with the north-eastern region steeper than the south-western part. While in the south-west the spectral indices keep values around -1, in the north-eastern region they change from -0.6 to -0.8 to values around -1.3.

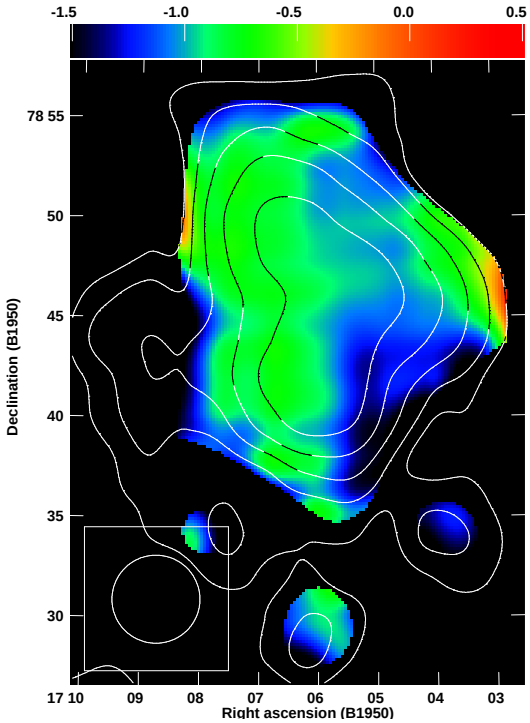

(a) Spectral index map between 2640 and 4850 MHz.

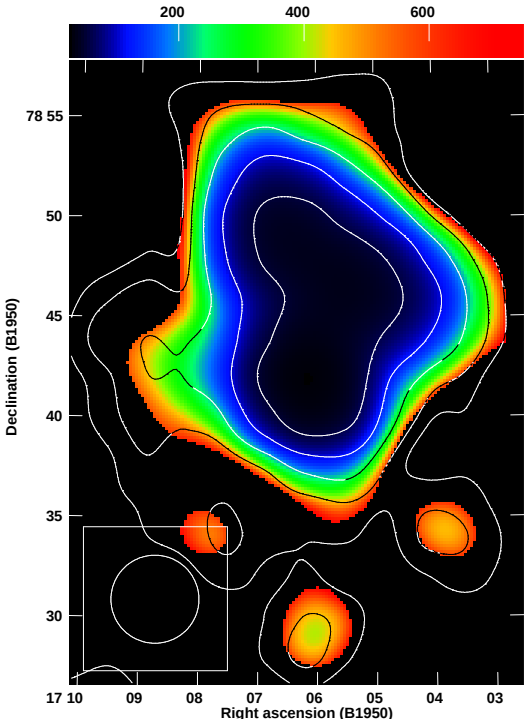

(b) Spectral index error map between 2640 and 4850 MHz.

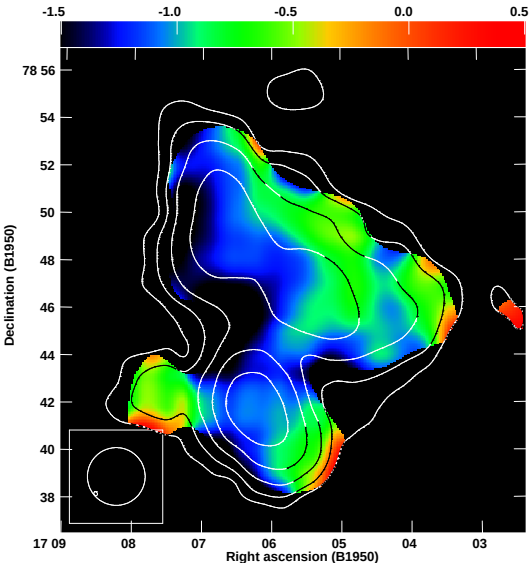

(c) Spectral index map between 4850 and 10450 MHz.

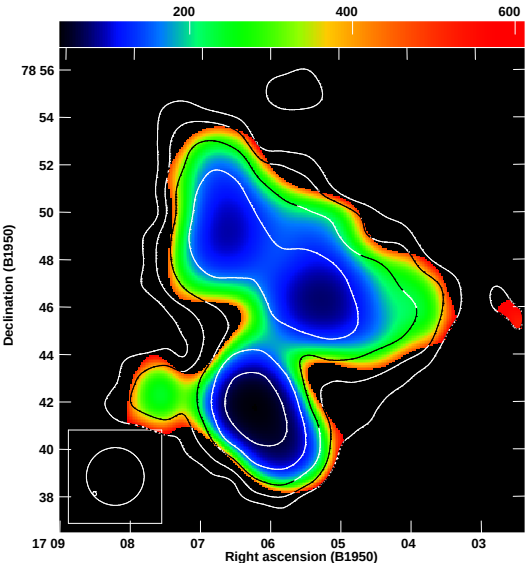

(d) Spectral index error map between between 4850 and 10450 MHz.

Fig. 5.3: Spectral index and error maps.

5.6 X-ray properties of the ICM

We used X-ray observations taken from the XMM-Newton archive to examine the properties of the ICM in A2256 (data reduction presented in Sec. 4.4). In Chap. 4 we showed the ICM temperatures calculated in specific regions across the radio relic emission (see Fig. 5.5a). Here we derive a *hardness ratio* map, which is also a qualitative indicator of the gas temperature in the cluster. The hardness ratio of the cluster X-ray emission is a proxy for the temperature because the principal component of the cluster X-ray emission is thermal bremsstrahlung. For thermal bremsstrahlung the X-ray luminosity in the energy band $E_1 - E_2$ is given by:

$$L_X \propto \int_{E_1}^{E_2} n_e^2 T^{-1/2} e^{-E/kT} G(E,T) dE \tag{5.1}$$

where n_e is the electron number density and $G(E,T)$ is the quantum correction Gaunt factor (Peacock, 1999). From the temperature dependence of L_X, one sees that the hardness ratio L_{X2}/L_{X1} is just related to the ratio of temperatures T_2/T_1, which after integration is roughly proportional to $(T_2/T_1)^{1/2}$. Thus, a higher hardness ratio corresponds to harder X-ray emission, which in turn implies a higher temperature (Henning et al., 2009). Moreover, a two-band hardness ratio map requires fewer counts than spectral temperatures profiles for a given signal-to-noise, and is suitable for XMM-Newton data, which are heavily affected by flares. The hardness ratio map between the bands (2-5 keV) and (0.5-2 keV) for A 2256 is shown in Fig. 5.4. It shows that the south-western region of the relic is colder. This is in agreement with previous studies conducted by Sun et al. (2002) and Bourdin & Mazzotta (2008), which showed that this region is cold due to the presence of a colder sub-cluster at an early stage of merging with the main cluster from the west.

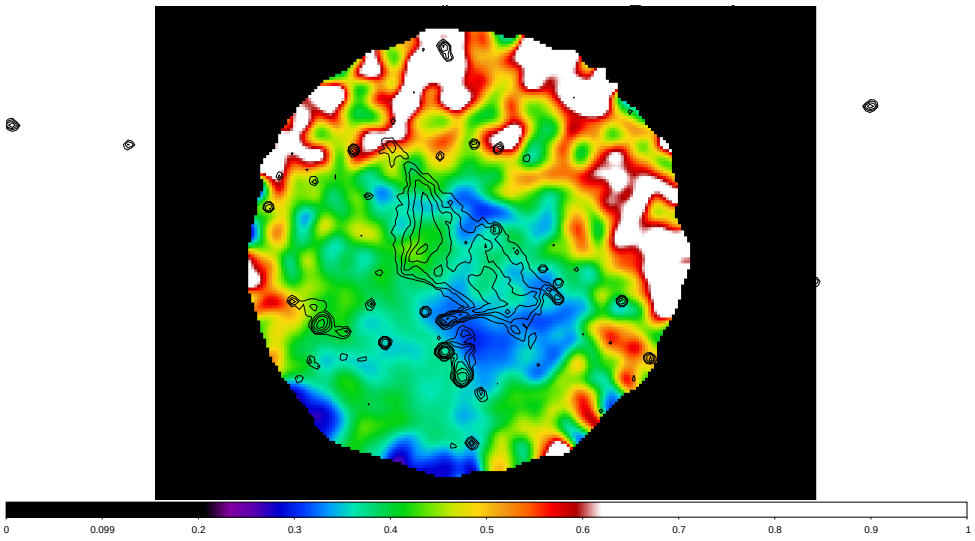

Fig. 5.4: Hardness ratio map for Abell 2256 from XMM-Newton data.

Radio relics are usually associated with *outgoing merger shocks* that travel from the core of a merging event outwardly towards the periphery of the clusters. We therefore checked for radial trends, extracting the ICM surface brightness profiles in the north-west (NW) direction

across region G of the relic and in the west (W) direction across region H (see Fig. 5.5a). The data binning inside each sector was determined by the requirement to have a constant number of photon counts inside each bin. For the extraction we used only the soft band (0.5-2 KeV), which is less affected by the soft-protons problem. The surface-brightness profiles are plotted in Fig. 5.5. The vertical lines in the plots corresponds to the annuli drawn in Fig. 5.5a and mark the position of the inner and outer edges of the radio relic with respect to the cluster center. Across the inner edge of region G we clearly see a break in the surface brightness profile (Fig. 5.5b). However, density jumps alone can not distinguish between *shocks* and *cold fronts*. An accurate temperature profile across this edge is needed to check wether this is associated with a decrease or increase of the temperature. In the latter case these features may correspond to a contact discontinuity where no clear pressure jump is present, usually referred to as a cold front (Markevitch et al., 2000). Bourdin & Mazzotta (2008) and Sun et al. (2002) reported the presence of two other cold fronts in A2256 at the south-eastern side of the cluster and in the south-western region respectively. Multiple cold fronts have already been observed in Abell 2142 (Rossetti et al., 2013).
The western sector (across region H) shows a break in the location of the outer edge of the radio relic that might indicate the presence of a shock front (Fig. 5.5c). However, we measured approximately the same temperature in the regions r4 and r5 across this edge (see Sect. 4.6).

5.7 Discussion

In the shock acceleration formation mechanism for relics the magnetic field becomes aligned with the shock front. In both low-resolution maps it seems that there is a transition in the polarization orientation going from the south-western to the north-eastern regions, suggesting maybe that the shock front encounters a medium with different properties while propagating. A linearly polarized wave when propagating through a magnetized plasma can experience *Faraday rotation*. This produces a rotation of the final electric field vectors and a reduction of the degree of polarization in case of large beam and coincidence of emitting and rotating volumes. The intrinsic polarization angle Ψ_0 will be rotated by an amount :

$$\Delta\Psi = \Psi - \Psi_0 = \lambda^2 \cdot RM$$

where λ is the observing wavelength and RM is the so-called Rotation Measure defined as:

$$RM = 812 \int_0^L n_e B_z dl (\mathrm{rad/m^2}),$$

where n_e is the thermal electron density in cm^{-3}, B_z is the magnetic field component along the line of sight in μG and L is the path length traveled by the radiation through the plasma in kpc.

This effect depends on the properties of the medium and decreases with increasing frequency so that going to high frequencies the observed polarization is closest to the intrinsic one. So, assuming that the polarization properties observed at 4850 MHz are close to the intrinsic one, the fact that at 2640 MHz the south-western part is less polarized than the north-eastern part can suggest that the radiation coming from south-west experienced higher Faraday depolarization because it traveled through a larger distance from us. Moreover in region G the E-vectors at 2640 MHz look rotated respect the E-vectors at 4850 MHz, suggesting that the

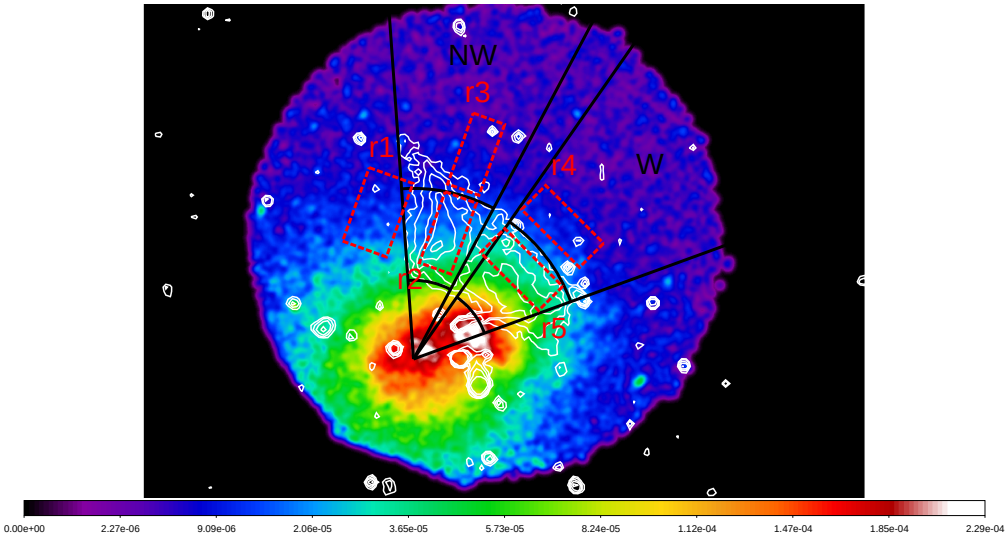

(a) Sectors used for the surface brightness extraction.

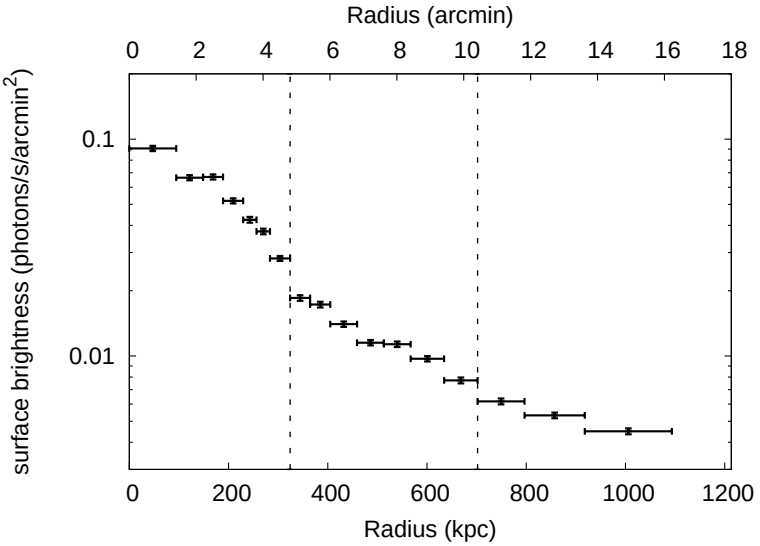

(b) XMM-Newton surface brightness profile in the north-western sector.

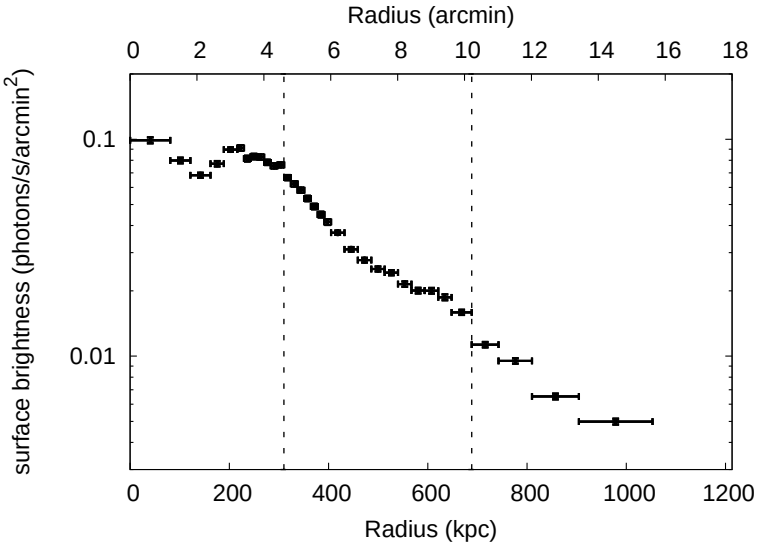

(c) XMM-Newton surface brightness profile in the western sector.

Fig. 5.5: XMM-Newton image of A2256 in colour scale (upper panel). White contours represents the radio relic emission. Red dashed boxes represents the area used for the temperature calculations presented in Sect. 4.6.

polarized emission undergoes Faraday rotation in the intergalactic medium while propagating toward us.
We suggest that these features could be explained if the relic is inclined with respect to the line of sight, with the north-eastern region H on the near side toward us and more external with respect to the cluster and the south-western region G more embedded in the intra-cluster medium, behind the sub-cluster merging from the west.

5.8 Conclusions

In this chapter we have presented a polarization and spectral study of the extended radio relic emission in the galaxy cluster A2256. The main points of this study can be summarized as follows.

1. We present new polarization observations of the radio relic in A2256 performed at 2273 MHz (13.2 cm, S-band) with the WSRT, and at 2640 MHz (11.35 cm, S-band) and 4850 MHz (6.2 cm, C-band) with the Effelsberg 100-m telescope. At all frequencies and resolutions, the orientation of the polarization vectors differ between the north-eastern region G and south-western region H of the relic emission identified in the total intensity image. In the north-eastern part of the relic, the B-vectors nicely follow the arc-like shape emission in the high-resolution WSRT image. The same orientation is roughly observable also at higher frequencies in the Effelsberg images, although with much lower resolution. In the south-western region the B-vectors are aligned with the major axis of the relic at 4850 MHz, while they look rotated at lower frequencies. In the high-resolution WSRT image the fractional polarization reaches a mean level of $\sim$ 30% in both regions, with peaks of 45-50 %. In the low-resolution Effelsberg images the level of polarization is lower due to beam depolarization. The north-eastern region of the relic is more polarized ($\sim$25-30 %) than the south-western one ($\sim$ 10-15%) at 2640 MHz, while they look similarly polarized at a level of $\sim$ 25-30 % at 4850 MHz.

2. We produced two spectral-index maps in the ranges 2640-4850 MHz and 4850-10450 MHz. We found a general occurrence of flat spectral indices in the region of the relic up to high frequencies, in agreement with the integrated radio spectrum shown in Chap. 4.

3. We complemented our radio analysis with archival X-ray observations. The hardness ratio map shows that the south-western region of the cluster is colder, probably due to the presence of a colder sub-cluster.

4. We suggest that the above properties can be explained by a geometry in which the relic is inclined respect the line of sight, with the north-eastern region H on the near side toward us and more external with respect to the cluster, and the south-western region G more embedded in the intra-cluster medium, behind the sub-cluster merging from the west.

Chapter 6

Preliminary results on the radio halo in the Coma cluster at GHz frequencies

6.1 Introduction

One of the first and strongest observational evidences supporting the scenario of the in-situ turbulent re-acceleration for radio halos has been the steepening observed above 1 GHz in the integrated spectrum of the radio halo in the Coma cluster (Schlickeiser et al., 1987; Thierbach et al., 2003). The high-frequency flux densities were measured with low resolution single-dish images and strongly depend on a correct subtraction of the contribution from point sources embedded in the diffuse emission. We observed the Coma halo field in the L-band with the Effelsberg telescope (see Sect. 3.3.1) and in the S-band with both the Effelsberg telescope and the WSRT. The high resolution of the latter observations will enable us to carefully estimate the contribution of point sources and confirm the steepening.

6.1.1 Effelsberg observations in the L-band

The Effelsberg L-band data and data reduction are presented in Sect. 3.3.1. Figure 3.4 shows the large field of the Coma cluster covered by the observations, which includes both the radio halo and relic emission. Figure 6.1 shows the diffuse halo emission from the Effelsberg observations after subtraction of the NVSS point-source emission. From preliminary measurements, the residual flux in the halo region is $\sim$ 200 mJy, lower than previously reported by Kim et al. (1990) ($S = 530 \pm 50$ mJy) and by Deiss et al. (1997) ($S = 640 \pm 35$ mJy) at similar frequencies. Our preliminary flux density measured at 1.4 GHz is plotted (in red) for comparison with the collection of other flux densities from literature (taken from Table 6 of Thierbach et al., 2003). Further and more careful flux density measurements will be performed in order to check the high frequency end of the integrated radio spectrum of the Coma halo.

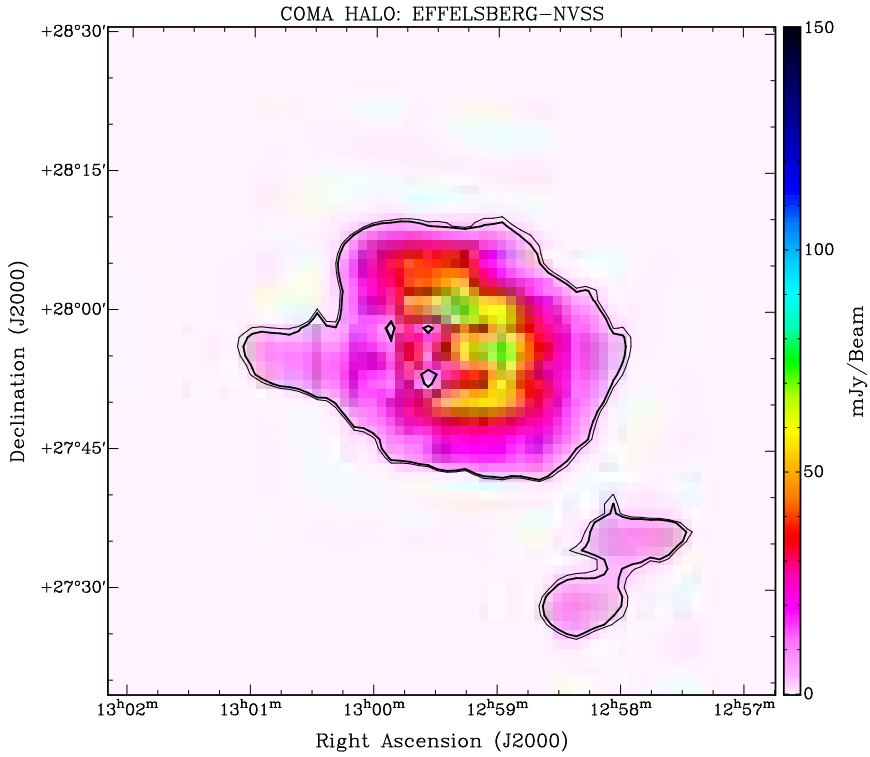

Fig. 6.1: Effelsberg L-band total intensity image of the Coma halo field, with NVSS emission subtracted out. The resolution is 9′.4 × 9′.4.

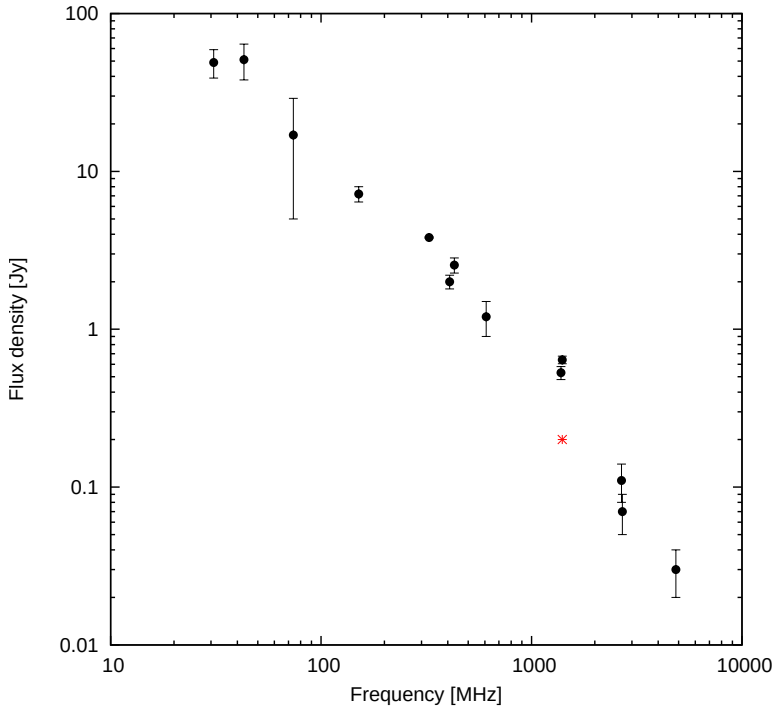

Fig. 6.2: Coma radio halo flux densities measurements from literature. Our preliminary measurement at 1400 MHz is plotted in red for comparison.

6.1.2 WSRT observations in the S-band

The Coma halo field was observed with the WSRT at 2273 MHz (13.2 cm, S-band) in full polarization. The observations were carried out in the *mosaic mode*, with 9 different pointing centers (summarized in Table 6.1).

Tab. 6.1: S-band WSRT observational parameters.

Pointing center (J2000) RA	DEC	Frequency (MHz)	Bandwidth (MHz)	Exposure time (min)
12:58:55	+27:48:50	2273	160	72
12:59:40	+27:48:50	2273	160	72
13:00:25	+27:48:50	2273	160	96
13:00:25	+27:58:50	2273	160	72
13:00:25	+28:08:50	2273	160	72
12:59:40	+28:08:50	2273	160	96
12:58:55	+28:08:50	2273	160	72
12:58:55	+27:58:50	2273	160	72
12:59:40	+27:58:50	2273	160	96

The data reduction was performed with the AIPS package, following standard procedures similar to those used for the WSRT observations of the Coma relic (Sect. 3.3.2) and of the relic in A2256 (Sect. 4.3.1). The nine pointings were imaged and self-calibrated separately with the IMAGR task in AIPS. Images of the Stokes parameter I, U and Q were obtained for each pointing and were then combined (separately for I, U and Q) and corrected for the primary beam attenuation with the FLATN task in AIPS. Preliminary images of the polarized intensity PI and position angle of the polarization Ψ were produced. Figure 6.3 shows the S-band WSRT image of the Coma halo field with polarization vectors over-plotted. The halo emission is completely filtered out as a result of the zero-spacing problem and the steep spectrum.

The high resolution of these observations will enable us to carefully estimate the point source contribution and confirm the steepening.

Figure 6.4 shows the entire $3^\circ \times 3^\circ$ field centered on the Coma cluster, observed with the Effelsberg in the S-band (see Sect. 3.5).

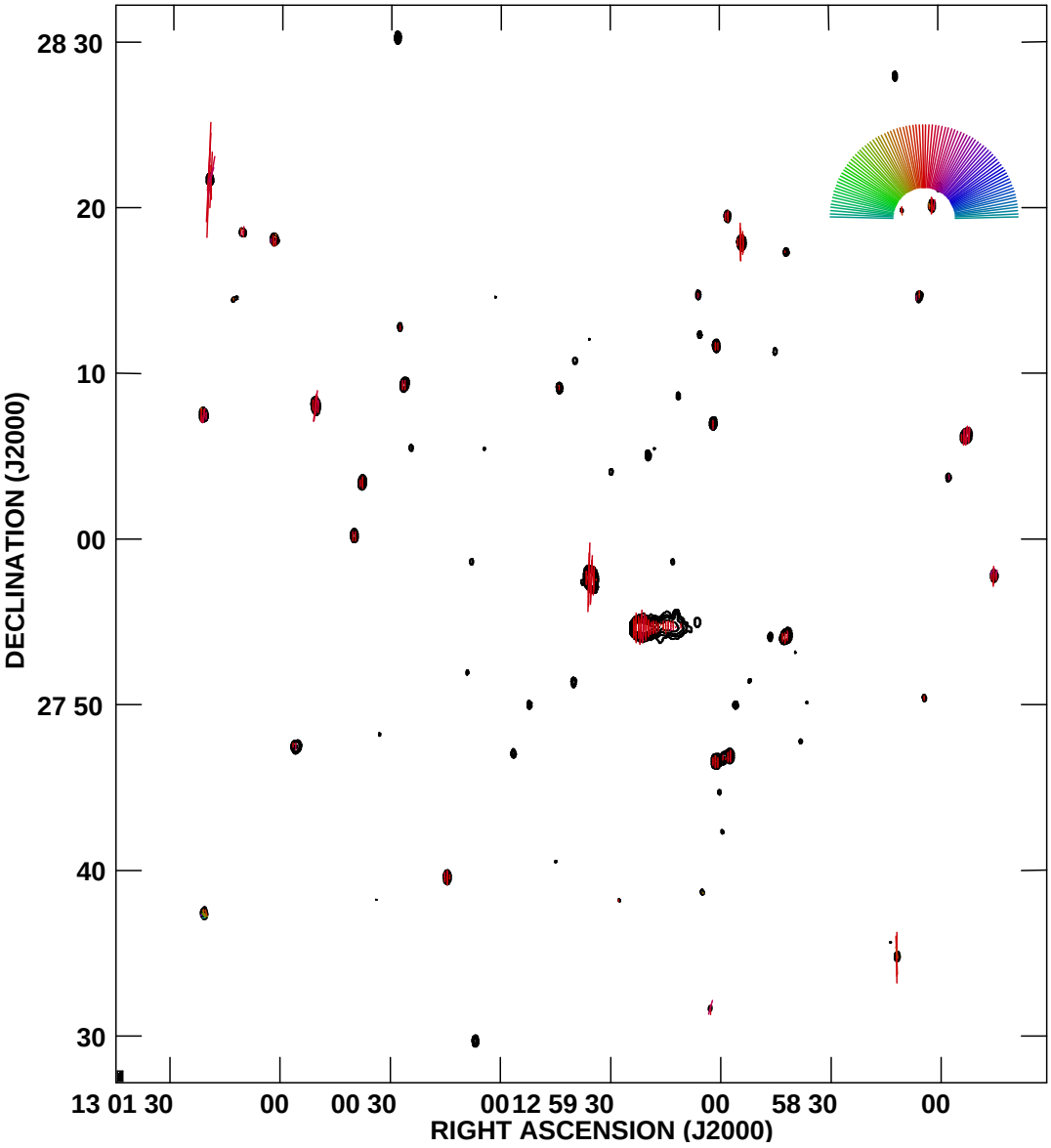

Fig. 6.3: WSRT S-band total intensity image of the Coma halo field.

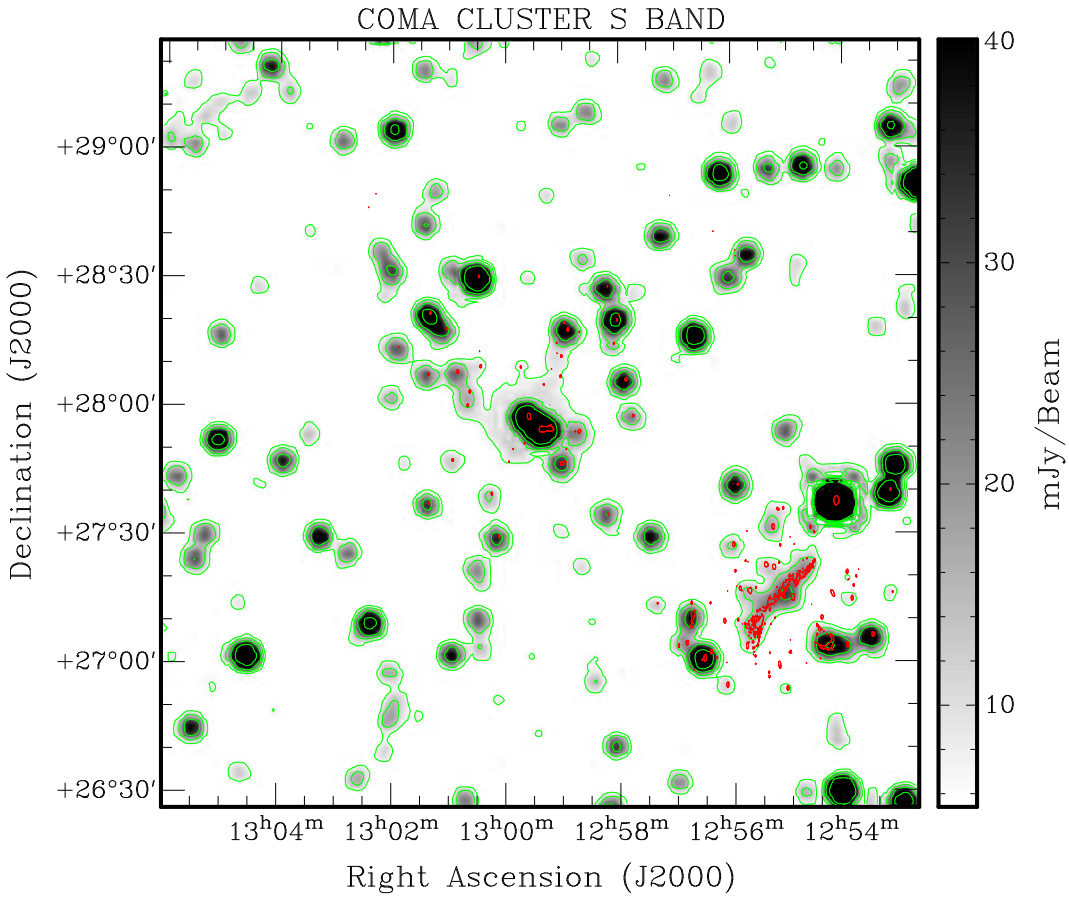

Fig. 6.4: The coma cluster in the S-band. Grey scale and green contours represent the Effelsberg observations (Sect. 3.5) contours are drawn at [1,2,4,8] × 0.007 mJy/beam. The synthesized beam is 4.′4×4.′4. Red contours represent the WSRT observations of the coma relic (drown at 0.0001 mJy/beam; Sect. 3.3.2) and of the radio halo (drown at 0.0003 mJy/beam; Fig. 6.3).

.

Summary and conclusions

In this thesis we studied the properties at GHz frequencies of the diffuse non-thermal sources observed in an increasing number of clusters of galaxies known as *radio relics* and *radio halos*. These sources, not related to any discrete source in the clusters but rather with the diffuse medium, require some form of particle acceleration given their large extent (of the order of Mpc). It has been proposed that they are connected to the most energetic phenomena in the universe, mergers between clusters, during which shocks and turbulence may develop in the ICM leading eventually to the acceleration of particles through Fermi mechanisms.
In order to test the proposed models, we studied the properties of these sources in two clusters, Abell 1656 (best known as the Coma cluster) and Abell 2256, both known to posses both a radio relic and a radio halo. We have observed a wide field on the Coma cluster, covering both the peripheral relic and the central halo, with the Effelsberg 100-m telescope at 1400 MHz (21.4 cm, L-band). Moreover, the Coma relic field and the Coma halo field have been covered separately with respectively a 3-pointing and a 9-pointing mosaics performed with the WSRT at 2273 MHz (13.2 cm, S-band). We have observed the cluster Abell 2256 with the Effelsberg-100m Telescope at 2640 MHz (11.35 cm, S-band) and at 4850 MHz (6.2 cm, C-band). The same field was observed with a 3-pointing mosaic performed with the WSRT at 2273 MHz (13.2 cm, S-band). The observations were performed in full polarization mode.
In the following the main results derived from the analysis of these data will be summarized.

- We showed the importance of high-frequencies observations (at GHz frequency e.g. L, S and C bands) for the study of these sources. According to the predictions of the proposed models, the currently known radio relics and halos are the most extreme and energetic cases, for which high-frequency observations are necessary to constrain the shape of the spectra and search for the presence of a steepening, in order to test the models expectations. For most of the currently known radio relics and halos the highest studied frequency is 1.4 GHz. Therefore, observations at GHz frequencies of the currently known radio relics and halos are essential to test the models and shed light on the origin of these diffuse sources. However, increasing the observing frequencies, the interferometers encounter the technical problem of the *missing short spacings*, that makes them "blind" to very extended structures. On the other hand, single dishes are optimal to catch all the emission from a field but they lack angular resolution.
  We showed the power of a method for combining interferometric and single-dish data in the Fourier domain, which allows to produce images sensitive to a large range of angular scales, from the map sizes down to the original synthesized beam of the interferometric observations. We applied this technique for the first time to study in detail the properties in the L and S bands of the radio relic emission in the Coma cluster. The final combined image in the L-band has a resolution of $45'' \times 45''$ and contains information on spatial frequencies in the range 0 - 4.5 kλ. The final combined image in the S-band has a resolution of $33\farcs17 \times 13\farcs16$, and complete uv-coverage in the range 0 - 21 kλ.

We showed that none of our images support the tentatively detection recently claimed in literature of an extension to the radio relic which would make its total extend ∼ 2 Mpc. Our data suggest an extent for the relic of no more than ∼30′ (∼ 800 kpc) at different frequencies and resolutions. Moreover the combination method allowed to recover ∼ 40 % of the total flux in the L-band and ∼ 36% of the total flux in the S-band, missed in the interferometric observations due to the zero spacing problem. The combination technique is, therefore, a promising tool to study the properties of radio relics and halos at GHz frequencies.

- To date, the integrated radio spectra of these diffuse sources are obtained with more than three flux density measurements at different frequencies only in few cases.

  We have performed an accurate study of the integrated spectrum of the radio relic in Abell 2256, by using our new GHz observations together with images available at other frequencies in the literature. This study was inspired by the publication of an unusually flat ($\alpha \sim 0.8$) integrated radio spectrum at low frequencies for the relic host in this cluster. It is, moreover, the first cluster observed with LOFAR, for which the flux density at very low frequencies (63 MHz) is available. We measured the relic flux density at six different frequencies in the range 63 -10450 MHz on images convolved to the same resolution and considering the same region for the integration. The integrated spectra of the discrete sources embedded in the relic emission have been carefully determined in the same frequency range in order to carefully account for their contribution to the emission. In this way we constrained the radio integrated spectrum of the radio relic in Abell 2256 over the widest frequency range collected so far for this kind of objects. We found that, although the relic spectrum between 63 and 10450 MHz is not inconsistent with a single power law with $\alpha(relic)_{63}^{10450} = 0.92 \pm 0.02$, a separate fit of the spectra between 63 and 1369 MHz and between 1369 and 10450 MHz shows that these two frequency ranges are best represented by two different power laws, with $\alpha(relic)_{63}^{1369} = 0.8488 \pm 0.0003$ and $\alpha(relic)_{1369}^{10450} = 1.00 \pm 0.02$. We discussed the difficulties in explaining such spectral behaviors in the framework of diffusive shock acceleration or acceleration by adiabatic compression.
  The high resolution (∼ 10″) of the WSRT observations allowed us to analyze the substructures of the diffuse emission in detail. The relic shows a complex morphology, with two regions of enhanced surface brightness: regions G and H. At full resolution the entire relic emission covers an area of about $10.'6 \times 5'$. We have investigated the possibility that the G and H regions are two independent relics with different properties in the frequency range 351-10450 MHz. We find that the singular spectra of regions G and H show a similar flat trend respect the total relic with $\alpha(G)_{351}^{10450} = 0.97 \pm 0.04$ and $\alpha(H)_{351}^{10450} = 0.92 \pm 0.02$. The absence of a pronounced steepening in the integrated radio spectrum of the relic as well as of the regions G and H separately, rule out a phoenices origin for the relic/s.

  We presented new flux density measurements of the Coma radio relic at 1400 and 2640 MHz. Fitting our data with flux densities published in literature we find that the Coma relic integrated spectrum in the frequency range 139-4759 MHz is consistent with a straight power law with a spectral index $\alpha = 1.21 \pm 0.03$, consistent with what previously reported. In the scenario of diffusive shock acceleration for radio relic and applying the

Rankine-Hugoniot conditions, this spectral index requires the presence of a shock with Mach number $M = 3.2^{+0.28}_{-0.15}$.

- We investigated the connection between the radio properties of the diffuse emissions with the thermal-dynamical properties of the host clusters.

  In the case of Abell 2256 we used Suzaku and XMM-Newton X-ray observations to study the properties of the intra-cluster medium in the regions across the radio relic emission. We found a ICM temperature ratio $T_2/T_1 \sim 1.7$ across the G region of the radio relic supporting the presence, if any, of a weak shock, weaker than what expected from the radio properties of the diffuse emission. Moreover, no clear break in the ICM surface brightness profile is detected in correspondence to this edge. No temperature jumps are observed in two areas across the H region of the relic, probably due to the projection of a colder sub-cluster approaching the main cluster from the west. However, in this direction the surface brightness profile shows a break in the location of the outer edge of the radio relic that might indicate the presence of a shock front.

  In the case of the Coma cluster we collaborated to the study of Sunyaev Zeldovich Planck data to investigate whether a pressure discontinuity is directly visible at the position of the radio relic. We tested different models and found that a power-law featuring a pressure discontinuity at the position of the relic provides the best fit to the SZ data. The best fit pressure ratio suggests a mildly supersonic shock ($M \sim 3$), in agreement with what predicted from the radio integrated spectrum, bolstering the hypothesis of shock origin of the radio relics. The analysis supports the idea of an outwardly moving shock front, likely caused by the first infall of the group NGC 4839.

- In case of shock acceleration, high-frequency radio emission in a radio relic mark the location of freshly accelerated electrons closest to the shock front, and it is therefore a cleaner indicator of the shock front geometry. Moreover at high frequency the polarization properties of the emission are less affected by Faraday rotation and the observed polarization is closest to the intrinsic one. In case of DSA alignment of the polarization vectors and spectral distribution across the extent of radio relics can therefore be connected to the geometry of the shock passage.

  We conducted a detailed study of the polarization and spectral properties across the diffuse emission in Abell 2256. We produced two spectral-index maps in the ranges 2640-4850 MHz and 4850-10450 MHz. We found a general occurrence of flat spectral indices in the region of the relic up to high frequencies, in agreement with the integrated radio spectrum. At all the three frequencies and resolutions studied, the orientation of the polarization vectors differ between the north-eastern region G and south-western region H of the relic emission identified in the total intensity image. However, the visible transition of the vectors' orientation from one region to the other suggests that the two regions are physically connected and not just superimposed by projection effects. In the north-eastern part of the relic, the B-vectors nicely follow the arc-like shape emission in the high-resolution WSRT image. The same orientation is roughly observable also at higher frequencies in the Effelsberg images, although with much lower resolution. In the south-western region the B-vectors are aligned with the major axis of the relic at

4850 MHz, while they look rotated at lower frequencies. In the high-resolution WSRT image the fractional polarization reaches a mean level of ∼ 30% in both regions, with peaks of 45-50 %. In the low-resolution images, the north-eastern region of the relic is more polarized (∼25-30 %) than the south-western one (∼ 10-15%) at 2640 MHz, while they look similarly polarized at a level of ∼ 25-30 % at 4850 MHz. We suggest that the above properties can be explained by a geometry in which the relic is inclined respect the line of sight, with the north-eastern region H on the near side toward us and more external with respect to the cluster, and the south-western region G more embedded in the intra-cluster medium, maybe behind the sub-cluster merging from the west.

- One of the first and strongest observational evidences supporting the scenario of the in-situ turbulent re-acceleration for radio halos has been the steepening observed above 1 GHz in the integrated spectrum of the radio halo in the Coma cluster. The high-frequency flux densities were measured with low resolution single-dish images and strongly depend on a correct subtraction of the contribution from point sources embedded in the diffuse emission.

  We showed preliminary results of observations of the Coma cluster performed with the Effelsberg-100m and the WSRT. The high resolution of the latter observations will enable us to carefully estimate the point source contribution and confirm the steepening.

- We finally showed the very preliminary results from the analysis of Effelsberg C-band observations of the clusters Abell 0115 and Abell 2255. These observations were carried out during an observational campaign of a small sample of galaxy clusters known to host diffuse non-thermal emission. The aim of the campaign and the focus of future work will be to increase the number of radio relics and halos with constrained integrated spectra up to high frequencies.

Appendix A

Formulary for test-particle DSA

The table provides the quantity in the rows as function of the quantity in the columns. Here we use the convention:

$$S(\nu) \propto \nu^{-\alpha_{inj}},$$

with the definition

$$\alpha_{inj} = \frac{\beta_{inj} - 1}{2} = \frac{\delta_{inj} - 3}{2}$$

as in Sect. 2.3.1.

Legend:

- α_{obs}: observed (with aging) synchrotron spectral index;
- α_{inj}: injection (without aging) synchrotron spectral index;
- β_{obs}: observed (with aging) particle energy distribution index;
- β_{inj}: injection (without aging) particle energy distribuion index;
- δ_{obs}: observed (with aging) particle momentum distribution index;
- δ_{inj}: injection (without aging) particle momentum distribution index;
- M: shock Mach number;
- C: shock compression ratio.

	α_{obs}	α_{inj}	β_{obs}	β_{inj}	δ_{obs}	δ_{inj}	M	C
$\alpha_{obs} =$		$\alpha_{inj} + 0.5$	$\frac{\beta_{obs}-1}{2}$	$\frac{\beta_{inj}}{2}$	$\frac{\delta_{obs}-3}{2}$	$\frac{\delta_{inj}-2}{2}$	$\frac{M^2+1}{M^2-1}$	$\frac{3C-1}{2(C-1)}$
$\alpha_{inj} =$	$\alpha_{obs} - 0.5$		$\frac{\beta_{inj}-2}{2}$	$\frac{\beta_{inj}-1}{2}$	$\frac{\delta_{obs}-4}{2}$	$\frac{\delta_{inj}-3}{2}$	$\frac{M^2+3}{2(M^2-1)}$	$\frac{3}{2(C-1)}$
$\beta_{obs} =$	$1+2\alpha_{obs}$	$2+2\alpha_{inj}$		$\beta_{inj} + 1$	$\delta_{obs} - 2$	$\delta_{inj} - 1$	$\frac{3M^2+1}{M^2-1}$	$\frac{2C+1}{C-1}$
$\beta_{inj} =$	$2\alpha_{obs}$	$1+2\alpha_{inj}$	$\beta_{obs} - 1$		$\delta_{obs} - 3$	$\delta_{inj} - 2$	$\frac{2M^2+2}{M^2-1}$	$\frac{C+2}{C-1}$
$\delta_{obs}=$	$3+2\alpha_{obs}$	$4+2\alpha_{inj}$	$\beta_{obs} + 2$	$\beta_{inj} + 3$		$\delta_{inj} + 1$	$\frac{5M^2-1}{M^2-1}$	$\frac{4C-1}{C-1}$
$\delta_{inj}=$	$2+2\alpha_{obs}$	$3+2\alpha_{inj}$	$\beta_{obs} + 1$	$\beta_{inj} + 2$	$\delta_{obs} - 1$		$\frac{4M^2}{M^2-1}$	$\frac{3C}{C-1}$
$M =$	$\sqrt{\frac{\alpha_{obs}+1}{\alpha_{obs}-1}}$	$\sqrt{\frac{2\alpha_{inj}+3}{2\alpha_{inj}-1}}$	$\sqrt{\frac{\beta_{obs}+1}{\beta_{obs}-3}}$	$\sqrt{\frac{\beta_{inj}+2}{\beta_{inj}-2}}$	$\sqrt{\frac{\delta_{obs}-5}{\delta_{obs}-1}}$	$\sqrt{\frac{\delta_{inj}}{\delta_{inj}-4}}$		$\sqrt{\frac{-3C}{C-4}}$
$C =$	$\frac{2\alpha_{obs}-1}{2\alpha_{obs}-3}$	$\frac{3+2\alpha_{inj}}{2\alpha_{inj}}$	$\frac{\beta_{obs}+1}{\beta_{obs}-2}$	$\frac{\beta_{inj}+2}{\beta_{inj}-1}$	$\frac{\delta_{obs}-1}{\delta_{obs}-4}$	$\frac{\delta_{inj}}{\delta_{inj}-3}$	$\frac{4M^2}{M^2+3}$	

Appendix B

Preliminary images from a Effelsberg campaign

The Effelsberg observations presented in this thesis were part of an observational campaign performed at high frequencies (S, C and X bands) and in full polarization mode, of a small sample of clusters known to host a radio relic and/or a radio halo. Here we show the preliminary images at 4850 MHz (with a resolution of 2′.43 × 2′.43) for other two of these clusters: Abell 0115 and Abell 2255.

Abell 0115

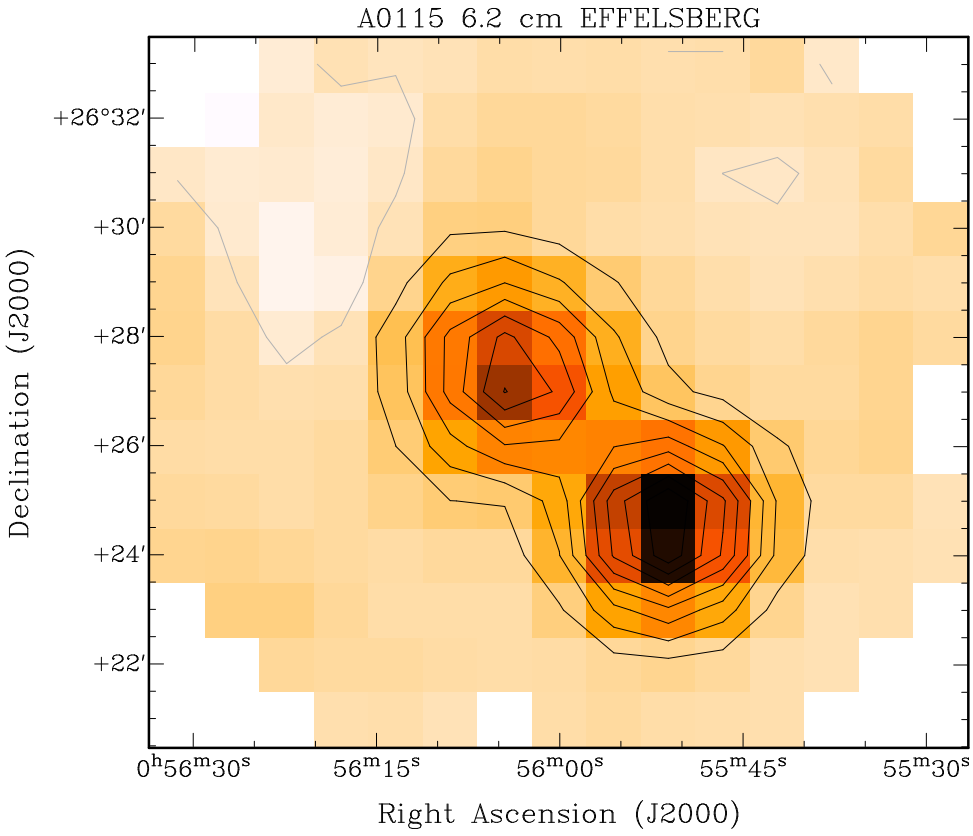

Fig. B.1: C-band preliminary total intensity image of Abell 0115.

.

Abell 2255

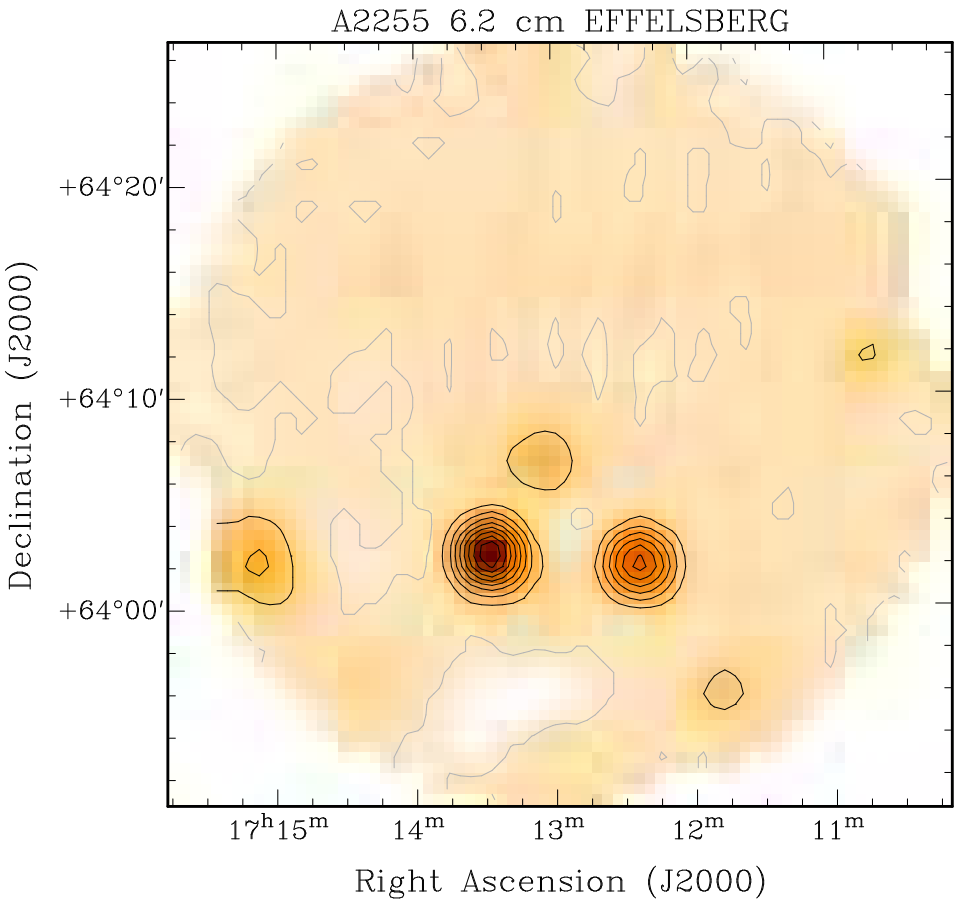

Fig. B.2: C-band preliminary total intensity image of Abell 2255.

.

Bibliography

Abell, G. O. 1958, ApJS, 3, 211

Abell, G. O., Corwin, Jr., H. G., & Olowin, R. P. 1989, ApJS, 70, 1

Ackermann, M., Ajello, M., Allafort, A., et al. 2010, ApJ, 717, L71

Ajello, M., Rebusco, P., Cappelluti, N., et al. 2009, ApJ, 690, 367

Akamatsu, H., Inoue, S., Sato, T., et al. 2013, PASJ, 65, 89

Akamatsu, H. & Kawahara, H. 2011, ArXiv e-prints

Akamatsu, H., Takizawa, M., Nakazawa, K., et al. 2012, PASJ, 64, 67

Allen, S. W., Evrard, A. E., & Mantz, A. B. 2011, ARA&A, 49, 409

Andernach, H., Feretti, L., & Giovannini, G. 1984, A&A, 133, 252

Anders, E. & Grevesse, N. 1989, Geochim. Cosmochim. Acta, 53, 197

Arnaud, M., Pratt, G. W., Piffaretti, R., et al. 2010, A&A, 517, A92

Baars, J. W. M., Genzel, R., Pauliny-Toth, I. I. K., & Witzel, A. 1977, A&A, 61, 99

Bacchi, M., Feretti, L., Giovannini, G., & Govoni, F. 2003, A&A, 400, 465

Ballarati, B., Feretti, L., Ficarra, A., et al. 1981, A&A, 100, 323

Bell, A. R. 2004, MNRAS, 353, 550

Bennett, C. L., Banday, A. J., Gorski, K. M., et al. 1996, ApJ, 464, L1

Bennett, C. L., Halpern, M., Hinshaw, G., et al. 2003, ApJS, 148, 1

Berrington, R. C., Lugger, P. M., & Cohn, H. N. 2002, AJ, 123, 2261

Bertschinger, E. 1985, ApJS, 58, 39

Blandford, R. & Eichler, D. 1987, Phys. Rep., 154, 1

Blasi, P. 2000, ApJ, 532, L9

Blasi, P. 2010, MNRAS, 402, 2807

Blasi, P. & Colafrancesco, S. 1999, Astroparticle Physics, 12, 169

Blasi, P., Gabici, S., & Brunetti, G. 2007, International Journal of Modern Physics A, 22, 681

Böhringer, H., Schuecker, P., Guzzo, L., et al. 2004, A&A, 425, 367

Bonafede, A. 2010, PhD thesis, Universita degli Studi di Bologna

Bonafede, A., Feretti, L., Giovannini, G., et al. 2009, A&A, 503, 707

Bonamente, M., Joy, M. K., & Lieu, R. 2003, ApJ, 585, 722

Bonamente, M., Lieu, R., Joy, M. K., & Nevalainen, J. H. 2002, ApJ, 576, 688

Borgani, S. & Kravtsov, A. 2011, Advanced Science Letters, 4, 204

Bourdin, H. & Mazzotta, P. 2008, A&A, 479, 307

Bowyer, S., Korpela, E. J., Lampton, M., & Jones, T. W. 2004, ApJ, 605, 168

Boylan-Kolchin, M., Springel, V., White, S. D. M., Jenkins, A., & Lemson, G. 2009, MNRAS, 398, 1150

Bregman, J. N. & Lloyd-Davies, E. J. 2006, ApJ, 644, 167

Brentjens, M. A. 2008, A&A, 489, 69

Bridle, A. H. & Fomalont, E. B. 1976, A&A, 52, 107

Bridle, A. H., Fomalont, E. B., Miley, G. K., & Valentijn, E. A. 1979, A&A, 80, 201

Broadhurst, T., Benítez, N., Coe, D., et al. 2005, ApJ, 621, 53

Brown, S., Duesterhoeft, J., & Rudnick, L. 2011, ApJ, 727, L25

Brown, S. & Rudnick, L. 2011, MNRAS, 412, 2

Brüggen, M., Bykov, A., Ryu, D., & Röttgering, H. 2012, Space Sci. Rev., 166, 187

Brunetti, G. & Blasi, P. 2005, MNRAS, 363, 1173

Brunetti, G., Blasi, P., Cassano, R., & Gabici, S. 2004, MNRAS, 350, 1174

Brunetti, G., Cassano, R., Dolag, K., & Setti, G. 2009, A&A, 507, 661

Brunetti, G. & Lazarian, A. 2007, MNRAS, 378, 245

Brunetti, G. & Lazarian, A. 2011, MNRAS, 412, 817

Brunetti, G., Setti, G., Feretti, L., & Giovannini, G. 2001, MNRAS, 320, 365

Buote, D. A. 2001, ApJ, 553, L15

Bykov, A. M., Bloemen, H., & Uvarov, Y. A. 2000, A&A, 362, 886

Carilli, C. L., Perley, R. A., Dreher, J. W., & Leahy, J. P. 1991, ApJ, 383, 554

Carilli, C. L. & Taylor, G. B. 2002, ARA&A, 40, 319

Carlstrom, J. E., Holder, G. P., & Reese, E. D. 2002, ARA&A, 40, 643

Cassano, R. & Brunetti, G. 2005, MNRAS, 357, 1313

Cassano, R., Brunetti, G., Röttgering, H. J. A., & Brüggen, M. 2010, A&A, 509, A68

Cassano, R., Brunetti, G., Venturi, T., et al. 2008, A&A, 480, 687

Cavaliere, A. & Fusco-Femiano, R. 1976, A&A, 49, 137

Clarke, T. E., Enßlin, T., Finoguenov, A., et al. 2011, Mem. Soc. Astron. Italiana, 82, 547

Clarke, T. E. & Ensslin, T. A. 2006, AJ, 131, 2900

Cohen, A. S. & Clarke, T. E. 2011, AJ, 141, 149

Cohen, A. S., Lane, W. M., Cotton, W. D., et al. 2007, AJ, 134, 1245

Condon, J. J., Cotton, W. D., Greisen, E. W., et al. 1998, AJ, 115, 1693

Cordey, R. A. 1985, MNRAS, 215, 437

Dallacasa, D., Brunetti, G., Giacintucci, S., et al. 2009, ApJ, 699, 1288

De Paolis, F., Ingrosso, G., Nucita, A. A., & Orlando, D. 2003, A&A, 398, 435

Deiss, B. M., Reich, W., Lesch, H., & Wielebinski, R. 1997, A&A, 321, 55

Dennison, B. 1980, ApJ, 239, L93

Dermer, C. D. 1986, A&A, 157, 223

Dolag, K., Bartelmann, M., & Lesch, H. 2002, A&A, 387, 383

Dolag, K., Bykov, A. M., & Diaferio, A. 2008, Space Sci. Rev., 134, 311

Dolag, K. & Enßlin, T. A. 2000, A&A, 362, 151

Donnert, J., Dolag, K., Cassano, R., & Brunetti, G. 2010, MNRAS, 407, 1565

Drury, L. O. 1983, Reports on Progress in Physics, 46, 973

Durret, F., Kaastra, J. S., Nevalainen, J., Ohashi, T., & Werner, N. 2008, Space Sci. Rev., 134, 51

Ebeling, H., Edge, A. C., Allen, S. W., et al. 2000, MNRAS, 318, 333

Ebeling, H., Edge, A. C., Bohringer, H., et al. 1998, MNRAS, 301, 881

Eilek, J. & Weatherall, J. C. 1999, in Diffuse Thermal and Relativistic Plasma in Galaxy Clusters, ed. H. Boehringer, L. Feretti, & P. Schuecker, 249

Emerson, D. T. & Graeve, R. 1988, A&A, 190, 353

Enßlin, T. A., Biermann, P. L., Klein, U., & Kohle, S. 1998, A&A, 332, 395

Enßlin, T. A. & Brüggen, M. 2002, MNRAS, 331, 1011

Enßlin, T. A. & Gopal-Krishna. 2001, in Astronomical Society of the Pacific Conference Series, Vol. 250, Particles and Fields in Radio Galaxies Conference, ed. R. A. Laing & K. M. Blundell, 454

Enßlin, T. A., Lieu, R., & Biermann, P. L. 1999, A&A, 344, 409

Evrard, A. E., Metzler, C. A., & Navarro, J. F. 1996, ApJ, 469, 494

Faridani, S., Flöer, L., Kerp, J., & Westmeier, T. 2014, A&A, 563, A99

Felten, J. E., Gould, R. J., Stein, W. A., & Woolf, N. J. 1966, ApJ, 146, 955

Feretti, L., Bacchi, M., Slee, O. B., et al. 2006, MNRAS, 368, 544

Feretti, L., Brunetti, G., Giovannini, G., et al. 2004, Journal of Korean Astronomical Society, 37, 315

Feretti, L., Giovannini, G., Govoni, F., & Murgia, M. 2012, A&A Rev., 20, 54

Feretti, L. & Neumann, D. M. 2006, A&A, 450, L21

Feretti, L., Schuecker, P., Böhringer, H., Govoni, F., & Giovannini, G. 2005, A&A, 444, 157

Fermi, E. 1949, Physical Review, 75, 1169

Ferrari, C., Govoni, F., Schindler, S., Bykov, A. M., & Rephaeli, Y. 2008, Space Sci. Rev., 134, 93

Finoguenov, A., Sarazin, C. L., Nakazawa, K., Wik, D. R., & Clarke, T. E. 2010, ApJ, 715, 1143

Fletcher, A., Beck, R., Shukurov, A., Berkhuijsen, E. M., & Horellou, C. 2011, MNRAS, 412, 2396

Fujita, Y. & Sarazin, C. L. 2001, ApJ, 563, 660

Fusco-Femiano, R., Dal Fiume, D., Feretti, L., et al. 1999, ApJ, 513, L21

Gabici, S. & Blasi, P. 2003, ApJ, 583, 695

Gao, L., Frenk, C. S., Jenkins, A., Springel, V., & White, S. D. M. 2012, MNRAS, 419, 1721

Giacintucci, S., Venturi, T., Macario, G., et al. 2008, A&A, 486, 347

Giovannini, G., Bonafede, A., Feretti, L., et al. 2009, A&A, 507, 1257

Giovannini, G., Feretti, L., & Andernach, H. 1985, A&A, 150, 302

Giovannini, G., Feretti, L., Girardi, M., et al. 2011, A&A, 530, L5

Giovannini, G., Feretti, L., & Stanghellini, C. 1991, A&A, 252, 528

Giovannini, G., Feretti, L., Venturi, T., Kim, K.-T., & Kronberg, P. P. 1993, ApJ, 406, 399

Giovannini, G., Kim, K. T., Kronberg, P. P., & Venturi, T. 1990, in IAU Symposium, Vol. 140, Galactic and Intergalactic Magnetic Fields, ed. R. Beck, R. Wielebinski, & P. P. Kronberg, 492

Giovannini, G., Tordi, M., & Feretti, L. 1999, 4, 141

Gitti, M., Brunetti, G., & Setti, G. 2002, A&A, 386, 456

Gitti, M., Ferrari, C., Domainko, W., Feretti, L., & Schindler, S. 2007, A&A, 470, L25

Govoni, F. & Feretti, L. 2004, International Journal of Modern Physics D, 13, 1549

Govoni, F., Feretti, L., Giovannini, G., et al. 2001, A&A, 376, 803

Govoni, F., Murgia, M., Feretti, L., et al. 2005, A&A, 430, L5

Govoni, F., Murgia, M., Markevitch, M., et al. 2009, A&A, 499, 371

Gursky, H., Solinger, A., Kellogg, E. M., et al. 1972, ApJ, 173, L99

Helmboldt, J. F., Kassim, N. E., Cohen, A. S., Lane, W. M., & Lazio, T. J. 2008, ApJS, 174, 313

Henning, J. W., Gantner, B., Burns, J. O., & Hallman, E. J. 2009, ApJ, 697, 1597

Hoeft, M., Brüggen, M., Yepes, G., Gottlöber, S., & Schwope, A. 2008, MNRAS, 391, 1511

Högbom, J. A. 1974, A&AS, 15, 417

Iapichino, L. & Brüggen, M. 2012, MNRAS, 423, 2781

Intema, H. T. 2009, PhD thesis, Leiden Observatory, Leiden University, P.O. Box 9513, 2300 RA Leiden, The Netherlands

Jaffe, W. J. 1977, ApJ, 212, 1

Jaffe, W. J. & Perola, G. C. 1973, A&A, 26, 423

Johnston-Hollitt, M., Clay, R. W., Ekers, R. D., Wieringa, M. H., & Hunstead, R. W. 2002, in IAU Symposium, Vol. 199, The Universe at Low Radio Frequencies, ed. A. Pramesh Rao, G. Swarup, & Gopal-Krishna, 157

Kaastra. 2008, Clusters of Galaxies: Beyond the Thermal View (Springer)

Kaastra, J. S., Lieu, R., Tamura, T., Paerels, F. B. S., & den Herder, J. W. 2003, A&A, 397, 445

Kaiser, N., Squires, G., & Broadhurst, T. 1995, ApJ, 449, 460

Kale, R. & Dwarakanath, K. S. 2010, ApJ, 718, 939

Kang, H. 2011, Journal of Korean Astronomical Society, 44, 49

Kang, H. & Ryu, D. 2010, ApJ, 721, 886

Kang, H. & Ryu, D. 2011, ApJ, 734, 18

Kang, H., Ryu, D., Cen, R., & Ostriker, J. P. 2007, ApJ, 669, 729

Kang, H., Ryu, D., & Jones, T. W. 2012, ApJ, 756, 97

Kardashev, N. S. 1962, Soviet Ast., 6, 317

Kempner, J. C., Blanton, E. L., Clarke, T. E., et al. 2004, in The Riddle of Cooling Flows in Galaxies and Clusters of galaxies, ed. T. Reiprich, J. Kempner, & N. Soker, 335

Kim, K.-T., Kronberg, P. P., Dewdney, P. E., & Landecker, T. L. 1990, ApJ, 355, 29

Kim, K.-T., Kronberg, P. P., Giovannini, G., & Venturi, T. 1989, Nature, 341, 720

Klein, U. & Mack, K.-H. 1995, in Astronomical Society of the Pacific Conference Series, Vol. 75, Multi-Feed Systems for Radio Telescopes, ed. D. T. Emerson & J. M. Payne, 318

Komissarov, S. S. & Gubanov, A. G. 1994, A&A, 285, 27

Krivonos, R. A., Vikhlinin, A. A., Markevitch, M. L., & Pavlinsky, M. N. 2003, Astronomy Letters, 29, 425

Kronberg, P. P., Kothes, R., Salter, C. J., & Perillat, P. 2007, ApJ, 659, 267

Krymskii, G. F. 1977, Akademiia Nauk SSSR Doklady, 234, 1306

Kulsrud, R. M. & Ferrari, A. 1971, Ap&SS, 12, 302

Large, M. I., Mathewson, D. S., & Haslam, C. G. T. 1959, Nature, 183, 1663

Lazarian, A. & Beresnyak, A. 2006, MNRAS, 373, 1195

Lieu, R., Mittaz, J. P. D., Bowyer, S., et al. 1996a, Science, 274, 1335

Lieu, R., Mittaz, J. P. D., Bowyer, S., et al. 1996b, ApJ, 458, L5

Lin, Y.-T., Partridge, B., Pober, J. C., et al. 2009, ApJ, 694, 992

Lovisari, L., Kapferer, W., Schindler, S., & Ferrari, C. 2009, A&A, 508, 191

Lovisari, L., Schindler, S., & Kapferer, W. 2011, A&A, 528, A60

Lucek, S. G. & Bell, A. R. 2000, MNRAS, 314, 65

Lukash, V. N., Mikheeva, E. V., & Malinovsky, A. M. 2011, Physics Uspekhi, 54, 983

Lynds, R. & Petrosian, V. 1986, in Bulletin of the American Astronomical Society, Vol. 18, Bulletin of the American Astronomical Society, 1014

Markevitch, M., Gonzalez, A. H., David, L., et al. 2002, ApJ, 567, L27

Markevitch, M., Govoni, F., Brunetti, G., & Jerius, D. 2005, ApJ, 627, 733

Markevitch, M., Ponman, T. J., Nulsen, P. E. J., et al. 2000, ApJ, 541, 542

Markevitch, M. & Vikhlinin, A. 1997, ApJ, 491, 467

Markevitch, M. & Vikhlinin, A. 2007, Phys. Rep., 443, 1

Miller, N. A., Owen, F. N., & Hill, J. M. 2003, AJ, 125, 2393

Miniati, F. 2003, MNRAS, 342, 1009

Miniati, F., Jones, T. W., Kang, H., & Ryu, D. 2001a, ApJ, 562, 233

Miniati, F., Ryu, D., Kang, H., & Jones, T. W. 2001b, ApJ, 559, 59

Miniati, F., Ryu, D., Kang, H., et al. 2000, ApJ, 542, 608

Mora, S. C. & Krause, M. 2013, A&A, 560, A42

Navarro, J. F., Frenk, C. S., & White, S. D. M. 1995, MNRAS, 275, 56

Ogrean, G. A. & Brüggen, M. 2013, MNRAS, 433, 1701

Oppermann, N., Junklewitz, H., Robbers, G., et al. 2012, A&A, 542, A93

Owen, F. N. & Ledlow, M. J. 1997, ApJS, 108, 41

Pacholczyk, A. G. 1970, Radio astrophysics. Nonthermal processes in galactic and extragalactic sources

Peacock, J. A. 1999, Cosmological Physics

Peebles, P. J. E. 1980, The large-scale structure of the universe

Peebles, P. J. E. 1993, Principles of Physical Cosmology

Peng, B., Kraus, A., Krichbaum, T. P., & Witzel, A. 2000, A&AS, 145, 1

Perley, R. A., Schwab, F. R., Bridle, A. R., & Wilkinson, P. 1990, Journal of the British Astronomical Association, 100, 150

Perley, R. A. & Taylor, G. B. 1999, VLA Calibrator Manual, Tech. Rep., NRAO

Petrosian, V. 2001, ApJ, 557, 560

Petrosian, V., Bykov, A., & Rephaeli, Y. 2008, Space Sci. Rev., 134, 191

Pfrommer, C. & Enßlin, T. A. 2004, A&A, 413, 17

Pfrommer, C., Enßlin, T. A., & Springel, V. 2008, MNRAS, 385, 1211

Pinzke, A. 2010, PhD thesis, University of Stockholm

Pinzke, A. & Pfrommer, C. 2010, MNRAS, 409, 449

Pizzo, R. F. 2010, PhD thesis, University of Groningen

Pizzo, R. F., de Bruyn, A. G., Bernardi, G., & Brentjens, M. A. 2011, A&A, 525, A104

Planck Collaboration, Ade, P. A. R., Aghanim, N., et al. 2013a, A&A, 550, A131

Planck Collaboration, Ade, P. A. R., Aghanim, N., et al. 2013b, A&A, 554, A140

Planck Collaboration, Ade, P. A. R., Aghanim, N., et al. 2011a, A&A, 536, A1

Planck Collaboration, Ade, P. A. R., Aghanim, N., et al. 2011b, A&A, 536, A11

Reimer, O., Pohl, M., Sreekumar, P., & Mattox, J. R. 2003, ApJ, 588, 155

Reiprich, T. H., Basu, K., Ettori, S., et al. 2013, Space Sci. Rev., 177, 195

Renaud, M., Bélanger, G., Paul, J., Lebrun, F., & Terrier, R. 2006, A&A, 453, L5

Rephaeli, Y. 1977, ApJ, 212, 608

Rephaeli, Y., Gruber, D., & Arieli, Y. 2006, ApJ, 649, 673

Rephaeli, Y., Gruber, D., & Blanco, P. 1999, ApJ, 511, L21

Rephaeli, Y., Nevalainen, J., Ohashi, T., & Bykov, A. M. 2008, Space Sci. Rev., 134, 71

Rosati, P., Borgani, S., & Norman, C. 2002, ARA&A, 40, 539

Rosati, P., Tozzi, P., Gobat, R., et al. 2009, A&A, 508, 583

Rossetti, M., Eckert, D., De Grandi, S., et al. 2013, A&A, 556, A44

Rossetti, M. & Molendi, S. 2004, A&A, 414, L41

Rottgering, H., Snellen, I., Miley, G., et al. 1994, ApJ, 436, 654

Rottgering, H. J. A., Wieringa, M. H., Hunstead, R. W., & Ekers, R. D. 1997, MNRAS, 290, 577

Rottmann, H., Mack, K.-H., Klein, U., & Wielebinski, R. 1996, A&A, 309, L19

Russel, H. 2010, in Galaxy Clusters: Observations, Physics and Cosmology

Rybicki, G. B. & Lightman, A. P. 1979, Radiative processes in astrophysics

Ryu, D., Kang, H., Cho, J., & Das, S. 2008, Science, 320, 909

Ryu, D., Kang, H., Hallman, E., & Jones, T. W. 2003, ApJ, 593, 599

Santos, J. S., Rosati, P., Tozzi, P., et al. 2008, A&A, 483, 35

Sarazin, C. L. 1986, Reviews of Modern Physics, 58, 1

Sarazin, C. L. & Kempner, J. C. 2000, ApJ, 533, 73

Sarazin, C. L. & Lieu, R. 1998, ApJ, 494, L177

Schlickeiser, R. & Miller, J. A. 1998, ApJ, 492, 352

Schlickeiser, R., Sievers, A., & Thiemann, H. 1987, A&A, 182, 21

Sieber, W., Haslam, C. G. T., & Salter, C. J. 1979, A&A, 74, 361

Simard-Normandin, M., Kronberg, P. P., & Button, S. 1981, ApJS, 45, 97

Slee, O. B., Roy, A. L., Murgia, M., Andernach, H., & Ehle, M. 2001, AJ, 122, 1172

Smith, S. 1936, ApJ, 83, 23

Springel, V. 2005, MNRAS, 364, 1105

Stanimirovic, S. 1999, PhD thesis, Arecibo Observatory, NAIC/Cornell University, HC 3 Box 53995, Arecibo, Puerto Rico 00612

Stanimirovic, S. 2002, in Astronomical Society of the Pacific Conference Series, Vol. 278, Single-Dish Radio Astronomy: Techniques and Applications, ed. S. Stanimirovic, D. Altschuler, P. Goldsmith, & C. Salter, 375–396

Stanimirovic, S., Altschuler, D., Goldsmith, P., & Salter, C., eds. 2002, Astronomical Society of the Pacific Conference Series, Vol. 278, Single-Dish Radio Astronomy: Techniques and Applications

Stanimirovic, S., Staveley-Smith, L., Dickey, J. M., Sault, R. J., & Snowden, S. L. 1999, MNRAS, 302, 417

Stroe, A., Rumsey, C., Harwood, J. J., et al. 2014, ArXiv e-prints

Stroe, A., van Weeren, R. J., Intema, H. T., et al. 2013, A&A, 555, A110

Struble, M. F. & Rood, H. J. 1991, ApJS, 77, 363

Subramanian, K., Shukurov, A., & Haugen, N. E. L. 2006, MNRAS, 366, 1437

Sun, M., Murray, S. S., Markevitch, M., & Vikhlinin, A. 2002, ApJ, 565, 867

Sunyaev, R. A. & Zeldovich, Y. B. 1970, Comments on Astrophysics and Space Physics, 2, 66

Tawa, N., Hayashida, K., Nagai, M., et al. 2008, PASJ, 60, 11

Taylor, G. B., Carilli, C. L., & Perley, R. A. 2000, The Observatory, 120, 278

Thierbach, M. 2000, PhD thesis, Argelander Institüt für Astronomie, Universität Bonn

Thierbach, M., Klein, U., & Wielebinski, R. 2003, A&A, 397, 53

Thompson, A. R., Moran, J. M., & Swenson, G. W. 2002, The Observatory, 122, 48

Trasatti, M. 2010, Master thesis, University of Bologna, Italy

Tribble, P. C. 1993, MNRAS, 261, 57

Vacca, V., Govoni, F., Murgia, M., et al. 2011, A&A, 535, A82

van Weeren, R. J., Brüggen, M., Röttgering, H. J. A., & Hoeft, M. 2011, MNRAS, 418, 230

van Weeren, R. J., Röttgering, H. J. A., Brüggen, M., & Hoeft, M. 2010, Science, 330, 347

van Weeren, R. J., Röttgering, H. J. A., Intema, H. T., et al. 2012a, A&A, 546, A124

van Weeren, R. J., Röttgering, H. J. A., Rafferty, D. A., et al. 2012b, A&A, 543, A43

Vazza, F., Brüggen, M., Gheller, C., & Brunetti, G. 2012, MNRAS, 421, 3375

Vazza, F., Brunetti, G., & Gheller, C. 2009a, MNRAS, 395, 1333

Vazza, F., Brunetti, G., Kritsuk, A., et al. 2009b, A&A, 504, 33

Venturi, T., Giacintucci, S., Brunetti, G., et al. 2007, A&A, 463, 937

Venturi, T., Giacintucci, S., Dallacasa, D., et al. 2008, A&A, 484, 327

Venturi, T., Giovannini, G., & Feretti, L. 1990, AJ, 99, 1381

Vogelsberger, M., Genel, S., Springel, V., et al. 2014, ArXiv e-prints

Voit, G. M. 2005, Reviews of Modern Physics, 77, 207

Werner, N., Kaastra, J. S., Takei, Y., et al. 2007, A&A, 468, 849

Widrow, L. M. 2002, Reviews of Modern Physics, 74, 775

Wik, D. R., Sarazin, C. L., Finoguenov, A., et al. 2009, ApJ, 696, 1700

Yoshikawa, K. & Sasaki, S. 2006, PASJ, 58, 641

ZuHone, J., Markevitch, M., & Brunetti, G. 2011, Mem. Soc. Astron. Italiana, 82, 632

Zwicky, F. 1937, ApJ, 86, 217

Acknowledgements

Finding the words to thank all the people who helped me during these years is, in this moment, the most difficult part of this thesis!

First of all I would like to thank my supervisor Prof. Uli Klein for giving me this great opportunity and for helping and supporting me with my thesis work. Especially thank you for always demonstrating to have faith in me and in my capabilities, sometimes even more than myself! Thank you for giving me the chance to travel around the world to meet and collaborate with great scientists. Thank you for being understanding in the difficult periods that life unfortunately always reserves. Grazie di tutto!

I would like to thank all the people that helped me with my work during these years: Emiliano Orlandi, Lorenzo Lovisari, Annalisa Bonafede, Franco Vazza, Marcus Brüggen, Daniele Dallacasa, Gianfranco Brunetti, Hiroki Akamatsu, Kaustuv Basu, Jens Erler, Tracy Clarke and all the members of the DFG Research Unit 1254.

I would like to thank the secretaries, Elisabeth and Christina, for always being there to help with bureaucratic stuff.

Living these last years in Bonn has been a great experience! I met so many nice people that now I'm afraid I would forget someone...I'll come back to you guys!